Investigations on Environmental Carbons

vorgelegt von
Diplom–Physiker
Jens–Oliver Müller
Berlin

Fakultät II – Mathematik und Naturwissenschaften
der Technischen Universität Berlin
zur Erlangung des akademischen Grades
Doktor der Naturwissenschaften
Dr. rer. nat.

genehmigte Dissertation

Promotionsausschuss:

Vorsitzender:	Prof. Dr. A. Knorr
Berichter:	Prof. Dr. R. Schlögl
Berichter:	Prof. Dr. M. Dähne

Tag der wissenschaftlichen Aussprache: 12. September 2005

Berlin 2005

D 83

Kurzzusammenfassung

Dieselruße, wie andere Feinpartikel, sind gesundheitsschädliche Stoffe, die, wenn sie in das Lungensystem gelangen, zu einer Irritation des Lungengewebes führen können. Dabei ist anzunehmen, daß die Partikel, umso tiefer in die Lunge eindringen können, je kleiner sie sind. Ferner ist nicht auszuschließen, dass Staubpartikel einen nicht unerheblichen Anteil am Treibhauseffekt haben.

Rußpartikel, die bekanntlich aus Kohlenstoff, Sauerstoff und Wasserstoff bestehen, zeigen in der Reaktivität eine deutliche Abhängigkeit von ihrer Mikrostruktur. Dies ist in folgendem Kontext von Vorteil. Sollte in Dieselmotoren eine Abgasreinigung vorgenommen werden, ist es wünschenswert, daß die Rußpartikel schnell zu Kohlenstoffdioxid umgewandelt werden, damit sie nicht in die Atmosphäre gelangen können.

In der vorliegenden Arbeit wurden die Morphologie und die Mikrostruktur von Dieselrußpartikeln mittels Transmissionselektronenmikroskopie untersucht. Zusätzlich dazu konnten unter Verwendung der Elektronenenergieverlustspektroskopie Informationen zur vorherrschenden Bindung der Kohlenstoffatome gewonnen werden. Die Oberfläche, die die Schnittstelle zur Umwelt darstellt, ist mittels Photoelektronenspektroskopie und Infrarotspektroskopie untersucht worden. Diese Messungen stellen den ersten Schritt zu einer Struktur–Reaktivitäts–Korrelation dar. Ergebnisse zur Reaktivität der Dieselrußpartikel konnten mittels Thermogravimetrie gewonnen werden.

Um eine Struktur–Reaktivitäts–Korrelation herzustellen, sind verschiedene Typen von Kohlenstoffverbindungen untersucht worden. Hauptaugenmerk wurde auf den Dieselruß gelegt. Die folgenden Materialien wurden als Strukturmodelle untersucht: Durch Funkenentladungen von Graphitelektroden hergestellter Ruß als Modell für feine atmosphärische Partikel, Industrieruß und große polyaromatische Kohlenwasserstoffe. Die grundlegenden Ergebnisse sind folgende: 1. Die Mikrostruktur der untersuchten Substanzen ist dominiert von Defekten und von der Abweichung von der idealen Struktur des Graphits. 2. Die Eigenschaften der Oberflächen sind dominiert von den Defekten und können mit der Mikrostruktur korreliert werden. 3. Die Reaktivität spiegelt die vorher genannten Ergebnisse wieder. Kleine Rußpartikel, mit sehr defektreicher Mikrostruktur, oxidieren bei niedriger Temperatur. Auch bei unterschiedlichen Abbrandbedingungen bleiben die Ergebnisse aus den vorherigen Untersuchungen bestehen, jedoch zeigt sich, daß NO_2 den Rußabbrand bei kleinen Temperaturen beschleunigt.

Diese Arbeit zeigt, dass moderne Dieselmotoren zwar feineren und reaktiveren Ruß generieren, dieser jedoch durch geeignete Maßnahmen relativ einfach gefiltert und zu CO_2 umgewandelt werden kann. Dies ist der technische Hintergrund dieser Arbeit. Es werden Grundlagen geschaffen, die es ermöglichen sollen, bei Nutzfahrzeugen ein sich ständig selbst regenerierendes Filtersystem zu schaffen.

Abstract

Diesel engine soot, as well as other fine dust particles are harmful compounds which, if they penetrate into the respiratory system, may lead to irritations of the lung tissues. It is very probable that the smaller the particles are the deeper they may be able to enter into the lungs. Furthermore it cannot be excluded that fine dust particles contribute significantly to the green house effect.

Soot particles, which are known to consist mainly of carbon, oxygen and hydrogen, show a clear dependency in their reactivity from their microstructure. This is an advantage if one considers the following context. If the exhaust from diesel engines has to be cleaned it is an advantage if the diesel engine generates soot particles with an increased reactivity which therefore may be easier converted to carbondioxide. In this way, their escape to the atmosphere may be subdued.

In the present work the morphology and microstructure of diesel engine soot particles is investigated. This is done by using transmission electron microscopy. Additional information on predominant bonding, using electron energy loss spectroscopy, of the carbon could be gained. The surface of the soot particles being the interface to the environment, is investigated with X–ray photoelectron spectroscopy as well as infrared spectroscopy. These experiments serve as the first steps to understand the basic structure reactivity correlations. The reactivity of the diesel engine soot particles is accessed with thermogravimetry.

To correlate the structure of the carbons with the reactivity, several types of carbons are investigated. The main emphasis is put on Diesel Engine soot. The following carbonaceous materials served as models for this sort of carbon, soot, generated by spark discharge of graphite electrodes as a model for fine atmospheric particles, carbon black and giant polyaromatic hydrocarbons. The main results of this work are the following: 1. The microstructure is dominated by defects and the deviation from a perfect graphitic structure. 2. The surface functionalization with heteroatoms is dominated by the defects and can be correlated with the microstructural investigations. 3. The reactivity of the carbons reflect the previous investigations. Small particles with their highly defective basic structural units show an onset of oxidation at lower temperatures, than well graphitized carbons. However the influence of the microstructure still holds when using different oxidizing atmospheres. NO_2 accelerates the oxidation of the particles at lower temperatures. Models from solid state kinetics are used to predict the oxidation behaviour under exhaust gas relevant conditions at different temperatures.

The present work shows that modern diesel engines generate finer and more reactive soot, this soot however may relatively easy be filtered and converted. This is the technical background of the present work. A general knowledge is created in order to build a self regenerating particulate trap for heavy duty diesel engines.

List of Figures

List of Tables

Contents

Chapter 1

Introduction

1.1 Motivation

The global emissions of black carbon from combustion of fossil fuels and burning of biomass are increasing. These particles, non-uniformly, but widely distributed throughout the troposphere and even the stratosphere, have a high impact on the atmosphere of the earth due to their reactivity with various gaseous species as NO_X, SO_X and O_3. The physical and structural properties of environmental relevant carbons have recently been investigated with increasing interest. The reactivity and adsorption properties of different substances toward carbon particles, in order to monitor their behavior in the atmosphere, are important [1–3]. Studies to resolve the relative role of soot and dust particles in the climate changes are also undertaken [4]. The impact on the bio–organism or even human health [5–7] is acessed by investigation of carcinogenicity.

The background of this work is the need for improvement of heavy duty diesel engines to fulfill the Euro IV norm introduced in the second half of the year 2005. The aim of this study is to screen the mircomorphology and electronic structure to surface functionalization and reactivity.

The majority of soot and carbon black studies do not attempt a detailed investigation of the microstructure or general morphology. Many studies have ignored the fact that several types of carbon have been used in oxidation, reactivity or atmospheric studies including flame soot, carbon black, and amorphous carbon, reflecting the common opinion (or assumption) that the structure of the soot particles differs little from various sources or synthesis conditions. Most of the studies assume the soot density to be that of graphite. It is consistent with this supposition that studies to date have not performed high resolution transmission electron microscopy in combination with electron energy loss spectroscopy and the surface

sensitive methods X–ray photoelectron spectroscopy and infrared spectroscopy in order to investigate initial soot structure and surface chemistry. If the nanostructure of soot and carbon black depends on the origin, the question has to be risen how the physical and chemical properties are affected. Reviews of literature of reactivity studies point out the fact that the origin of investigated samples indeed influence the results [8–11].

Here, the micromorphology, electronic structure and functionalisation of disordered sp^2 carbon materials is studied. Two soot types from heavy duty diesel engines, a model aerosol soot and two common carbon blacks are investigated. These materials are chosen in order to demonstrate the variety of these carbons. Moreover the investigation of bulk and surface properties are important factors that play a key role in the understanding of the overall behavior of environmentally relevant carbons. The microstructure investigations are carried out by means of high resolution transmission electron microscopy, electronic structure measurements are undertaken with electron energy loss spectrometry. To analyse for carbon–oxygen functionalisation X–ray photoelectron spectroscopy is used. The reactivity toward O_2 and NO_2 using is accessed with thermogravimetric measurements.

Chapter 1 will give a short introduction to the motivation of this work. The politics and legislation behind the diesel engine emissions are introduced.

Chapter 2 describes the technical background of this thesis. A short introduction on history and technology of the Diesel engine will be given here.

Chapter 3 introduces the used bulk (HRTEM and EELS) and surface (XPS and DRIFTS) investigation methods applied in this work.

Chapter 4 gives an insight into the investigations on microstructure (with HRTEM) and electronic structure (with EELS) of the carbon materials.

Chapter 5 draws an image of the investigations (XPS and DRIFTS) that leads to an understanding of the oxygen functional groups present in the materials.

Chapter 6 is the link to chemical reactivity. The combustion behavior of the carbons is described, in order to deduce the structure reactivity correlations. Additionally, the oxidation of Diesel engine soot under real exhaust treatment conditions is examined.

Chapter 7 summarizes the work and gives an outlook on a bright future with a (hopefully) clean environment.

1.2 Rudolf Diesel

Rudolf Diesel (March 18, 1858 – September 30, 1913) is the inventor of the Diesel engine. He was born in Paris and died on the English Channel.

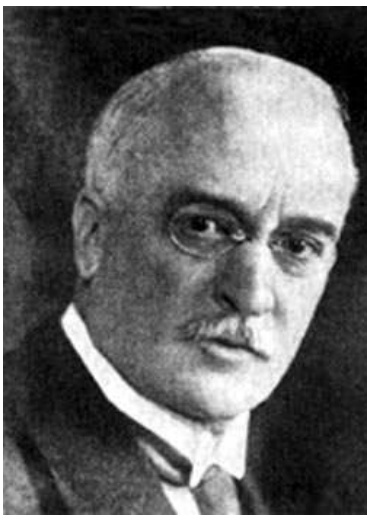

Fig. 1.1: Rudolf Diesel;
Mar. 18, 1858 – Sept. 29, 1913.

Rudolf Diesel developed the idea of the compression ignition engine during the last decade of the 19th century, receiving a patent for the device on Feb. 23, 1893 and building a functional prototype in early 1897 while working at the MAN plant in Augsburg. This "Diesel engine" was named after him. Originally it was known as the "oil engine".

In 1892 Rudolf Diesel was issued a patent for a proposed engine that compresses air so much that the resulting temperature would far exceed the ignition temperature of the fuel. Baron von Krupp and Maschinenfabrik Augsburg Nürnberg in Germany backed Rudolf Diesel financially as well as providing engineers to work with him on the development of an engine that would burn coal dust, because there were mountains of useless coal dust piled up in the Ruhr valley. The first experimental engine was built in 1893 and used high pressure air to blast the coal dust into the combustion chamber. This engine exploded and further developments of using coal dust as a fuel failed, however a compression ignition engine that used oil as fuel was successful and a number of manufacturers were licensed to build similar engines.

The original oil burning engines used very crude mechanical injection equipment so Rudolf Diesel again began using air blast to provide atomization of the fuel as well as turbulence of the mixture. This was very successful and utilized in Rudolf Diesel's third engine built in 1895. This engine was very similar to engines being used today. It was a four–stroke cycle with 450 psi compression. Progress in diesel engine development has since depended on improvements in fuel injection technology.

Between 1911 and 1912 Rudolf Diesel stated "The diesel engine can be fed with vegetable oils and would help considerably in the development of agriculture of the countries which use it" and predicted that "The use of vegetable oils for engine fuels may seem insignificant today. But such oils may become in course of time as

important as petroleum and the coal tar products of the present time".

In Augsburg, on Aug. 10, 1893, Rudolf Diesel's prime model, a single 10–foot iron cylinder with a flywheel at its base, ran on its own power for the first time. Rudolf Diesel spent two more years making improvements and in 1896 demonstrated another model with the theoretical efficiency of 75 percent, in contrast to the ten percent efficiency of the steam engine. By 1898, Rudolf Diesel was a millionaire. His engines were used to power pipelines, electric and water plants, automobiles and trucks, and marine craft, and soon after were used in mines, oil fields, factories, and transoceanic shipping.

Diesel died in mysterious circumstances: He disappeared on a cross–channel ferry. On Sept. 29, 1913 he shipped on the "SS Dresden" for a short trip to the Rover factories in England.

1.3 Emission Standards

The European regulations for new heavy–duty diesel engines are commonly referred to as Euro I – V. The Euro I standards for medium and heavy–duty engines were introduced in 1992. The Euro II regulations came to power in 1996. These standards applied to both heavy–duty highway diesel engines and urban buses. The urban bus standards, however were voluntary.

In 1999, the European Parliament and the Council of Environment Ministers adopted the Euro III standard and also adopted Euro IV and V standards for the years 2005/2008. The standards also set specific, stricter values for extra low emission vehicles (also known as "enhanced environmentally friendly vehicles" or EEVs) in view of their contribution to reducing atmospheric pollution in cities.

The emission limit values set for 2005 and 2008 will require all new diesel–powered heavy duty vehicles to be fitted with exhaust gas after treatment devices, such as particulate traps and DeNO$_x$ catalysts. The 2008 NO$_x$ standard will be reviewed and either confirmed or modified, depending on the available emission control technology.

Table 1.1 contains a summary of the emission standards and their implementation dates. Changes in the engine test cycles have been introduced in the Euro III standard (year 2000). The old steady–state engine test cycle ECE R–49 is replaced by two cycles: a stationary cycle ESC (European Stationary Cycle) and a transient cycle ETC (European Transient Cycle). Smoke opacity is measured on the ELR (European Load Response) test.

For the type approval of new vehicles with diesel engines according to the Euro III

Table 1.1: EU emission standards (european stationary cycle, ESC) for HD diesel engines, g/kWh (smoke in m^{-1}).

Tier	Date & Category	Test Cycle	CO	HC	NOx	PM	Smoke
Euro I	1992, $<$ 85 kW	ECE R-49	4.5	1.1	8.0	0.612	
	1992, $>$ 85 kW		4.5	1.1	8.0	0.36	
Euro II	1996.10		4.0	1.1	7.0	0.25	
	1998.10		4.0	1.1	7.0	0.15	
Euro III	1999.10, EEVs only	ESC & ELR	1.5	0.25	2.0	0.02	0.15
	2000.10	ESC & ELR	2.1	0.66	5.0	0.10	0.8
Euro IV	2005.10		1.5	0.46	3.5	0.02	0.5
Euro V	2008.10		1.5	0.46	2.0	0.02	0.5

standard (year 2000), manufacturers have the choice between either of these tests. For type approval according to the Euro IV (year 2005) limit values and for EEVs, the emissions have to be determined on both the ETC and the ESC/ELR tests.

Emission standards for diesel engines that are tested on the ETC test cycle, as well as for heavy–duty gas engines, are summarized in Table 1.2.

Table 1.2: EU emission standards for diesel and gas engines, european transient cycle (ETC) test, g/kWh.

Tier	Date & Category	Test Cycle	CO	NMHC	CH4	NOx	PM
Euro III	1999.10, EEVs only	ETC	3.0	0.40	0.65	2.0	0.02
	2000.10	ETC	5.45	0.78	1.6	5.0	0.16
							0.21
Euro IV	2005.10		4.0	0.55	1.1	3.5	0.03
Euro V	2008.10		4.0	0.55	1.1	2.0	0.03

1.3.1 ESC Test Cycle

The ESC test cycle has been introduced, together with the ETC and the ELR tests, for emission certification of heavy–duty diesel engines in Europe starting in the year 2000. The ESC is a 13-mode, steady–state procedure. The engine is tested on an engine dynamometer over a sequence of steady–state modes (Figure 1.2). The engine must be operated for the prescribed time in each mode, completing engine speed and load changes in the first 20 seconds. The specified speed shall be held to within $\pm$50 rpm and the specified torque shall be held to within $\pm$ 2% of the maximum torque at the test speed. Emissions are measured during each mode and averaged over the cycle using a set of weighing factors. Particulate matter emissions are sampled on one filter over the 13 modes. The final emission results are expressed in g/kWh.

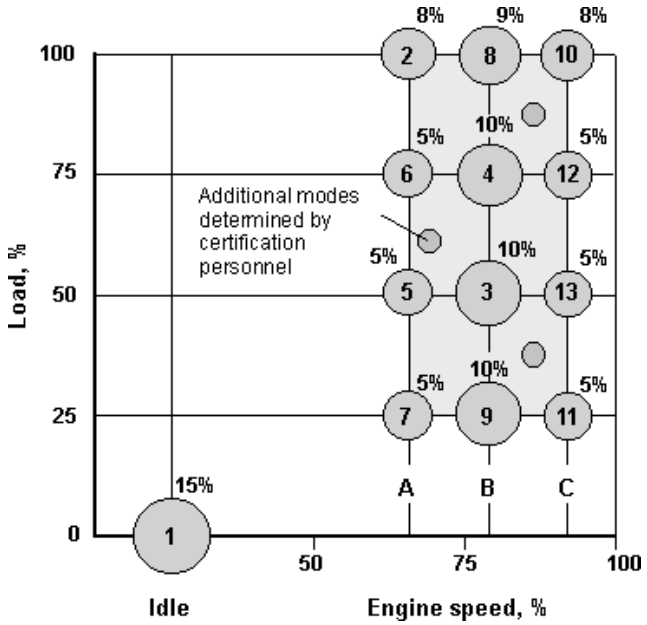

Fig. 1.2: Scheme for the European Stationary Cycle. The 13 test modes are indicated, additional tests may be chosen from operator.

During emission certification testing, the certification personnel may request additional random testing modes within the cycle control area (Figure 1.2). Maximum emission at these extra modes are determined by interpolation between results from the neighboring regular test modes. Point 1 is held for 4 minutes, the remnant points are then held for 2 minutes respectively.

The engine speeds are defined as follows: The high speed n_{hi} is determined by calculating 70% of the declared maximum net power. The highest engine speed where this power value occurs (i.e. above the rated speed) on the power curve is defined as n_{hi}. The low speed n_{lo} is determined by calculating 50% of the declared maximum net power. The lowest engine speed where this power value occurs (i.e. below the rated speed) on the power curve is defined as n_{lo}. The engine speeds A, B, and C to be used during the test are then calculated from the following formulas:

$$A = n_{lo} + 0.25\,(n_{hi} - n_{lo}) \tag{1.1}$$

$$B = n_{lo} + 0.5\,(n_{hi} - n_{lo}) \tag{1.2}$$

$$C = n_{lo} + 0.75\,(n_{hi} - n_{lo}) \tag{1.3}$$

The ESC test is characterized by high average load factors and very high exhaust gas temperatures.

1.3.2 ETC Test Cycle

The ETC test cycle was also introduced, together with the ESC, for emission certification of heavy–duty diesel engines in Europe starting in the year 2000. The ETC cycle has been developed by the FIGE Institute, Aachen, Germany, based on

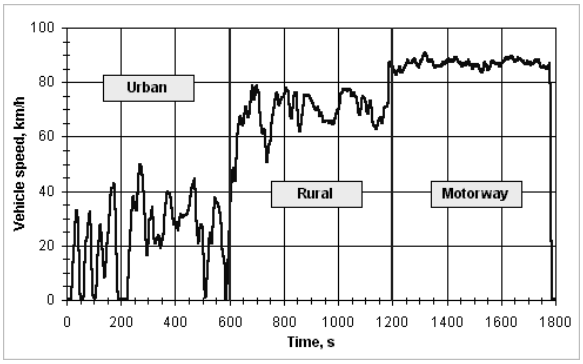

Fig. 1.3: ETC transient cycle – vehicle speed. The vehicle speed is simulated for different situations as urban, rural and motorway traffic.

real road cycle measurements of heavy duty vehicles. Different driving conditions are represented by three parts of the ETC cycle, including urban, rural and motorway driving. The duration of the entire cycle is 1800 s. The duration of each part is 600 s. Part one represents city driving with a maximum speed of 50 km/h, frequent starts, stops, and idling. Part two is rural driving starting with a steep acceleration segment. The average speed is about 72 km/h. Part three is motorway driving with average speed of about 88 km/h. Vehicle speed vs. time over the duration of the cycle is shown in Fig. 1.3. For the purpose of engine certification, the ETC cycle is performed on an engine dynamometer. This allows to measure the pertinent engine speed and torque curves.

1.4 Advantages and Disadvantages vs. Spark–Ignition Engines

Diesel engines are more massive than gasoline/petrol engines of the same power because of the heavier construction required to withstand the higher combustion pressures needed for ignition. Yet it is this same build quality that has allowed to acquire significant power increases with turbocharged engines through fairly simple modifications. A gasoline engine of similar size cannot put out a comparable power increase without extensive alterations because the stock components would not be able to withstand the higher stresses placed upon them. Since a diesel engine is already built to withstand higher levels of stress, it makes an ideal candidate for

performance tuning at little expense.

The addition of a turbocharger or supercharger to the engine greatly assists in increasing fuel economy and power output. The higher compression ratio allows a diesel engine to be more efficient than a comparable spark ignition engine, although the calorific value of the fuel is slightly lower at 45.3 megajoules/kilogram to gasoline at 45.8 megajoules/kilogram.

The increased fuel economy of the diesel over the petrol engine means that mile–for–mile the diesel produces less carbon dioxide (CO_2). The recent development of biofuel alternatives to fossil fuels has unleashed the ability to produce a net–sum of zero emissions of CO_2, as it is re-absorbed into plants and then comes full circle, being used to produce the fuel.

Diesel engines produce black soot from their exhaust. This consists of unburnt carbon compounds. Other problems associated with the exhaust gases (high particulates, nitrogen oxide, sulfurous fumes) can be mitigated with further investment and equipment. This issue is the basis of motivation of this work.

1.5 Carbon

The chemistry of the element carbon is complex with a wide form of micro– and nanostructured varieties that exceed the well known crystal structures of graphite and diamond [12]. In its elemental forms carbon occurs in sp^2 or in sp^3 atomic hybridization.

The sp^3 bonding configuration leads the stable structure of diamond (m3m) [13]. The diamond lattice consists of two interpenetrating face–centered cubic Bravais lattices, displaced along the body diagonal of the cubic cell by one quarter of the length of the diagonal. The coordination number is four. Its surface is terminated usually by hydrogen atoms. This surface is chemically very inert and requires strong chemical reagents to change the terminating heteroatom. Over-oxidation and local thermal effects might lead to an interconversion of the surface of diamond into graphite on which oxygen functional groups, characteristic of bulk graphite can all exist.

The sp^2 type of bonding results in the structure of Graphite (6/mmm) [13]. It has a simple hexagonal Bravais lattice with four carbon atoms per primitive cell. The lattice planes perpendicular to the c–axis have a honeycomb arrangement, building a layered structure with strong in–plane bonds and weak out of plane bonding of the van der Waals type. The separation between lattice planes along the c–axis is almost 2.4 times the nearest–neighbour distance within the planes. Graphite is

the thermodynamically stable bulk phase of carbon up to very high temperatures under normal ranges of pressure (diamond is only kinetically stable). This is not the case with finite numbers of carbon atoms. In the nanosize range, the size of the graphenes leads to a high density of dangling bonds. In this case, the structure does gain energy by closing onto itself and removing all the dangling bonds, leading then to fullerenes or carbon nanotubes.

Nanostructured carbon is also known in the form of Fullerenes [14], carbon nanotubes [15], –fibers and –whiskers. These forms of carbons are the "third" form of carbon being neither graphite nor diamond. The bonding properties of these carbons are a hybrid of sp^2 and sp^3. The strongly bent sp^2 carbon fullerene C_{60} exhibits the electronic structure of a polyolefinic molecule with well resolved molecular resonances for the anti–bonding π^* states. Graphite as planar sp^2 carbon exhibits at similar energies than fullerene its metallic π^* conduction band. The skeletal σ^* bonds of the sp^2 hybridization are well separated from the π^* states.

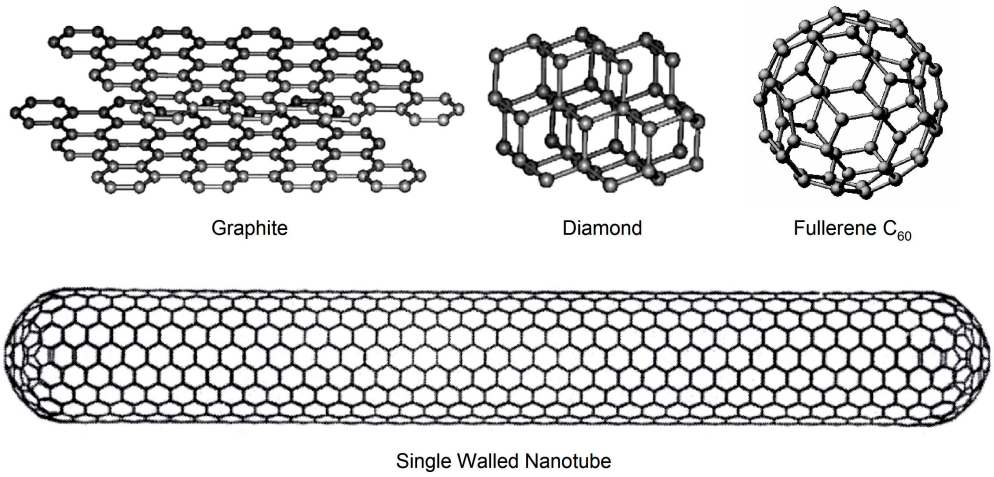

Fig. 1.4: The modifications of carbon: Graphite, Diamond, Buckminster Fullerene and Carbon Nanotube.

The fullerenes are closed shell all carbon molecules with an even number of atoms (starting at C_{28}) and nominal sp^2 bonding between adjacent atoms. To form curved structures (such as the fullerenes) from a planar fragment of hexagonal graphite lattice, certain topological defects have to be included in the structure. This is done by creating pentagons. A carbon nanotube consists of a long cylinder made of the hexagonal honeycomb lattice of carbon, bound by two pieces of fullerenes at the ends. The diameter of the tube will depend on the size of the semi–fullerene that the end is made of [16].

The surface chemistry is strongly correlated to the chemical bonding within the bulk of carbon. The sp^2 configuration of carbon atoms leads to planar graphene

layers if only the most stable geometric arrangement of six–membered rings are formed as primary structural motif. The result is a family of well–ordered or turbostratically (randomly around the surface normal rotated graphene layers) disordered stacks of planar layers (graphenes) with lateral dimensions ranging from a few nm to several ten micrometers. Graphitic and carbon black materials result from this arrangement. The strain (deviation form planarity) increases significantly the reactivity and forces the ideally delocalized π electrons from the sp^2 bonds into localized states ending in fullerenes in a polyolefinic rather than in an aromatic electronic structure. Structural deviations from planar geometries will result in a vast variation in carbon functional groups. For bent sp^2 carbons all atoms at the surface are potential binding sites for heteroatoms. For planar sp^2 carbons (Fig. 1.5) only two types of anchoring points exist with the well known zig–zag and arm–chair configurations.

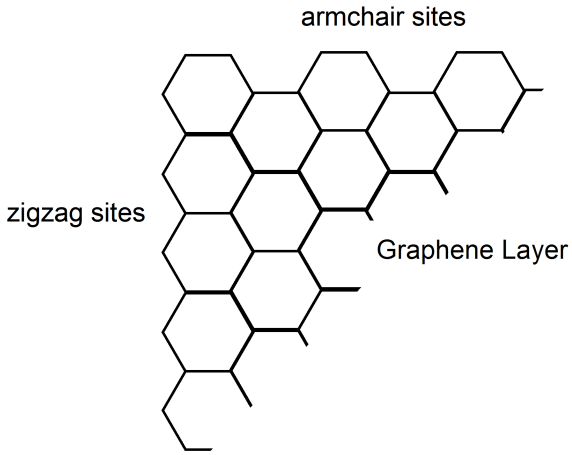

Fig. 1.5: Graphene sheet exhibiting the two types of termination as ″armchair″ and ″zig–zag″. At graphene edges a mixture of both topologies occur.

For non–hydrogen heteroatoms the topology thus has significant implications on the resonance stabilisation of carbon heterobonds with the ″aromatic″ π – electronic system. The most important point in the surface chemistry of carbon is the fact that due to the semimetallic or ″aromatic″ chemical bonding of the sp^2 configuration no functional chemistry can occur on the vastly dominating basal planes at the surface of the graphitic materials. All these sites are coordinatively saturated and can only act as nucleophiles or metals towards weakly adsorbing species. The surface chemistry of sp^2 carbon involving covalent bond formation is thus completely dominated by defect sites and the prismatic face boundaries of the graphene layers.

Chapter 2

Technical Background

In this chapter the general features of the diesel engine are described (section 2.1). In section 2.2 the problems of exhaust and exhaust treatment for diesel engines are stressed. At the end of the chapter in section 2.3 the device for collecting soot particles is described.

2.1 Diesel Engine Concept and Engine-Internal Features

In this section the overall principles of modern diesel engines are briefly described [17–19]. The experiments are carried out using a modified MAN D0836 LF-4V six-cylinder engine (6.6 l displacement, 228 kW) with two-stage controlled turbocharging, an external, controlled cooled EGR and a CR injection system (Fig. 2.1). The engines injection, turbocharging and EGR systems are set for a NO_x emission of less than 3.5 g/kWh and a PM emission of 0.03/0.06 g/kWh (ESC/ETC). The maximum exhaust gas volume flow at the nominal engine speed and full load was 1200 Nm^3/h.

2.1.1 Injection System

To achieve the Euro IV standards places great demands on engine components and the internal combustion. Large EGR rates (15–20 %, depending on engine speed and the load conditions) are necessary to meet the Euro IV standard for NO_x while maintaining an acceptable level of fuel consumption. A high-performance and flexible injection system must be used so that particle emissions remain within the permissible range. Preinjection is used to avoid the large cylinder pressure gradient otherwise caused by the necessarily large injection pressures (maximum 1600 bar), so that combustion noise levels comply with current requirements.

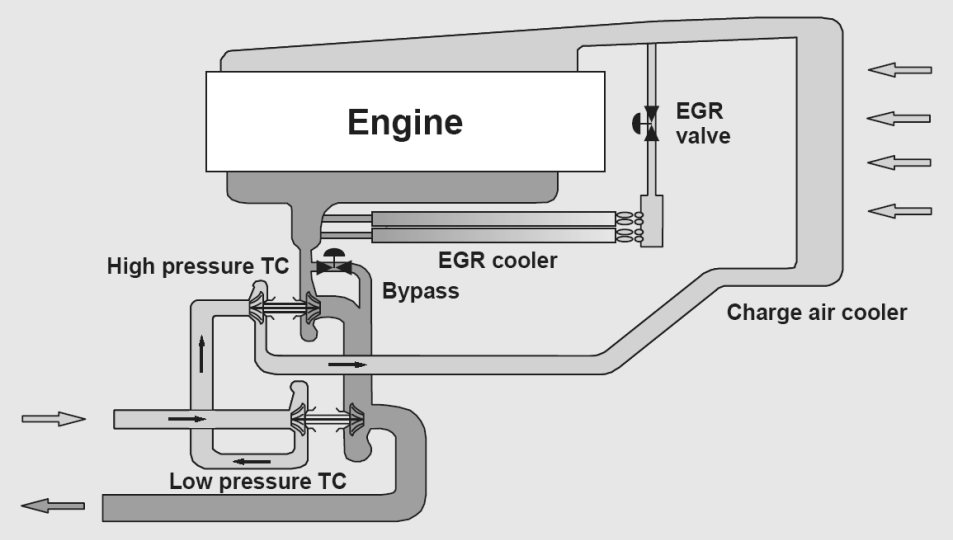

Fig. 2.1: Schematic drawing of the diesel engine described in this section. The sketch includes the charge air cooling section, the turbocharger group (low pressure and high pressure TC) and the recirculation of cooled exhaust gas (EGR).

2.1.2 Turbocharger System

A sufficiently low particle level cannot be achieved with high injection pressures alone due to the mutually interdependent parameters of soot emission, NO_x emission and EGR rate. Any further increase in injection pressures would require further increases in the EGR rate due to the corresponding increases in NO_x emissions. Due to the decreasing level of excess air and the associated increase in soot emissions, this would then again require higher injection pressures. Thus a vicious circle develops, which can be halted by maintaining a sufficient level of excess air. This together with today's standard demands for a higher level of performance and superior driving dynamics make two–stage turbocharging necessary. The slight reduction in soot levels is a result of the higher air supply in the combustion chamber (Fig. 2.1). In dynamic operation the advantages of two–stage turbocharging are clearly evident. A better reaction behavior is obtained. This means that during acceleration the high–pressure compressor is better able to supply the required air demand quickly. The losses in efficiency – caused by blow back in the high–pressure turbine for higher mass flows and by the phase–by–phase unequal distribution of compression work during acceleration – are accepted because of the positive effect on particle emission.

2.1.3 EGR System

Exhaust gas recirculation systems are introduced to reduce the exhaust emission of oxides of nitrogen. They are formed when temperatures in the combustion chamber get too hot. At temperatures higher than 1400 °C the nitrogen and oxygen in the combustion chamber can chemically combine to form nitrous oxides (NO_x). The EGR system recirculates exhaust into the intake stream. Exhaust gases have already combusted, so they do not burn again when they are recirculated. These gases displace some of the normal intake charge. This slows and cools the combustion process by several hundred degrees and thus reduces the formation of NO_x. A EGR system may actually increase engine performance and economy. As the combustion chamber temperature is reduced, the engine detonation potential is also reduced. This factor makes it possible to enhance the spark timing program, increasing power, performance and economy. In order to guarantee as spontaneous a reaction as possible in the turbocharger group during acceleration phases in transient operation, the EGR is switched off during these periods. In this way the entire exhaust gas mass flow is available to the turbocharger group during acceleration. At the same time extreme EGR peaks in the charge air pipe are avoided. However, excessively long and excessively frequent closed phases in transient operation (ETC test) are not possible due to the low NO_x target level.

2.2 Exhaust & Exhaust Treatment

In order to introduce exhaust treatment systems it is necessary to give an overview of exhaust composition. A graphical presentation is given in Fig. 2.2.

Harmful components are included in the exhaust gas to an amout of 0.22 vol%. The particulate matter (soot, ash, oil and fuel) contributes to the exhaust with an amount of 20–200 mg m^{-3}. This is 50 times as much as in the case of the Otto four stroke engine (1–10 mg m^{-3}).

Any particulates that are generated in the diesel engine have to be removed from the exhaust. Several different attempts are made to reach the soot particle free diesel engine [20]. Efficient soot oxidation by O_2 can be supported by the addition of catalytically active metal oxide nanoparticles [21–25] to the fuel. However, this approach involves the danger of even more potentially hazardous emissions.

Another possibility is the oxidation of the diesel soot in filters with the aid of NO_2

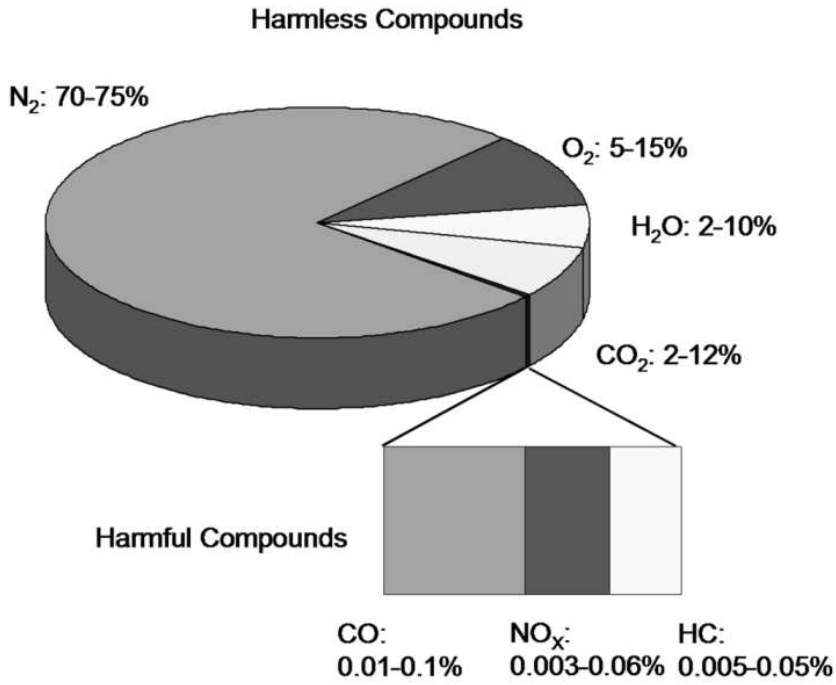

Fig. 2.2: Composition of HD diesel engine exhaust. The graph shows the amount of basically harmless and harmful compounds in the exhaust gas of a diesel engine.

with the following possible reactions:

$$\mathrm{C}(s) + \mathrm{NO_2} \longrightarrow \mathrm{CO}(g) + \mathrm{NO}(g) \tag{2.1}$$

$$\mathrm{CO}(g) + \mathrm{NO_2}(g) \longrightarrow \mathrm{CO_2}(g) + \mathrm{NO}(g) \tag{2.2}$$

$$2\mathrm{NO}(g) + \mathrm{O_2} \longrightarrow 2\mathrm{NO_2} \tag{2.3}$$

A wide range of of particle trapping and exhaust treatment have been introduced and are still under development, for example ceramic diesel particulate filters, particle traps and oxidation catalysts with open deposition structures. The aim of this work is to separate particles in a structure that in principle remains open, and thus do not need to be exchanged. However care must be taken to ensure that the de-

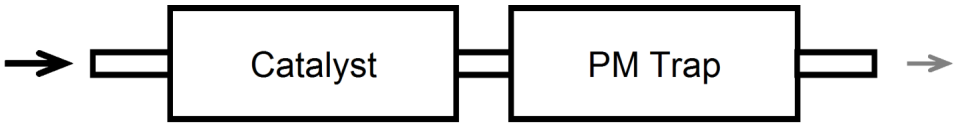

Fig. 2.3: Catalyst–filter–combination used for exhaust treatment. The aim is to oxidize NO_x to NO_2 and to regenerate with this oxidant the soot trapped in the filter device.

posited particles cannot shear off as a result of the aerodynamic forces associated with sudden surges in the mass flow. This system is required to be capable of splitting the exhaust gas stream. The particulate matter is now deposited in this open

structure by aerodynamical forces. The structure is filled with particles, so that ultimately a point is reached at which the flow of exhaust gas has to overcome an increasing resistance. In order for further particles to be trapped, the particles that have been deposited must be decomposed again. This is done for instance by oxidizing the carbon using NO_2. To achieve this, an oxidation catalyst, in which NO_2 is formed, is placed before the filter (Fig. 2.3). At temperatures exceeding 200 °C the NO_2 should react continuously with the deposited particles.

2.3 Collection of Soot Particles

To collect the Euro IV HD diesel engine soot particles for TEM investigations a special particle collector (Fig. 2.4) is designed and built. The center of this collector is a vacuum T-piece. The typical copper grids (3 mm diameter, 400 mesh) coated with holey carbon film [26] used for TEM investigations are fixed in an exchangeable holder. Two valves control the inlet and the outlet of the piece. through the third

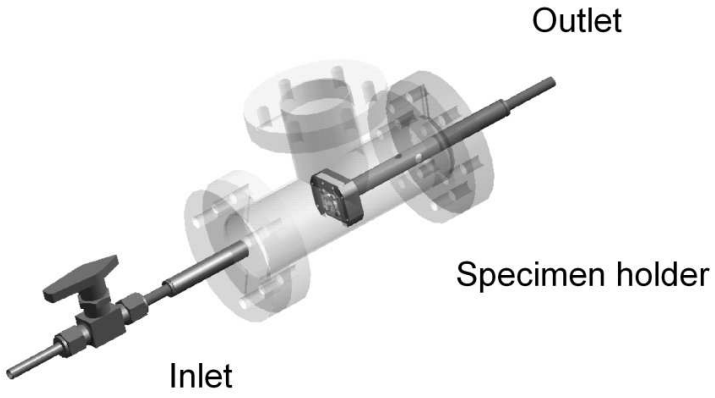

Fig. 2.4: Schematical drawing of the particle collector designed for loading soot on TEM copper grids. The exhaust gases are led through the device. The grid–holder is exchanged through the ”short” part of the device.

part of the ”T” the holder can be removed and changed. The collector is attached to the exhaust pipe of the engine, as seen in the photograph Fig. 2.5. A fraction of the exhaust gases of the engine are led directly through the collector and through the copper grids. In this way the soot agglomerates attach to the hole borders. Thus they are large enough that investigations without underlying carbon film are possible. To avoid condensation of water from the exhaust gases, the gas inlet and the whole collection chamber are heated. The collector ensures reproducible sampling conditions without problems of water condensation. A good reproducibility of sampling conditions is achieved. Constant gas throughput volumes are achieved with a pump which is adjusted to a constant flow of 5 l/min.

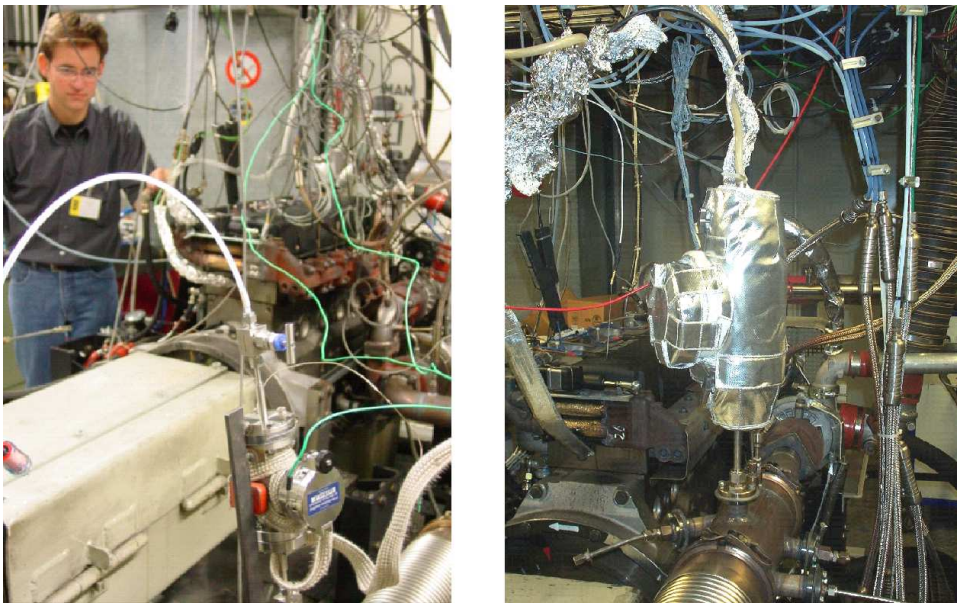

Fig. 2.5: Particle collector for TEM grids attached to the exhaust pipe of the diesel engine, image taken during a campaign at the MAN test bench in Nürnberg. The left hand side shows the diesel engine (with operator), the right side the mounted particle collector with heating facility.

Chapter 3

Characterization

In this chapter the characterization methods are described. The first section 3.1 gives a short overview over transmission electron microscopy (TEM), the second section 3.2 deals with electron energy loss spectroscopy (EELS). In section 3.3 and 3.4 the investigation methods for surface measurements X–ray photoelectron spectroscopy (XPS) and infrared spectroscopy in diffuse reflection (DRIFTS) are presented. The last section introduces Thermogravimetry (TG).

3.1 Transmission Electron Microscopy

TEM is analogous to optical transmission microscopy, but using an electron beam and magnetic lenses instead of visible light and glass lenses, respectively [27–29]. The transmitted electron beam forms an image, which is a 2–dimensional projection of the 3–dimensional sample in the direction of the beam. The resolution is limited by the wavelength of the probing waves. This is 400–700 nm for visible light. The wavelength of the electrons can be reduced to values suitable for imaging atomic features by accelerating electrons through high voltages (kV). The lenses in a TEM are electromagnetic, which makes it possible to change the strength of the lenses and to adjust the magnification and defocus without physically changing or moving the lenses. However, the lenses are sensitive to instabilities in the lens current which influence the resolution of the microscope.

Fig. 3.1 shows the sketch of a TEM equipped with a field–emission gun which is used to study the morphology and microstructure of the carbonaceous materials. The field–emission gun (FEG) electron source, which is a very fine needle, works as a cathode with respect to two anodes. Electrons are pulled out from the extraordinarily fine needle (tungsten) by an extraction voltage of ≈ 3.8 kV created by the first

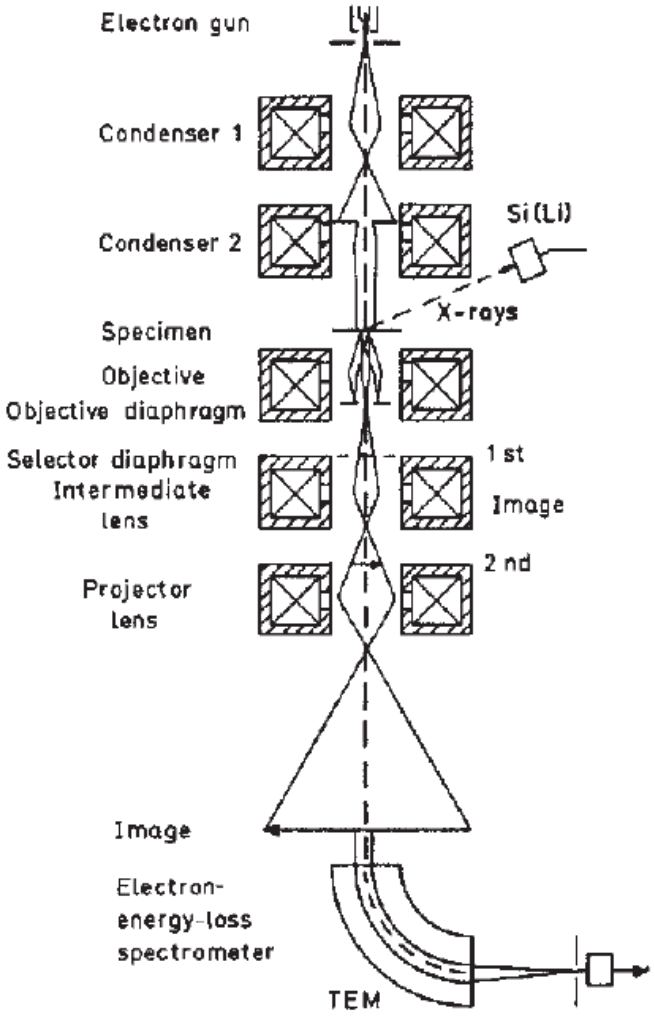

Fig. 3.1: Sketch of a TEM equipped with X–ray detector and imaging filter. The image shows the condensor lens system, the objective lens with aperture as well as the intermediate and projector lenses.

anode. The second anode accelerates the electrons to their final energy (200 keV). The FEG produces a highly coherent beam, which is essential for high resolution TEM. Condenser lenses, which are placed between the FEG unit and the specimen (see Fig. 3.1) forces the electrons into a parallel beam, before they interact with the specimen. The first image is generated by the objective lens. The first intermediate lens of the microscope is responsible for the coupling of the magnifying unit (projector lenses) to the first image generated. The projector lenses are responsible for the image magnification. Different excitations will result in different magnifications (in the case of the used TEM up to 1 000 000 times). Basically, TEM is a diffraction technique.

In Fig. 3.2 the ray–trace of the incident electron beam at the specimen to the final image is shown.

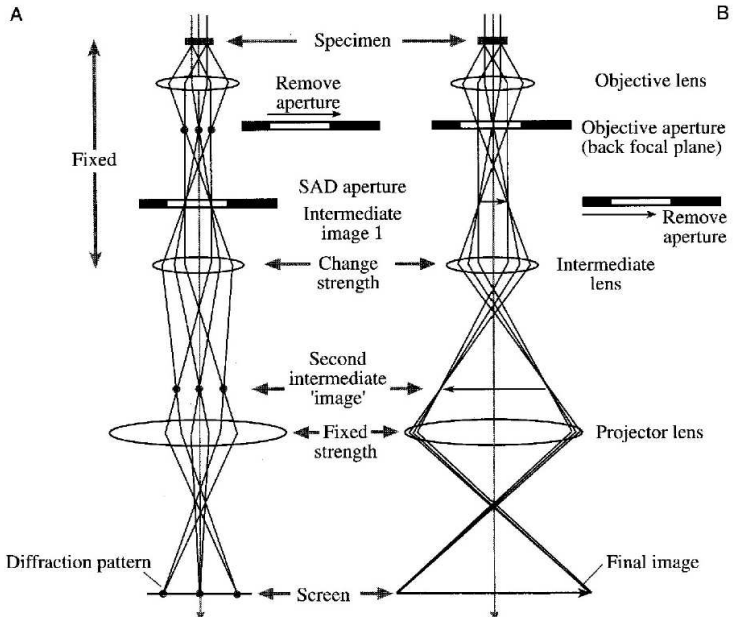

Fig. 3.2: Ray–trace of the electron beam in the column. A shows the ray–trace for electron diffraction, B shows the ray–trace for imaging. Both operation modes are achieved with changing the focus of the intermediate lens.

The microscope is operated in two modes: The diffraction mode, which will produce a diffraction pattern of the probed specimen on the viewing screen, and imaging mode, which results in an image of the specimen. Controlling the strength of the intermediate lenses shifts between these two modes. In the diffraction mode the object of the intermediate lenses is chosen as the back focal plane of the objective lens. In imaging mode the object of the intermediate lens is the image plane of the objective lens. For digital image recording, a CCD camera coupled to the imaging filter (Gatan) is used to depict the intensity variations of the transmitted

electron beam. As electrons interact strongly with matter and the electron beam has to be transmitted through the sample, only very thin samples are suitable for TEM. The maximum thickness suitable depends on the system of interest, but as a rule of thumb the thickness must not exceed 100 nm. The requirement of thin specimens is a major limitation of TEM. In general, two types of contrast are observed in a transmission electron microscope operating in imaging mode. The mass-thickness contrast or diffraction contrast, which is observed in low magnification images, and the phase contrast which accounts for atomic resolution in high magnification images. The mass thickness contrast/diffraction contrast is induced by electrons that are scattered off-axis by elastic scattering as they pass through the specimen with a typical scattering angle of $\gg 10$ mrad. The cross section for elastic Rutherford scattering is proportional to Z^2. As the thickness increases, more electrons are scattered off-axis. Electrons scattered through angles larger than the objective aperture (see Fig. 3.2) are intercepted resulting in high mass-thickness areas to appear darker than low mass-thickness areas. This type of contrast can be enhanced by decreasing the size of the objective aperture, although the total image intensity decreases. The phase contrast is produced by interference between the scattered wave and the incident wave at the image point. This contrast gives detailed structural information of the specimen at an atomic level.

3.2 Electron Energy Loss Spectroscopy

Electron Energy Loss Spectroscopy (EELS) is an established technique to investigate the composition of and the electronic structure in solids [30–32]. The basic principle is as follows: The energy distribution of initially monoenergetic electrons is analyzed after they have interacted inelastically with a specimen. These inelastic collisions reveal information about the electronic structure of the specimen atoms and hence, details of the nature of these atoms, their bonding and nearest–neighbour distributions, and their dielectric response. Transmission EELS is usually carried out in a TEM, which allows high spatial resolution and also offers imaging and diffraction capabilities that can be used to identify the structure of the analyzed material.

3.2.1 Electron Energy Loss Spectrum

The beam of electrons that have transmitted the sample is directed into a high-resolution electron spectrometer which separates the electrons according to their kinetic energy and produces an electron energy loss spectrum showing the scat-

tered intensity (electron counts) as a function of the decrease in kinetic energy of the incident fast electron. The first zero–loss or "elastic" peak in Fig. 3.3 represents

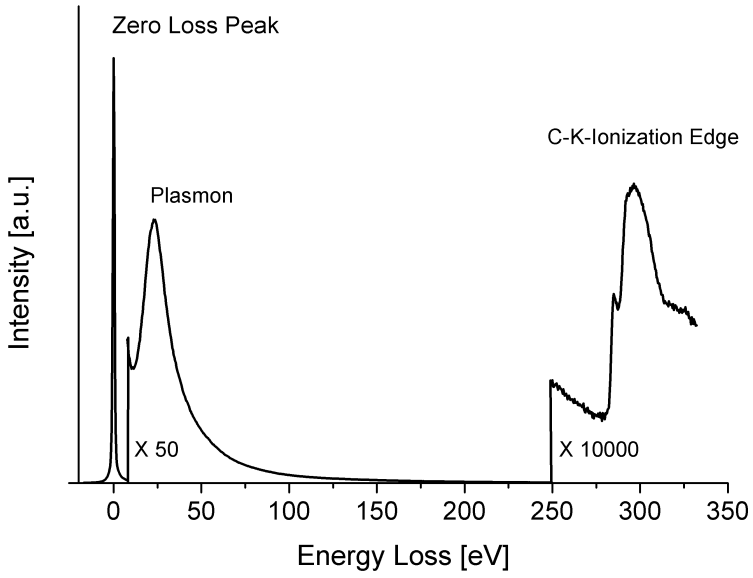

Fig. 3.3: Example of an EELS–spectrum. Included are the zero–loss peak, the intensity of plasmon oszillations and the carbon–K ionization edge.

electrons which are transmitted without suffering any measurable energy loss, including those which are scattered elastically in the forward direction and those which have excited phonon modes, for which the energy loss is less than the experimental energy resolution. The low–loss region up to an energy loss of about 50 eV contains electrons which have interacted with the weakly bound outer-shell electrons of the atoms in the specimen, i.e. electrons that have set up plasmon oscillations or have generated inter– or intra–band transitions. Plasmons are longitudinal wave–like oscillations of weakly bound electrons. The plasmon peak is the second most dominant feature of the energy–loss spectrum after the zero–loss peak. Electrons in the high–loss region have interacted with the more tightly bound inner–shell or "core" electrons to move it outside the attractive field of the nucleus, resulting in an ionization process. The ionization losses are characteristic of the atom involved and so the signal is a direct source of elemental information, just like the characteristic X–rays (feature at 285 eV in Fig. 3.3). When viewed in greater detail, both the valence–electron (low–loss) peaks and the ionization edges possess a fine structure which reflects the crystallographic or energy–band structure of the specimen. Therefore, an element or compound that is present in different forms (like in the defect rich carbons) shows quite distinct fine structures as will be shown later.

3.2.2 Instrumentation

EEL spectra are recorded with the Gatan Imaging Filter GIF 100. The energy resolution is 1 eV (FWHM of the zero loss). A schematic drawing is given in Fig. 3.4

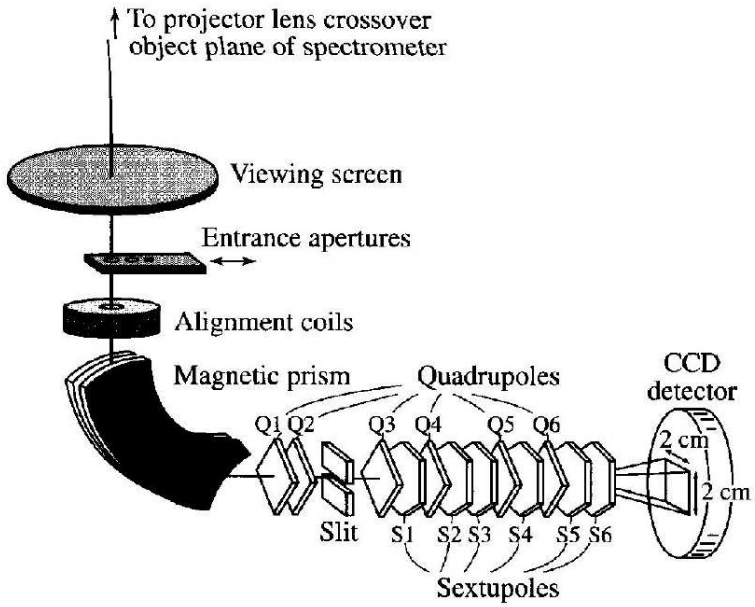

Fig. 3.4: The Gatan Imaging Filter. The filter is attached to the bottom of the column of the electron microscope. The electrons are led through a magnetic prism. Energy filtered imaging as well as electron energy loss spectroscopy is possible through adjusting the quadrupole and hexapole lenses of the filter.

The Gatan Imaging Filter (GIF) is mounted on the bottom of the camera chamber of the TEM. It allows images and diffraction patterns produced by the TEM to be transformed into energy–filtered (energy–selected) images and diffraction patterns. It can also form energy loss spectra with a range of energy dispersions. After passing the entrance aperture the electrons travel down a "drift tube" through the spectrometer and are deflected through $\geq 90^\circ$ on the basis of the velocity–dependent Lorentzforce.

Electrons with greater energy loss are deflected further than those suffering zero loss. A spectrum is thus formed in the dispersion plane which consists of a distribution of electron counts versus energy loss. Besides bending the electron beam and creating energy dispersion, the magnetic prism also has a focusing action and creates an energy dispersed, focused image of the TEM's projector lens crossover. This is the energy–loss spectrum. A quadrupole–sextupole assembly is mounted at the end of the prism. It can be operated in two modes: In image mode, it takes

the electrons which are selected by an energy–selecting slit located in the plane of the focused energy–loss spectrum and projects an energy–selected version of the TEM image onto the cameras. In spectroscopy mode, the quadrupole–sextupole assembly projects the focused energy loss spectrum onto the cameras.

3.2.3 Theoretical Background

Excitations from inner shells of atoms give rise to absorption edges in Energy Loss Spectroscopy similar to the well–known X–ray absorption edges (Fig. 3.5). In general these edges occur at energies E $\geq$ 50 eV for most elements, which is far beyond the interaction energy of valence electrons in the solid state. This allows to treat the target electrons as bound to single nuclei, not interacting with other atoms. On the other hand, valence or conduction electrons interact strongly with one another and influence the low loss region E $\leq$ 20 eV. In the following, the probability for inelastic scattering of electrons on atoms is calculated as a function of energy and momentum transfer.

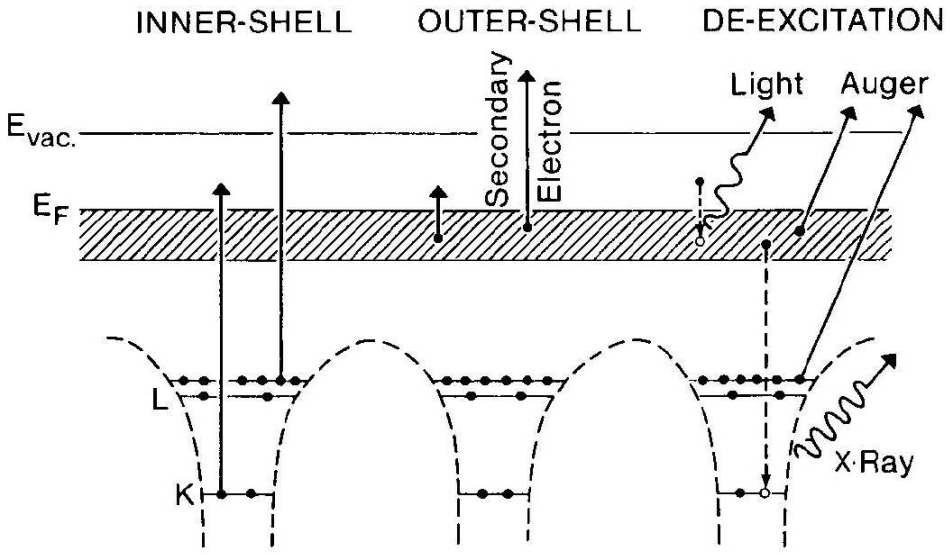

Fig. 3.5: Energy–level diagram of a solid , including K– and L– shell core levels and the valence band (shaded); E_F is the Fermi level and E_{vac} the vacuum level. The primary processes of inner– and outer–shell excitation are shown on the left, secondary processes as photon and electron emission on the right (adapted from [30]).

The scattering probability is the differential cross section which is measurable directly in energy loss experiments.

According to Fermi's golden rule, the transition probability of a system going from an initial state $|i\rangle$ to a final state $|f\rangle$ by the influence of a perturbance given by the operator V is proportional to the square of the transition matrix element. the rule

is derived in time dependent perturbation theory and gives the transition rate W (transitions per time):

$$\mathrm{d}W_{fi} = \frac{2\pi}{\hbar} \left|\langle f|V|i\rangle\right|^2 \mathrm{d}v_f \cdot \delta\left(E_i - E_f\right) \tag{3.1}$$

$\mathrm{d}W_{fi}$ is the number of transitions from unperturbed state $|i\rangle$ to state $|f\rangle$ within the differential phase space element $\mathrm{d}v_f$ around $|f\rangle$ per unit time (transition rate). The differential particle current of free electrons scattered into $(\mathrm{d}\Omega, \mathrm{d}E)$ can be calculated by summing 3.1 over all possible final states $|f\rangle$. This gives the double differential cross section:

$$\frac{\partial^2\sigma}{\partial E \partial\Omega} = \frac{2\pi}{\hbar}^4 \sum_f \frac{k_f}{k_i} \left|\langle f|V|i\rangle\right|^2 \delta\left(E_i - E_f\right) \tag{3.2}$$

In elastic scattering, both, initial and final state are considered free states, and V is a static potential.

Inelastic scattering can be treated similarly when V represents the interaction potential between the probe and the target charges. Then $|i\rangle$ and $|f\rangle$ in 3.1 resemble many particle state vectors, including the target atoms.

3.2.4 The Dynamic Form Factor

The approximation that leads to the transition rate W_{fi} (Eq. 3.1) is only valid if the perturbation V is small compared to the energy of the scattered electrons, as for fast collisions. The unperturbed state vectors can be approximately factorized, since exchange effects are negligible:

$$|i\rangle = |k_i\rangle \otimes |\varphi_i\rangle\,, \qquad |f\rangle = |k_f\rangle \otimes |\varphi_f\rangle\,, \tag{3.3}$$

k_i, k_f are free states, φ_i and φ_f are the eigenfunctions of the electrons bound to the target nucleus before and after the collision.

The interacting potential representing the electrostatic forces between an incident electron and an atom can be written as

$$V = \frac{-Ne^2}{r} + \sum_{i=1}^{N} \frac{e^2}{|\mathbf{r} - \mathbf{r}_i|} \tag{3.4}$$

where the first term represents Coulomb attraction by the nucleus and the second term is a sum of the repulsive effects of each atomic electron at coordinate r_i.

This leads to the double differential cross section within the first Born approximation:

$$\frac{\partial^2\sigma}{\partial E\partial\Omega} = \left(\frac{2me^2}{\hbar^2Q^2}\right)\frac{k_f}{k_i}\sum_{i,f}\left|\langle\varphi_f|\exp\left(i\mathbf{QR}\right)|\varphi_i\rangle\right|^2\delta^2\left(E+E_{\varphi_i}-E_{\varphi_f}\right) \tag{3.5}$$

$E = E_{k_i} - E_{k_f}$ in 3.5 is the energy loss, $\mathbf{Q} = \mathbf{k}_i - \mathbf{k}_f$ is the wave vector transferred during the interaction.

3.2.5 Orientation sensitive EELS

The operator which connects initial and final state can be expanded as

$$\exp\left(i\mathbf{QR}\right) = 1 + i\mathbf{QR} - \left(\mathbf{QR}\right)^2 + \text{plus higher order terms} \tag{3.6}$$

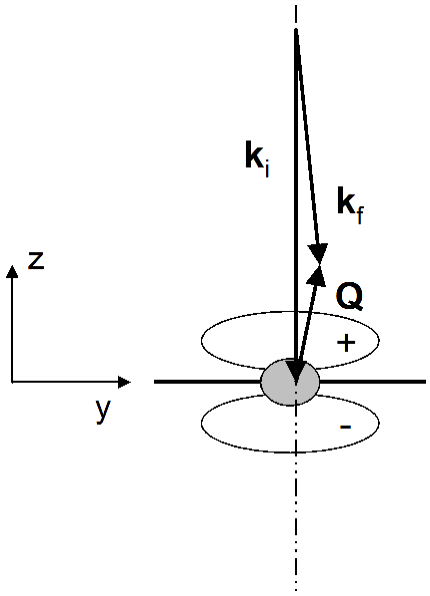

Fig. 3.6: Principle of an excitation from an initial $|s\rangle$ to a final $|p\rangle$ state.

which allows 3.5 to be split into terms of different order in $\mathbf{QR}$. If $\mathbf{QR} \ll 1$ then the higher order terms in 3.5 can be neglected and the matrix element reduces the dipole form:

$$\langle\varphi_f\left|\mathbf{QR}\right|\varphi_i\rangle \tag{3.7}$$

In this form the matrix element is similar to the dipole matrix element for the absorption of polarized electromagnetic radiation. The condition for the dipole ap-

proximation is fulfilled in the case of small scattering angles. This implies that $\mathbf{Q} \ll r_C^{-1}$, where r_C is the radius of the core state defining the spatial region in which most of the transitions occur. The dipole form of the matrix element requires that selection rules apply and hence, the relation between angular momentum in the initial state ℓ and final state ℓ' is $\ell' = |\ell \pm 1|$.

In case of an initial s symmetry the final state must therefore be of p symmetry:

$$\langle \varphi_f \, |\mathbf{QR}| \, s \rangle = Q \, \langle \varphi_f \, |z| \, s \rangle = Q \, \langle p_z | p_z \rangle \, , \qquad \text{if} \quad \mathbf{Q} = \mathbf{z}Q \tag{3.8}$$

3.2.6 The Beam Collection and Convergence Angle

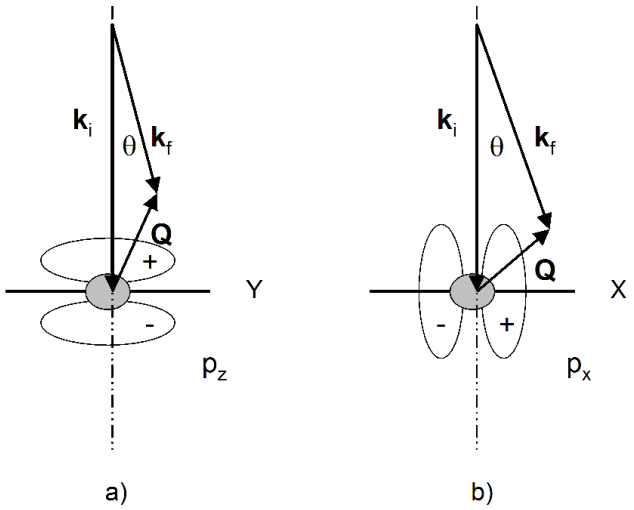

Fig. 3.7: Dependence of the final state upon the direction of the transferred momentum Q: a) case of a small scattering angle b) case of a large scattering angle.

Detailed intensity variations in the spectrum depend on the range of electron scattering angles which are gathered by the spectrometer. In order to investigate anisotropy in the local final DOS with EELS, the spectrometer collection angle is an important variable: In case of a small collection angle (Fig. 3.7a), EELS probes states which are polarized parallel to the incident beam. In case of a larger collection angle (Fig. 3.7b), additional excitations into orbitals perpendicular to the incident beam contribute to the spectrum. In order to give a reasonable interpretation of the fine structure in EELS measurements, the dipole approximation must be fulfilled and, additionally, the spectrometer collection angle must be known. The angular dependence of the spectra allows qualitative determination of the orientation of orbitals to which spectral features correspond.

The convergence angle, also termed illumination angle, can be obtained directly in the diffraction pattern of a sample: $\alpha \approx \frac{r}{L}$, where L is the camera length and r is the

radius of the diffraction spots. The size of the spectrometer entrance aperture and the setting of the camera length L determine the collection semiangle $\beta = \frac{s}{L'}$, where s is the radius of the projected spectrometer entrance aperture and L' is the effective camera length: from projector lens crossover to spectrometer entrance aperture.

Determination of the Characteristic Scattering Angle

The momentum transferred from an incident electron to an atomic electron within the sample is related to the scattering angle ϑ through conservation of energy and momentum.

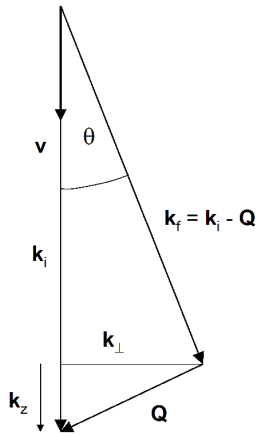

Fig. 3.8: Momentum triangle of inelastic scattering.

The momentum transfer **Q** can be split into a component parallel and a component perpendicular to the incident beam direction:

$$\mathbf{Q} = \mathbf{k}_z + \mathbf{k}_\perp \tag{3.9}$$

For small scattering angles follows:

$$|\mathbf{k}_\perp| = \vartheta \, |\mathbf{k}_i| \tag{3.10}$$

It follows that $Q^2 = k_i^2 \left(\vartheta^2 + \vartheta_E^2\right)$. Where $\vartheta_E = E/2E_0$ ($\vartheta_E = E/2\gamma T$ in the relativistic case) is the characteristic angle of inelastic scattering and depends only on the energy loss E. In the case of small **Q** follows from 3.5:

$$\frac{\partial^2 \sigma}{\partial E \partial \Omega} \propto \frac{1}{Q^2} \tag{3.11}$$

Therefore, the angular distribution of ionization–loss electrons varies as $\left(\vartheta^2 + \vartheta_E^2\right)^{-1}$

and will be a maximum for $\vartheta = 0$ in the forward-scattered direction. The distribution decreases to the FWHM at the characteristic scattering angle ϑ_E. At an incident energy of 200 keV, the characterisic scattering angle for the carbon–K–ionization edge (at about 285 eV) is:

$$\vartheta_E = \frac{E}{2\gamma T} = \frac{285 \text{ eV}}{343.8 \text{ keV}} = 0.83 \text{ mrad} \tag{3.12}$$

3.2.7 Determination of the sp^2/sp^3 Hybridisation Ratio with EELS

In this case we require the EEL spectra to be orientation independent even for anisotropic materials. Such a situation arises in determining the average bonding nature of carbon materials. A method for evaluating this property, developed by Berger et al. [33], is to measure the relative intensity of the 1s to π^* peak in the carbon K ionization edge. One of the problems inherent in the use of this technique is the fact that the 1s to π^* transition intensity is determined by the experimental conditions. As a consequence, for high collection angles, the spectrum does not mirror the electronic structure of the selected anisotropy axis. In graphite with the c–axis oriented parallel to the beam this would mean, that instead of the π^* peak, the σ^* becomes more dominant as observed in Fig 3.9.

The approach is to eliminate the orientation dependence completely through a judicious choice of convergence and collection condition. This is called the "Magic–Angle–condition". If this is applied to both the unknown carbon material and that of standards for sp^2 materials, the relative intensity of the 1s–to–2p π^* transition can be directly related to the bonding nature of the materials alone [34].

The double differential cross section for inelastic electron scattering is given in the equation 3.5 already. For scattering geometry for graphite it is convenient to express $\mathbf{Q}_0$ in cylindrical coordinates which relate to the azimuth φ and the scattering angle ϑ as:

$$\mathbf{Q} = \begin{pmatrix} k_0 \sin\vartheta \sin\varphi \\ k_0 \sin\vartheta \cos\varphi \\ k_0 \vartheta_E \end{pmatrix} \tag{3.13}$$

The incident electron's trajectory is parallel to the cylinder axis. For small scattering angles we can replace $\sin\vartheta$ by ϑ. The classical characteristic scattering angle is then $\vartheta_E = E/2E_0$. Q can be interpreted as the kinetic energy of an electron with momentum $\hbar$q; i.e. the energy of a free photoelectron at rest before the scattering. The kinematically corrected expression yields the characteristic scattering angle as al-

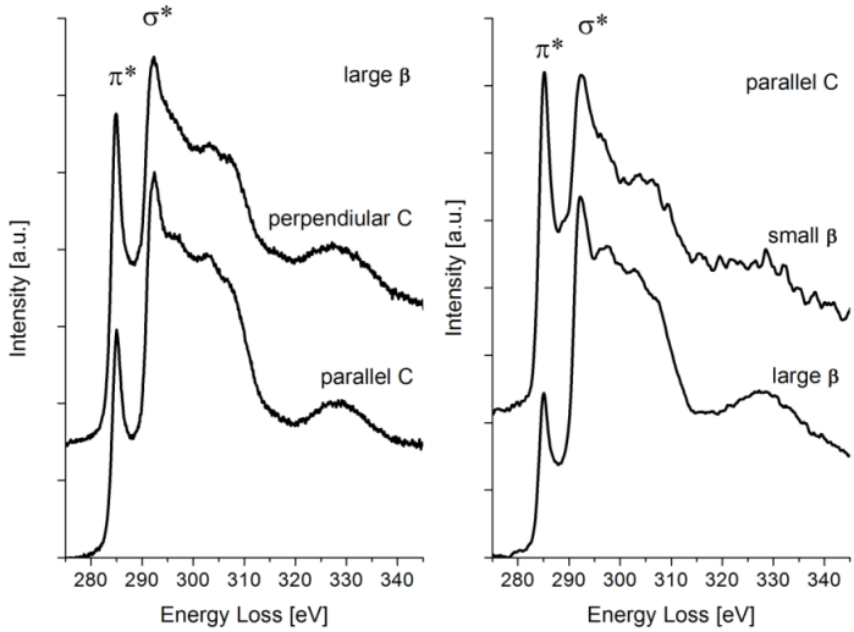

a) b)

Fig. 3.9: EELS spectra for a) HOPG in different orientations b) HOPG oriented with the c–axis parallel to the electron beam, changing the collection angle β. Note in both cases the change in intensity ratio between the π^* and the first σ^* peak.

ready described. The magic angle is found to be at 3.97 ϑ_E. Experiments have used a magic angle of 2 ϑ_E. The apparent difference was lately solved in using a relativistic correction. This replaces the z–component in equation 3.13 with $k_0\vartheta_E(1-\beta^2)$. This correction then is closer to the experimentally estimated magic angle combination (also used in this work), i.e. 1.46 ϑ_E at 200 keV. Apart from experimental uncertainties, several effects can explain the remaining disagreement between experiment and theory. First, coupling to diffuse quasi-elastic and to Bragg scattering can change the apparent fine structure, and consequently change the measured magic angle. Errors in the calibration of the camera length may contribute with $\pm 3\%$: Finally, channeling effects in a zone axis orientation and non-dipole transitions may play a minor role. However the correct settings of incident and collection angle are measured in Section 4.2.2 (Chapter 4).

3.3 X–Ray Photoelectron Spectroscopy

X–ray photoelectron spectroscopy (XPS), also known as Electron Spectroscopy for Chemical Analysis (ESCA), is a widely used technique for obtaining chemical information of material surfaces. Core–level electrons are emitted from a surface after it

has been irradiated with soft X–ray. The low kinetic energy (0 – 1500 eV) of emitted photoelectrons limits the depth from which it can emerge so that the sample depth is in the range of few nanometers (in carbon $\approx$ 5 nm). Photoelectrons are collected and analyzed by the instrument to produce a spectrum of emission intensity versus electron binding energy. In general, the binding energies of the photoelectrons are characteristic of the element from which they are emanated so that the spectra can be used for surface elemental analysis. Small shifts in the elemental binding energies provide information about the chemical state of the elements on the surface. Therefore, the high resolution XPS studies can provide the chemical state information of the surface.

Traditionally, when the technique has been used for surface studies it has been subdivided according to the source of exciting radiation into X-ray Photoelectron Spectroscopy (XPS) – using soft X–ray (200 – 2000 eV) radiation to examine core-levels. Ultraviolet Photoelectron Spectroscopy (UPS) – using vacuum UV (10 – 45 eV) radiation to examine valence levels.

The kinetic energy distribution of the emitted photoelectrons (i.e. the number of emitted photoelectrons as a function of their kinetic energy) can be measured using any appropriate electron energy analyzer and a photoelectron spectrum can thus be recorded.

The process of photoionization can be considered as follows:

$$A + h\nu \rightarrow A^{+} + e^{-} \tag{3.14}$$

Conservation of energy then requires that:

$$E(A) + h\nu = E(A^{+}) + E(e^{-}) \tag{3.15}$$

The final term in brackets, representing the difference in energy between the ionized and neutral atoms, is generally called the binding energy (E_B) of the electron – this then leads to the following commonly quoted equation. The E_B is now taken to be a direct measure of the energy required to just remove the electron concerned from its initial level to the vacuum level and the kinetic energy (E_{kin}) of the photoelectron is again given by:

$$E_{kin} = h\nu - E_B \tag{3.16}$$

The binding energies (E_B) of energy levels in solids are conventionally measured with respect to the Fermi-level of the solid, rather than the vacuum level. This

involves a small correction to the equation given above in order to account for the work function Φ of the solid.

The XPS investigations are carried out in a modified LHS/SPECS EA200 MCD system equipped with facilities for XPS (Mg Kα 1253.6 eV, 168 W power). For the XPS measurements a fixed analyser pass energy of 48 eV is used resulting in a resolution of 0.9 eV FWHM of the Ag $3d_{5/2}$ peak. The binding energy scale is calibrated using Au $4f_{7/2}$ = 84.0 eV and Cu $2p_{3/2}$ = 932.67 eV. The sample was mounted on a stainless steel sample holder without any further preparation step in order to avoid the potential preparation artefacts on the surface. The base pressure of the UHV analysis chamber is $< 1 \cdot 10^{-10}$ mbar.

3.4 Infrared Spectroscopy

Diffuse reflection infrared fourier transform spectroscopy (DRIFTS) is used to acquire additional information on surface functional groups on the carbon materials. When a beam of electromagnetic radiation of intensity I_0 is passed onto a substance, it is either absorbed or reflected, depending upon its frequency and the structure of the molecule it encounters. When a molecule absorbs radiation it gains energy as it undergoes a quantum transition from one energy state ($E_{initial}$) to another (E_{final}). The frequency of the absorbed radiation is related to the energy of the transition by Planck's law:

$$E_{initial} - E_{final} = E = h\nu = hc/\lambda \tag{3.17}$$

If a transition exists which is related to the frequency of the incident radiation by Planck's constant, the radiation can be absorbed. If the frequency does not satisfy the Planck expression, the radiation will be transmitted. A plot of the frequency of the incident radiation vs. the percent radiation absorbed by the sample is the absorption spectrum of the compound.

There are in general several types of motion that a molecule may undergo. The molecule undergoes translational motion (kinetic energy), given by $\frac{mv^2}{2}$ (v = velocity of the center of mass of the molecule). The molecule has three translational degrees of freedom.

Second, the molecule may rotate. Thus, the rotation of the molecule may be resolved into three mutually perpendicular components. Each atom has, therefore, 3 degrees of freedom available to it, for a total of 3N for the molecule.) This leads to the general rule, that the number of vibrational degrees of freedom is given by

3N–6 for a non-linear polyatomic molecule; and by 3N–5 for a linear polyatomic molecule.

Each of the vibrational motions of a molecule occurs with a certain frequency, which is characteristic of the molecule and of the particular vibration. The molecule may be made to go from one energy level to a higher one by absorption of a quantum of electromagnetic radiation. In undergoing such a transition, the molecule gains vibrational energy, and this is manifested in an increase in the amplitude of the vibration.

In order for a particular vibrational mode to directly absorb infrared electromagnetic radiation, the vibrational motion associated with that mode must produce a change in the dipole moment of the molecule. The requirement that a vibration must cause a change in the dipole moment of the molecule in order to absorb radiation can be understood if we realize that exchange of energy between electromagnetic radiation and matter can occur only if the radiation and matter can interact (or couple) in some way.

To analyse for functional groups in the carbonaceous materials IR spectroscopy is applied. The measurements are performed in diffuse reflectance (Graseby-Specac DRIFTS accessory) using a Bruker IFS 66 FTIR–spectrometer.

3.5 Thermogravimetry

In thermogravimetry (TG) changes in the mass of a sample are studied while the sample is subjected to a controlled temperature program. The temperature program is most often a linear increase in temperature, but isothermal studies can also be carried out, when the changes in sample mass with time are followed. (There is also a family of newer control techniques – i.e. controlled rate methods, and Hi-Res TG).

TG is inherently quantitative, and therefore an extremely powerful thermal technique, but gives no direct chemical information. The ability to analyse the volatile products during a weight loss is of great value.

The essential components of the equipment used, called a thermobalance, are a recording balance, furnace, temperature programmer, sample holder, an enclosure for establishing the required atmosphere, and a means of recording and displaying the data.

Balance sensitivity is usually around one microgram, with a total capacity of a few hundred milligrams. A typical operating range for the furnace is ambient to 1000 °C, with heating rates up to 100 °C/min. The quality of the furnace at-

mosphere deserves careful attention, particularly the ability to establish an inert (oxygen–free) atmosphere, and it is useful to be able to quickly change the nature of the atmosphere. Compatibility between the materials of construction and the sample and its decomposition products, and the gaseous atmosphere, must be considered. Sample holder materials commonly available include aluminium, platinum, silica, and alumina.

Many factors influence the form of the TG curve, both sample- and instrument-related, some of which are interactive. The primary factors are heating rate and sample size, an increase in either of which tends to increase the temperature at which sample decomposition occurs, and to decrease the resolution between successive mass losses. The particle size of the sample material, the way in which it is packed, the crucible shape, and the gas flow rate can also affect the progress of the reaction. Careful attention to consistency in experimental details normally results in good repeatability. On the other hand, studying the effect of deliberate alterations in such factors as the heating rate can give valuable insights into the nature of the observed reactions.

TG is applied extensively to studying analytical precipitates for gravimetric analysis. The derivative of the TG curve, or the DTG curve, is often useful in revealing an extra detail. The DTG curve is sometimes used to determine inflection points on the TG curve, to provide reference points for weight change measurements in systems where the weight losses are not completely resolved.

In this work the TG/DSC data is acquired using a Netzsch-STA 449 instrument with Al_2O_3 crucibles. The gas phase products are transferred through a heated quartz capillary to a quadrupol mass spectrometer operated in SIM mode (Thermostar, Balzers). For investigations under more realistic exhaust conditions a Seiko TG/DTA instrument is used.

Chapter 4

Microstructure

In this chapter the first section 4.1 will describe the results of the TEM investigations undertaken on the various soots, carbon blacks and carbon model substances. In the second section 4.2 the results of the EELS measurements are presented including the determination of the sp^2/sp^3 hybridization of the carbons. In the third section 4.3 the results are discussed with the background of soot formation in flames and especially in diesel engines.

4.1 TEM Work

4.1.1 General TEM Investigation of Diesel Engine Soot

In order to understand the morphology of diesel engine soot and to test the reproducibility of the collection technique, different soot samples were collected using different engine setting and engine loads. The particle collector for TEM is tested using different collection times as well. An example of collection of the soot in the holes of the carbon film is given in Fig. 4.1. The charging of the particulates in the holes of the carbon films is clearly observed.

The expected fractal–like agglomerates [35, 36] of the soot are well resolved in the TEM micrograph (Fig. 4.1). The soot agglomerates are suspended over the hole. Chainlike agglomerates with a size up to 2 μm can be seen in the image. These agglomerates seem to consist of spherical like single particles. These particles are often called primary particles. They form long chains interwoven to give the fractal forms as depicted in Fig. 4.1.

A more detailed investigation is needed in order to screen the different morphologies of the soot emitted from different engine settings. These are important pa-

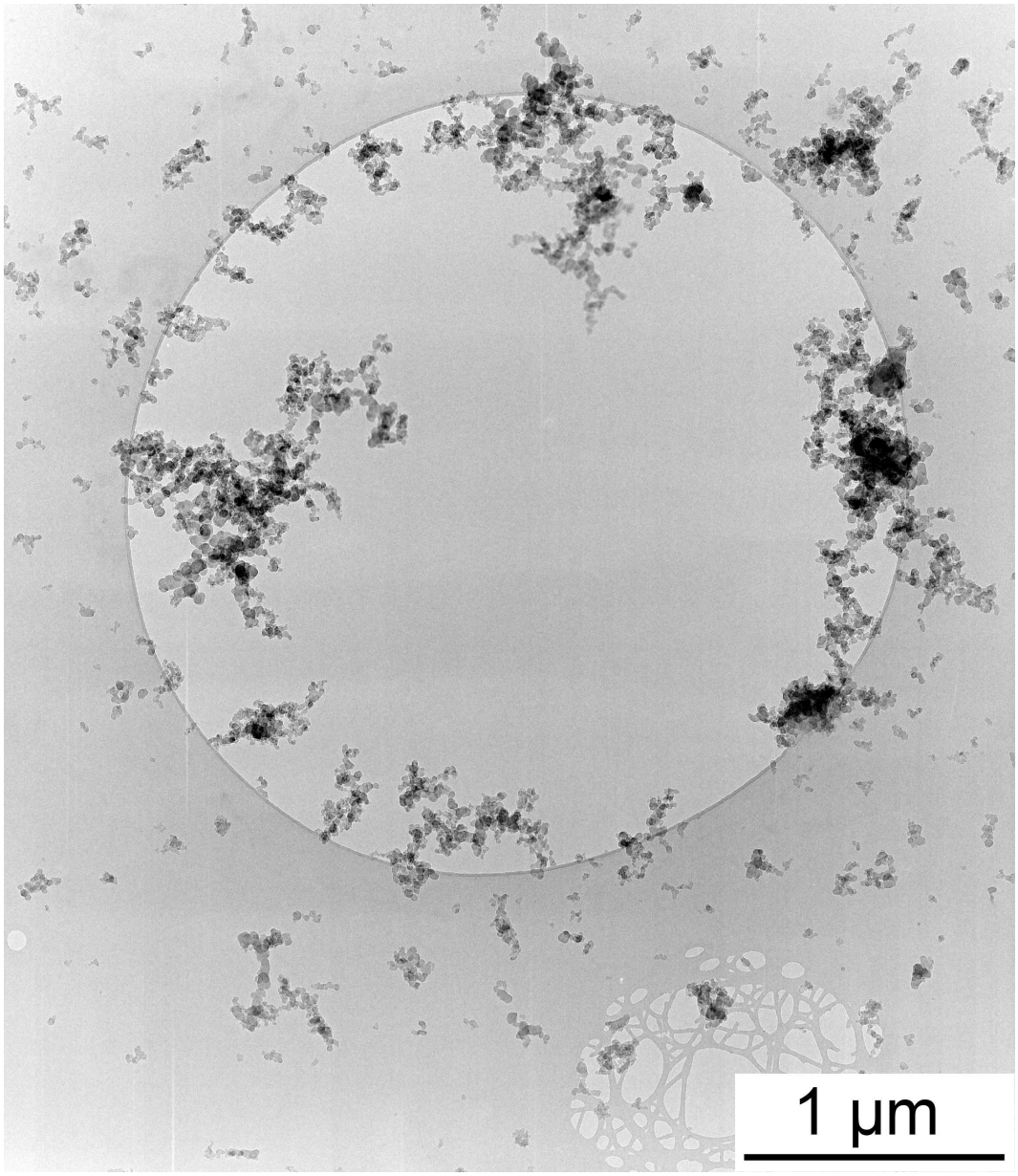

Fig. 4.1: Collection of Euro IV HD diesel engine soot. The soot agglomerates are attached to the border of the hole. Thus it is ensured that TEM and EELS investigations can be done on parts without underlying carbon film.

rameters to understand the reactivity for the exhaust treatment system. To screen the settings properly three different sets of conditions are chosen: 30%, 50%, 75% load respectively. It is observed that the morphology of the soot samples changes slightly (Fig. 4.2).

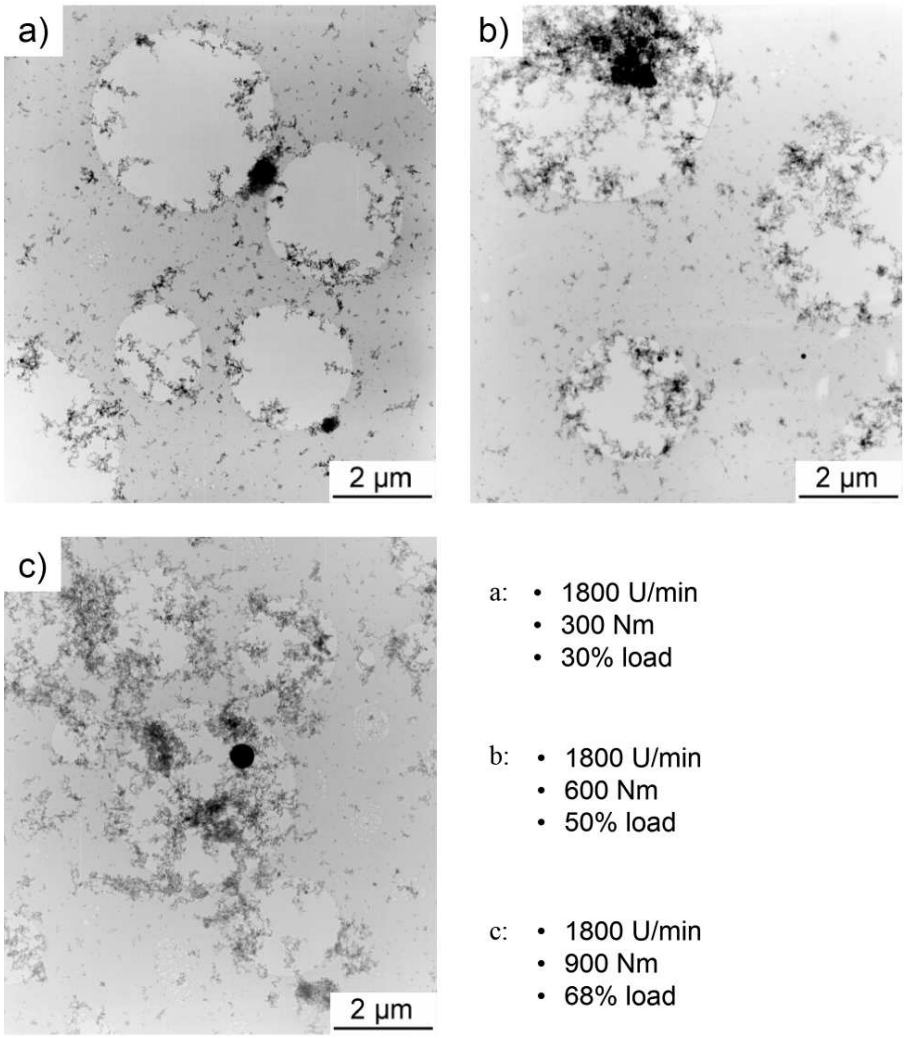

Fig. 4.2: Loading of the holey carbon films as a function of different settings of the diesel engine. a) low load b) middle load c) high load.

In all the three cases displayed in Fig. 4.2a, b, and c the collection time for the soot was the same i.e. 20 minutes. A constant gas volume was led through the grids. This measurement shows that the diesel engine emits different amounts of soot for the different settings. At high load more soot is produced than at low load. This is visualized with the clogging of the holes in the carbon film. The images reveal that oil drops with incorporated ash are also collected with this method. Furthermore this indicates that the the purpose of the particle collector works. Soot particles can be sampled reproducibly, the amount of particulate matter can be controlled.

4.1.2 Investigation of Euro III soot

In order to investigate the change of the soot with respect to the improvement in combustion from diesel engines, soot is sampled from a diesel engine set to fulfill Euro III conditions. The aim is to compare the measurements from this engine to the improved diesel engines. HRTEM images are acquired as well as scattering contrast images. From scattering contrast images a size distribution is evaluated. In order to obtain valuable information the relevant data is obtained from 25 TEM images and thus $\approx$ 200 particles. A representative micrograph of spherical soot particles predominant in the particulate matter is given in Fig. 4.3.

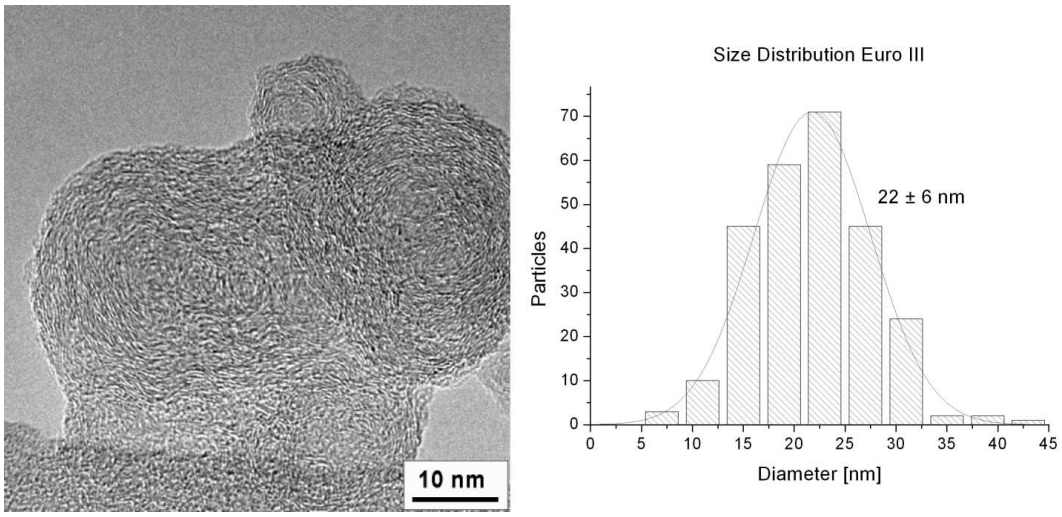

Fig. 4.3: HRTEM micrograph of Euro III HD diesel engine soot. The size distribution reveals a particle size of (22 $\pm$ 6) nm.

The size distribution is depicted as well. The median size of the spherical particles is (22 $\pm$ 6) nm. The Euro III HD diesel engine soot particles exhibit a core shell structure. The spherical–like primary particles are built of a disordered core about 5 nm in diameter. The surrounding shell is 8–10 nm thick. It consists of stacked graphite like subunits referred to as Basic Structural Units (BSU). This term originally used by Oberlin [37] describes small crystals with a size up to 3 nm. The BSU are formed of up to 6 graphene stacks. The term graphene is used in this work for the description of a single graphite layer. The interplanar distance is slightly larger 3.4–3.5 Å) than the typical distance in graphite (3.35 Å). The spheres coagulate to fractal like agglomerates. These agglomerates can attain sizes up to several μm.

4.1.3 Investigation of Euro IV soot

A general morphology of soot from a diesel engine set to fulfill the Euro IV conditions is depicted in Fig. 4.4. The spherical particles with the core shell structure are not predominant. Nevertheless a size distribution of soot spheres could be accomplished. This was equally done in acquiring overviev TEM images and measuring the single spherical particles. The median size is here: (18 $\pm$ 6) nm.

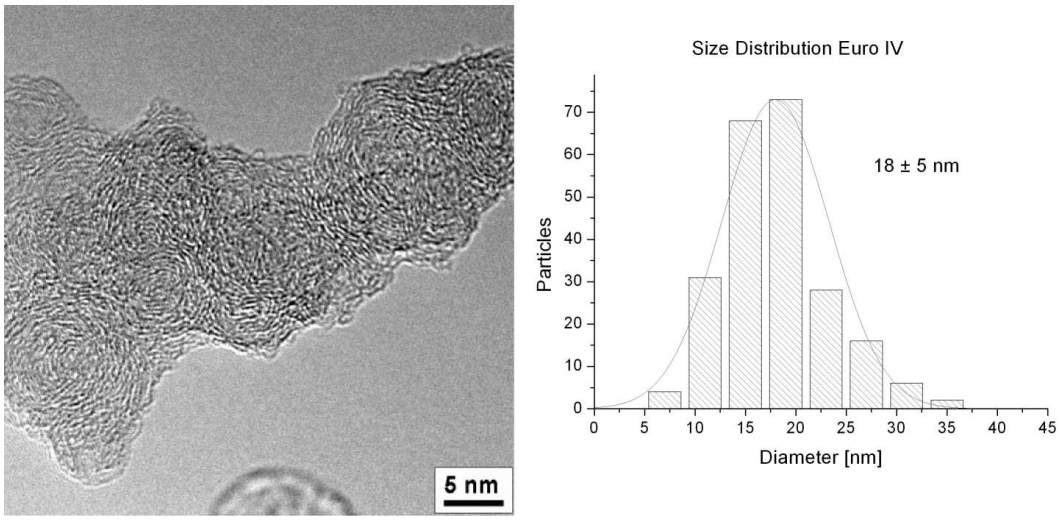

Fig. 4.4: HRTEM micrograph of Euro III HD diesel engine soot. The size distribution reveals a smaller particle size as in the case of the Euro III soot: (18 $\pm$ 5) nm.

The image of Euro IV soot reveals a different microstructure compared to the Euro III HD diesel engine soot. The carbon is made from units of sp^2 carbon that form interlaced bundles of ribbons with eventual large areas of planar interconnection. The primary units are bands of carbon with multiple continuous bending. No specific core of particles as typical of onion-like carbons can be identified. The interlacing can be explained by the frequent apparent intersection of the bands leaving, in 2–dimensional projection, the impression of discontinued contrast.

The secondary structure of the Euro IV soot formed from bands can be seen more clearly from inspection of typical smaller particles shown in Fig. 4.5. Multiple nuclei of particles arise from strongly bent ribbons (Fig. 4.5a). Large nuclei allow for a larger bending radius and the formation of flat sections of neighbouring structures. The nuclei then agglomerate to gain stability by a graphene-type dispersive interaction between parallel strands of ribbons. The bands rarely wind up in an ordered fashion so as to produce the onion-like particle of Fig. 4.5b. The bands form a 3–dimensional object as can be seen from the frequent oblique projection in random orientation giving the false impression of ”amorphous” regions in the material.

The surface roughness of the particles of Euro IV soot is a consequence of the con-

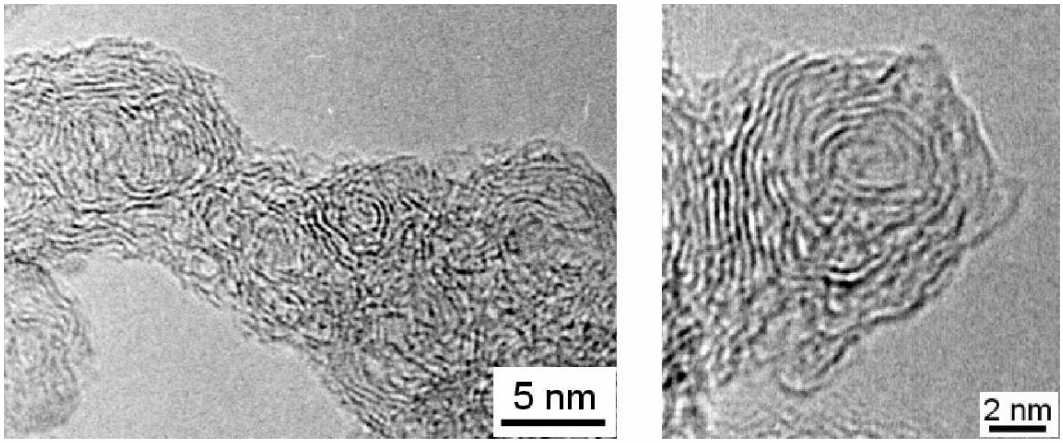

Fig. 4.5: Euro IV soot: a) Fullerenoid agglomerate, b) a small particle situated on larger agglomerate.

tinuous nucleation of new bands at the pre–formed particle. The HRTEM images show small objects nucleated on top of clusters of ribbons. They are single, continuously bent carbon objects with the smaller ones having a diameter typical of a fullerene molecule (see inset in Fig. 4.6). The continuous bending indeed implies the presence of a sizeable fraction of non–6–membered carbon rings and qualifies the graphenes as fullerenoid objects probably characterized by an electronic structure being hybrid between semimetallic and polyolefinic with localized double bonds at the non–6–membered carbon rings.

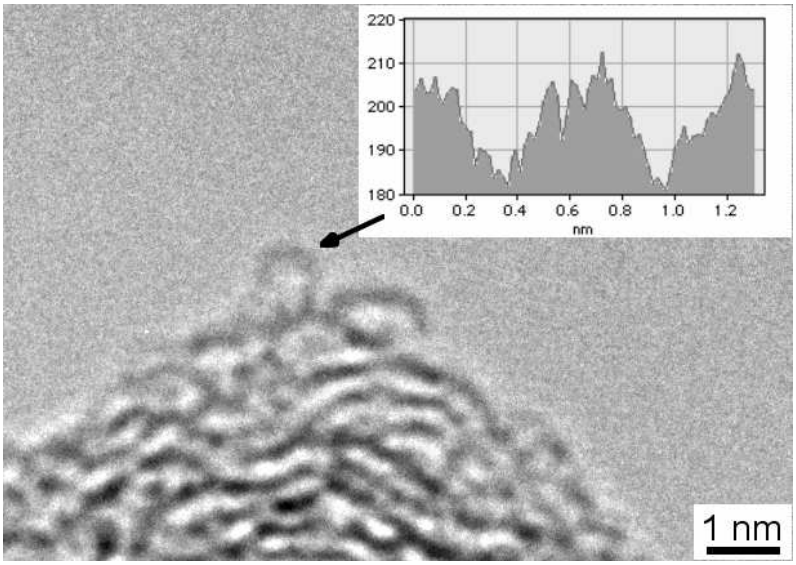

Fig. 4.6: Fullerenoid object attached to the surface of a large soot particle. The inset shows that the diameter of the object is in the size range of a single fullerene molecule.

It is obvious that the modification of reaction conditions in low emission engines as compared to the older engines brings about new qualities of soot. This is no surprise as the soot formation, as a kinetically controlled reaction sequence, will be sensitive to boundary conditions. The ribbon–like interlaced structure of the Euro IV soot is reminiscent of glassy carbon, which exhibits the same general morphology. This indicates that formation temperatures relevant for the Euro IV soot are much higher than the formation temperatures of the investigated Euro III soot or black smoke soot. Only fast growing graphene units with many ring–size defects survive and find no time for the formation of aromatic structures that would allow a substantial gain in energy. During short periods the carbon source becomes rich, allowing fullerenoid elements to form. The short duration of the feed–rich episodes prevents the formation of regular onion–like carbon and results in the irregularly interconnected fragments found in fullerene soot [38]. The general morphology

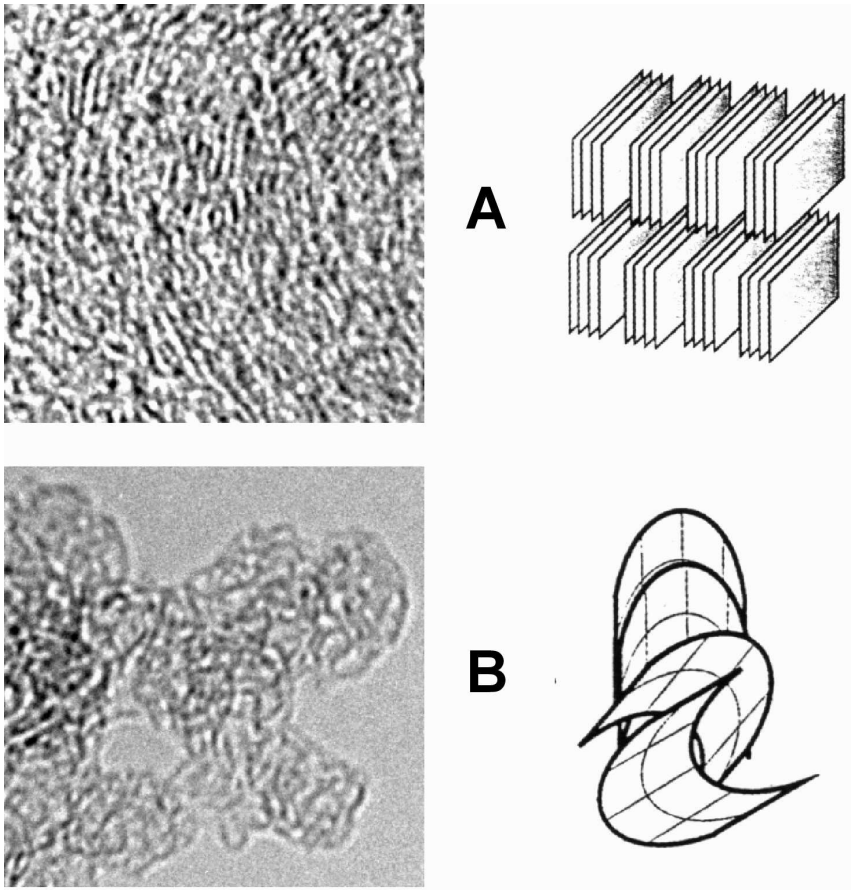

Fig. 4.7: a) shows the arrangement of stacks of planar graphene units. Only few of these stacks are oriented with the a-axis parallel to the electron beam and can be imaged as illustrated in the sketch. The majority are randomly oriented and give hence an amorphous contrast; b) represents bent sheets which are stacked concentrically and randomly.

of the graphene segments can be viewed in Fig. 4.7. In general one can divide the subunits of the diesel engine soot into stacked planar graphenes and curved fullerenoid graphene structures. To this end model substances are synthesized and investigated with TEM and TPO in order to understand the contribution to reactivity from both structures. This will be intensively discussed in chapter 6 [39,40].

4.1.4 Investigation of Model Substances

Soot Model substances are neccessary in order to understand the microstructure, electronic structure and reactivity correlations in carbonaceous marterials. To this end Giant Polyaromatic Hydrocarbons (GPAH) are synthesized as models for the graphite like BSUs. Several pathways for the synthesis of such GPAHs are described in the literature, oxidative cyclodehydrogenation of hexaphenylbenzene (1, HPB) with copper(II) triflate and aluminum(III) trichloride is applied in order to obtain the materials [41,42].

Flat Model Carbons

Hexabenzocoronene ($C_{42}H_{18}$) and the larger molecule ($C_{96}H_{24}$) are chosen as models of flat layers as already resolved in the soot materials. In Fig. 4.8 representative micrographs are given. In the case of the $C_{42}H_{18}$ stacks of several nm length can be observed (inset in Fig. 4.8a). These columns consist of the GPAH layers in a fishbone like structure and are slightly inclined [42].

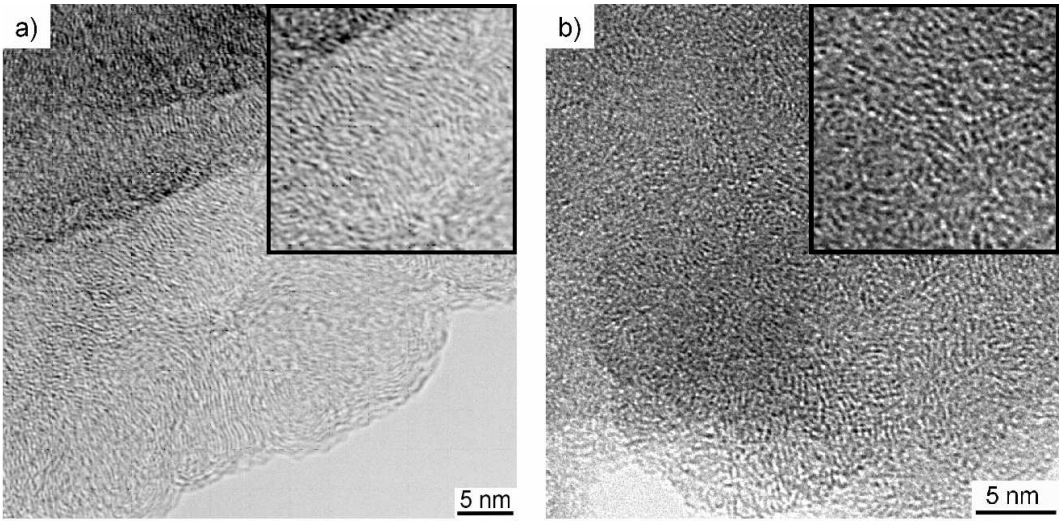

Fig. 4.8: Stacked Giant Polyaromatic Haydrocarbons. a) $C_{42}H_{18}$, b) $C_{96}H_{24}$.

The other model carbon $C_{96}H_{24}$ also exhibits stacks of molecules. From MALDI-

TOF measurements it is known that particles of up to 7 disks can be measured [43]. These columns are clearly visualized in the HRTEM images. Stacks of 6–7 GPAHs are observable (inset in Fig. 4.8b). This demands that the disks are oriented in such a way that the electron beam passes parallel to the disk plane. The misoriented disks contribute to the apparent disordered background surrounding the columns.

Curved Model Carbons

The soot microstroctural investigations show clearly, that the graphenes serving as basic structural units are not flat. They tend to be rich in defects and bent. This bending could only be understood from the assumption that non–hexagonal units are involved and thus destroying the hexagonal structure. In addition to this it is well known that a deviation from the aromatic electronic structure leads to a polyolefinic structure with localized double bondings. This leads to strain in the flat graphene layer and in this case to a bending or more rolling and twisting of the bands. This microstructure is then more similar to interwoven carbonaceous bands. The structures are depicted in Fig. 4.9.

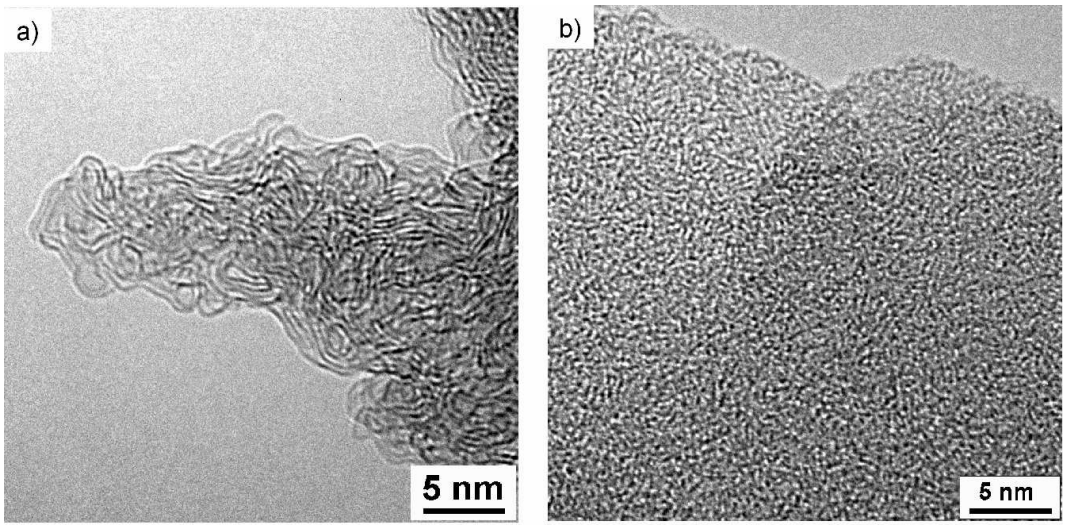

Fig. 4.9: Graphene model substances, a) Graphene Ribbon, b) $C_{90}H_{36}$.

Fig. 4.9a shows a phase contrast image of graphene ribbons wound up in a disordered way due to the molecular strain described above. The molecule depicted in Fig. 4.9b has three five membered rings incorporated. This deviation from planarity suppresses a regular stacking as revealed for the flat molecules. The image shows a high disorder.

4.1.5 Comparative Analysis of Soot and Carbon Black

In this section the diesel engine soot is compared to other soot and carbon black materials. A detailed investigation is carried out on GfG soot, Furnace Soot and Lamp Black. The GfG Soot is obtained by a spark discharge method [44–46]. The Furnace Soot (FW 1) and the Lamp Black (FR 101/33 D) are industrial carbon blacks produced by DEGUSSA. The investigated Black Smoke soot (BS soot) is also a diesel engine soot that evolves from the engine if the diesel fuel is combusted in an under–stoichiometric air to fuel ratio.

Fig. 4.10 shows HRTEM micrographs of the investigated carbon materials. The GfG soot (Fig. 4.10a) consists of small particles. Spherical particles are not larger than 3 nm and seldom observed. The graphene segments are strongly bent forming single or double-layered fullerenoid-like structures, coagulated to long chainlike agglomerates.

The BS soot (Fig. 4.10b) consists of typical spherical particles with a median diameter of 24 ± 7 nm. A disordered core of about 2 – 4 nm is clearly observed. The outer parts of the spheres are built of homogeneously sized flat BSUs. The interplanar distances of the graphenes range from 3.4 to 3.5 Å, thus being larger than the typical plane distance in graphite (3.35 Å). The spherical particles exhibit a very smooth surface, with few irregularities.

The high resolution TEM image of BS soot (Figure 4.10b) reveals the common morphology of a spherical secondary structure made from homogeneously sized flat BSUs which are stacked such that the interplanar interaction is maximised while the outer surface area is minimised. A similar gross morphology is observed in technical products of carbon black from understoichiometric low temperature flame pyrolysis of hydrocarbons. The smooth outer surface of the particles indicates a long reaction time to reach a minimum energy situation or a post–synthesis oxidative episode that burnt away surface irregularities.

A very similar morphology is observed in the case of the Furnace Soot (Fig. 4.10c). The particles are slightly smaller than those of the BS soot (median size of about (24 ± 3) nm). The gross morphology is similar. One observes the disordered core and the graphitic outer part of the spherical soot particles.

The electron micrograph in Fig. 4.10d reveals the typical microstructure of the outer part of a Lamp Black particle thin enough for high–resolution imaging. It consists of spherical primary particles with a mean size of about 110 nm, also agglomerated in chain-like secondary structure typical of carbon black. Homogeneously sized flat BSUs forming planar graphene layers, some with small curvatures are predominant. The image exhibits a fringe contrast region as thick as several tenths

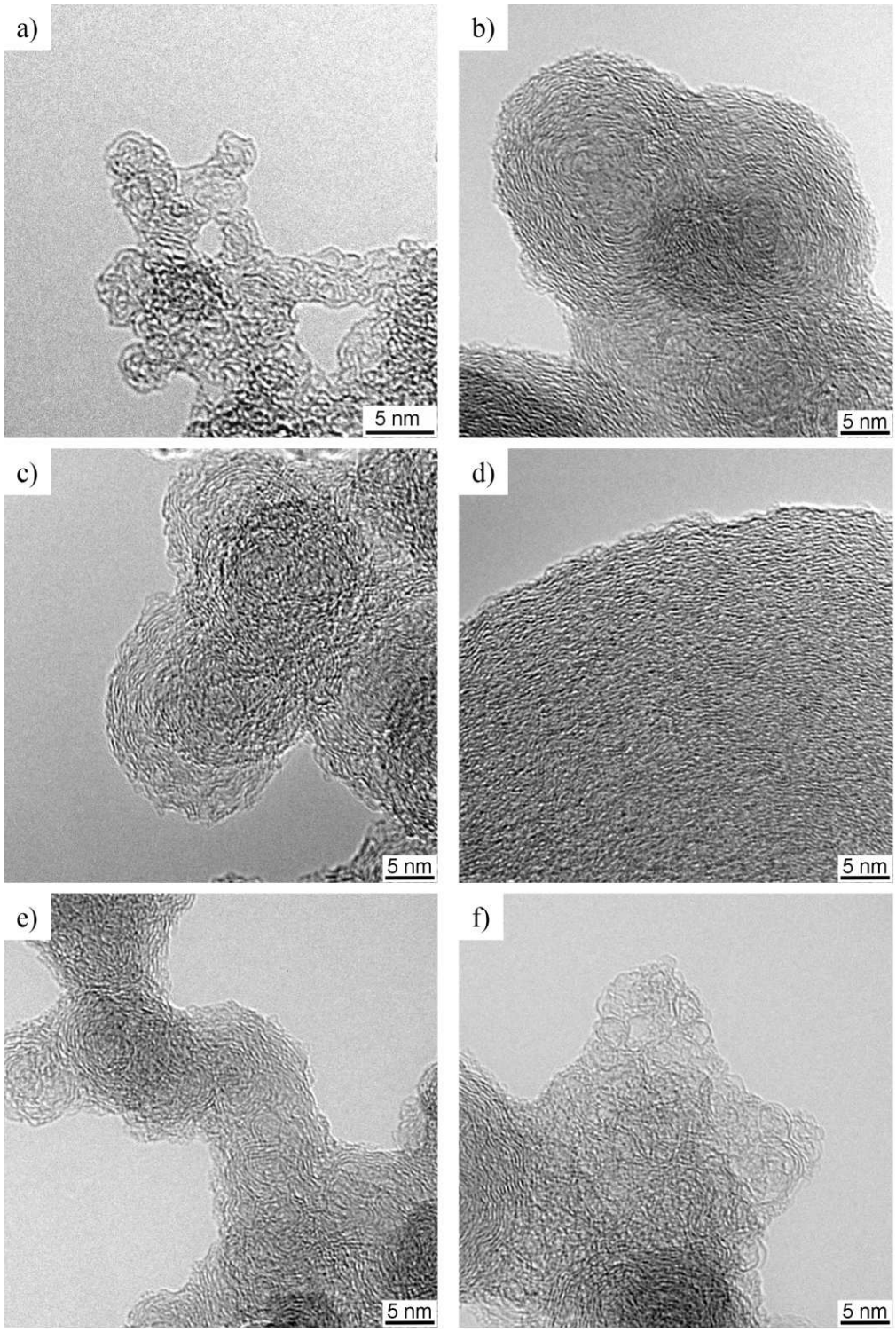

Fig. 4.10: HRTEM micrographs of the investigated carbon materials: a) GfG Soot, b) BS soot, c) Furnace Soot, d) Lamp Black, e, f) Euro IV HD diesel engine soot.

of nanometer. The core part of the Lamp Black particles gives a too bad contrast due to the large diameter of the particles and the resulting thickness at the core.

The Euro IV HD diesel engine soot shows a different morphology compared to the industrial sample. The high resolution electron micrograph (Fig. 4.10e, f) shows that the spherical particles (18 $\pm$ 6) nm are in a minority. Small primary particles coagulate to chainlike agglomerates. The agglomerates are built of small nuclei in the size of 10 to 15 nm. The surface is dominated by irregularities. Small fullerenoid particles with a deformed onion–like structure (2–3 nm in diameter) are observed. A considerable fraction shows a morphology similar to spark discharge soot. The detailed analysis has already been given in the section 4.1.3.

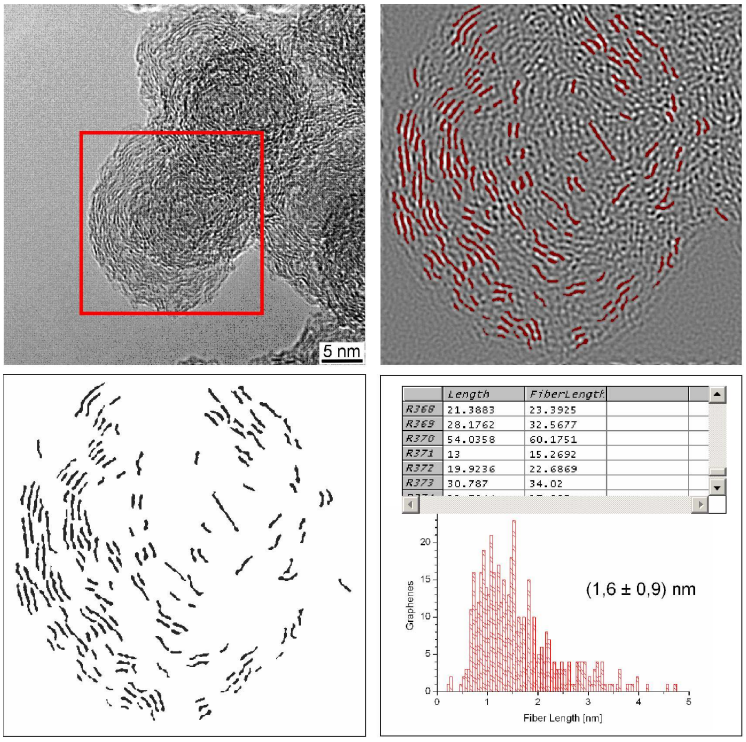

Fig. 4.11: Extraction of graphene sizes fron HRTEM images of soot. Image – Selection – Threshold Analysis – Particle Selection – Analysis of Particles – Histogram.

For quantitative treatment of the TEM fringe images, the complex phase contrast image has to be converted into a set of distinct, identifiable fringes that can be analyzed by image analysis algorithms. The section below outlines a preprocessing procedure which while not unique or free from subjectivity is a procedure that yields reproducible fringe populations that reveal the essential differences between samples. The processing procedure involves the separate steps of fourier transform filtering, binary image conversion, skeletonization, post–processing and quantitative analysis of structure.

To evaluate the HRTEM images a lattice fringe analysis with the DIGITAL MICROGRAPH software package by GATAN is performed. The basic steps are: 1) applying a background offset and spatial filter to correct for background, image illumination and quality; 2) thresholding to isolate the lattice fringes and 3) selecting fringes to rule out artifacts such as sharp bends or joint fringes as well as contributions from ”noise”. These steps create a binary image, effectively isolating the lattice fringes as discrete line segments [47–49]. The program tabulates the length of each fringe. A histogram is readily created from such data (Fig. 4.11).

The further approach is then to keep the single threshold value for preliminary identification and then to identify the aggregate structures. After the threshold procedure further steps are taken including removal of small fringes. To evaluate the HRTEM images a lattice fringe analysis with the DIGITAL MICROGRAPH software package by GATAN is performed. The program tabulates the length of each fringe. A histogram is readily created from such data (Fig. 4.11). The advantage of the fringe analysis is that it is sensitive to the level of molecular organization (nanostructure) of soot.

Table 4.1: Graphene sizes curvature values deduced from HRTEM micrographs of the soots and carbon blacks.

	Size [nm]	Curvature
GfG Soot	1.3 ± 0.5	0.79 ± 0.08
Euro IV Soot	1.4 ± 0.8	0.83 ± 0.06
BS Soot	1.6 ± 0.9	0.87 ± 0.04
Furnace Soot	1.6 ± 0.9	0.85 ± 0.05
Lamp Black	1.7 ± 0.7	0.88 ± 0.03

These advantages distinguish it from traditional methods of Raman Spectroscopy (see [50,51]) and X–ray diffraction that provide an averaged measure of the graphitic structure and cannot provide a direct visualization of the molecular level structure. It is possible to deduce graphene sizes (Table: 4.1). The size of the graphenes varies with the different carbons. The curvature is acquired in measuring the length and fiber length of the graphenes (Fig. 4.11). The ratio (Equation 4.1) defines the curvature.

$$\text{Curvature} = \frac{\text{Length}}{\text{Fiber Length}} \tag{4.1}$$

In the case of the GfG soot the graphenes are small and strongly bent. In the case of the Lamp Black, the graphenes are large and flat (see Fig. 4.12). The relative broad distribution of curvature in the case of the GfG Soot displays the non–uniform

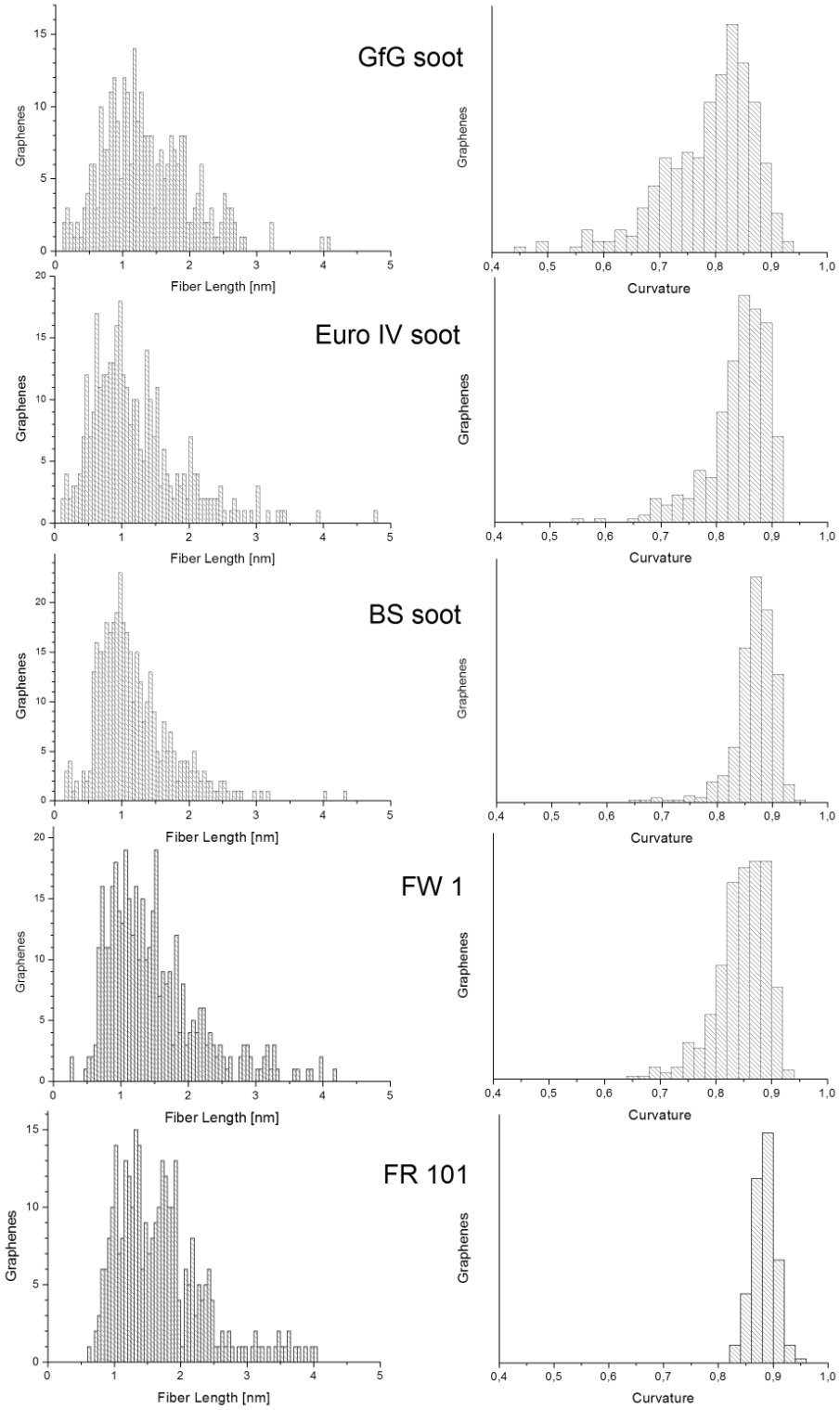

Fig. 4.12: Extracted graphene size and curvature distributions from the investigated soot and carbon black materials.

shape of the graphenes. In the case of the Lamp Black, the graphenes are flat, as seen in the HRTEM images. In the spherical particles the formation of small crystallites is preferred.

4.2 EELS Work

4.2.1 General EELS Analysis

The EELS carbon K (1s) near–edge structures have been recorded for the structures described in section 4.1.4 and section 4.1.5. The results are displayed in Fig. 4.13 and 4.14. In all cases the electron beam propagates parallel or tangential to the graphene layers plane. It gives rise to scattering events incorporating momentum transfer parallel as well as perpendicular to the local c axis of the layered structure. Together with the values of the angles of illumination and collection used, these experimental conditions average out anisotropy effects. The sharp peak at 285 eV is due to the transition from 1s to π* states, while the four peaks at higher energy loss correspond to the σ^* region 290—310 eV. There is a systematic evolution in the edge structures of the spectra as the curvature radius of the graphenes decreases and the graphitization increases. For a thorough investigation the spectra are acquired from different places in the samples. The measured spectra are treated with a background removal following the power law. The measurements are carried out as follows: The EELS spectra are acquired under magic angle conditions (see below) and are averaged in order to have the possibility to show the difference in electronic structure. To avoid contributions from plural scattering, the spectra are deconvoluted from the zero–loss peak.

Model Substances

The Model substances are also investigated by means of energy loss spectrometry. The spectra are overall more homogeneous indicating the pure carbon material.

In Figure 4.13, the resulting spectra are shown. All the spectra show a contribution from the π^* prepeak at 285 eV energy loss. the second feature is then the σ^* feature. In this a dominant peak at 292 eV is clearly visible. This feature is most prominent for the samples building up the stacks ($C_{42}H_{18}$, $C_{96}H_{30}$) as visualized in the HRTEM investigations. This feature is less prominent for the curved samples ($C_{90}H_{36}$, Graphene Ribbon). Especially in the case of the Graphene Ribbon sample the π^* prepeak is the least prominent. The overall σ^* feature is different from the other samples showing the highest intensity at 302 eV. This seems to be the effect of

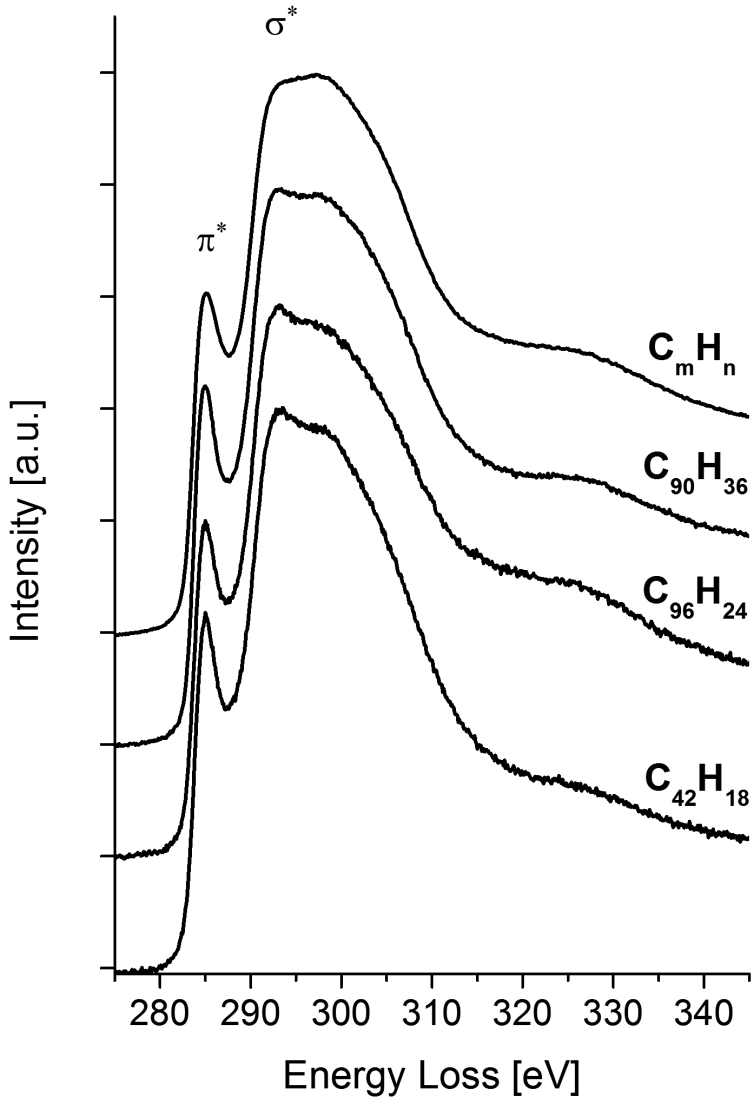

Fig. 4.13: Averaged EELS spectra obtained from the polymers. The spectra are offset for clarity.

the rather polyolefinic electronic structure that stems from localized double bonds. The HRTEM images show the long strands of ribbons wound and curled up. This suppresses the π electronic structure, also clearly indicated by the low π^* feature at 285 eV.

Soot and Carbon Black

To first analyse the electronic structure of the soot and carbon black materials the EELS measurements are shown in Fig. 4.14. The carbon–K ionization edge reveals the bonding properties predominant in the carbons.

The measurements are carried out as follows: The EELS spectra are acquired under magic angle conditions (see below) and are averaged in order to have the possibility to show the difference in electronic structure.

From the spectra, the different intensities in energy losses at 285 eV and 292 eV (Fig. 4.14) are observed. This shows that the predominant bonding behavior is different in the soot materials ranging from disordered to graphitic. The presence of the π^* peak (labeled π^*) at 285 eV in all the carbon samples is characteristic of π bonds in sp^2–coordinated carbon. The comparison of the spectra of the different soot and carbon black materials in comparison to the graphite shows that all samples exhibit a predominant sp^2–rich form. The main trend in all spectra is the loss of fine structure at $\Delta E > 296$ eV and a fluctuation of the relative intensities of the π^* and σ^* peaks. An additional feature in the spectra, between the σ^* and π^* peaks at $\Delta E = (287 \pm 1)$ eV, is usually assigned to C–H bonds.

4.2.2 sp^2/sp^3 Quantification

In graphite, the highly anisotropic material, the EEL spectra show different shapes depending on the orientation of the sample. This is due to the interaction of electrons with respect to that of the principle axis of the anisotropic material. Thus, the detected inelastic scattering will encompass a range of momentum transfers at various orientations, the extent of which is dependent on the experimental conditions. The orientation dependence of the EELS core edges in anisotropic can be ruled out as described 3.2.7 in choosing a set of combinations for incident and collection angle.

EELS measurements show the electronic structure of the carbon materials. The carbon–K–ionization edge is sensitive to the bonding behavior of the carbon [30,52]. It is possible to deduce a predominant hybridization of the carbon orbitals.

In order to avoid the influence of anisotropy orientation all measurements were

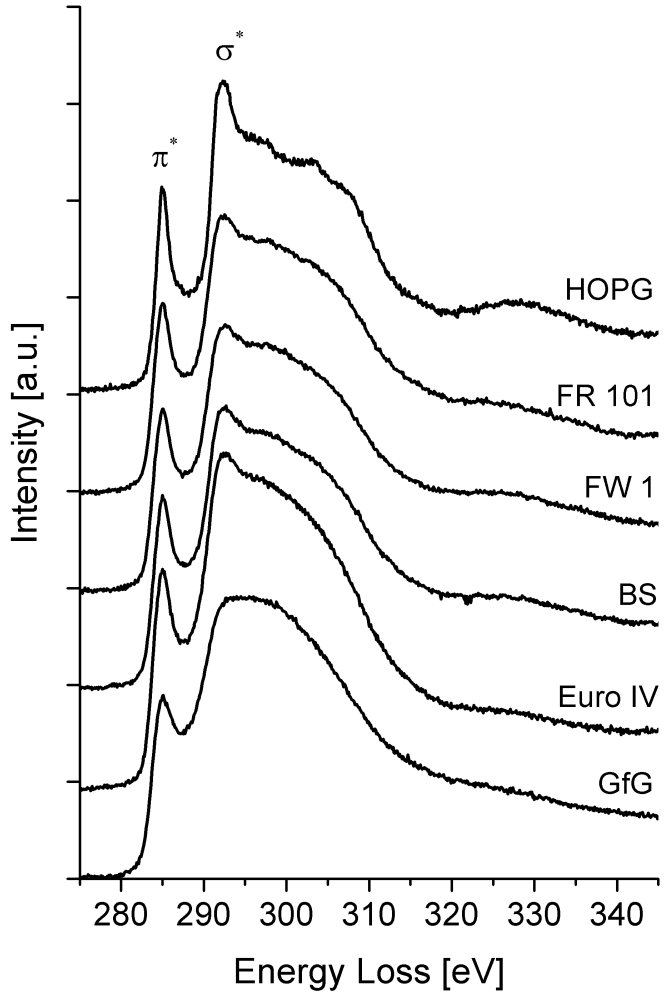

Fig. 4.14: Averaged EELS spectra obtained from the soot and carbon black materials. The spectra are offset for clarity.

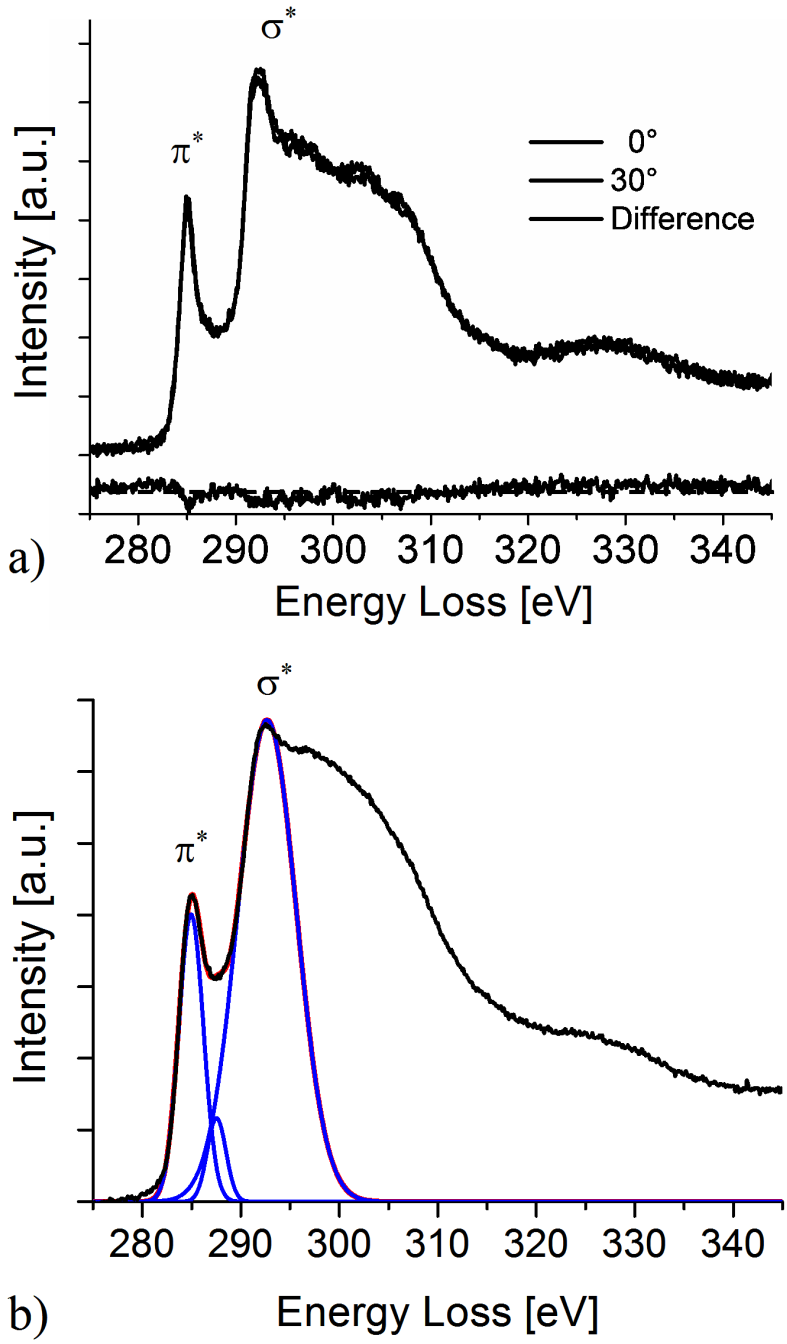

Fig. 4.15: Quantification of sp^2/sp^3 hybridization ratio with EELS, a) shows the independence of the graphite reference spectra for different orientations, b) shows the fit leading to the hybridization ratio.

carried out in the so called "magic–angle–condition" i.e. α = 0.8 mrad and β = 1.38 mrad. These values are in accordance with $2\vartheta_E$ [53], where ϑ_E = 0.83 mrad is the characteristic scattering angle. However due to the difference to the proposed angle $4\vartheta_E$ [54, 55] the correct settings were verified with a HOPG crystal were no changes in the carbon–K ionization edge where found when tilting the sample out of the (002) orientation (Fig. 4.15).

To acquire the respective EELS spectra and to be able to perform a thorough investigation of average predominant spectral features, several spectra are acquired for each sample. As the spectra are acquired in diffraction mode, the area from which the information stems is given by the projected diameter of the smallest SAD–aperture used in the microscope. The diameter is d = 189 nm, leading to an area of 0.028 μm^2. They are also processed with a background removal and deconvoluted. A weighted average is calculated for each sample.

Assuming that the intensity of carbon–K ionization edge represents the density of anti–bonding states located within the electron probe volume it is possible to determine the relative amounts of π- and σ-bonded carbon from the relative intensities of the π and σ features in the near-edge structure. To estimate the fraction of π and σ bonds, it is assumed that the ratio of integrated areas under the π^* peak and the σ^* peak is proportional to N_π/N_σ, the ratio of the density of π and σ states. This ratio is normalized with respect to the value determined for HOPG, the material only consisting of carbon in a sp^2 hybridization. Thus it is possible to deduce the sp^2/sp^3 hybridization ratio in applying equation (4.2).

$$\mathrm{sp}^2 = \frac{\left[\dfrac{\mathrm{area}(\pi^*)}{\mathrm{area}(\pi^* + \sigma^*)}\right]_{\mathrm{sample}}}{\left[\dfrac{\mathrm{area}(\pi^*)}{\mathrm{area}(\pi^* + \sigma^*)}\right]_{100\%\ \mathrm{sp}^2\ \mathrm{reference}}} \tag{4.2}$$

The hybridization ratio is acquired in applying a Gauss fit to the spectra (Fig. 4.15) and comparing the different areas of the respective Gauss curves [33, 56, 57]. This gives the ratios as displayed in Table 4.2. The graphitization is high in the carbon samples with larger spheres and planar graphite microcrystals. This is evidenced by the high Nsp^2 ratio in the Lamp Black, the Furnace Soot and the BS soot. The lower Nsp^2 is due to the high disordered structure and the bent graphenes as in the Euro IV and even more in the GfG soot.

Table 4.2: Quantification of the sp^2/sp^3 hybridization ratio from the EELS experiments.

	Nsp^2 %	Nsp^3 %
GfG Soot	54	46
Euro IV Soot	66	34
BS Soot	76	24
Furnace Soot	77	23
Lamp Black	77	23
Graphite	100	0

4.3 Discussion

In the following discussion, the task is to link the microstructure of the investigated carbon materials to their origin in the flames and, which is more important, to the soot generation in the diesel engine.

As revealed by the measurements with TEM and EELS, the morphology of the soot samples is different with respect to their origin of combustion. The shorter the time of generation is, the smaller the spherical graphitic particles are [36, 58, 59]. In fact, the lack of such particles in the GfG soot underlines these findings. The Furnace soot and the Lamp Black have a comparatively longer development time. A large amount of precursor molecules is available for surface growth. In this way, the spherical particles can form and undergo a surface minimization and build up the regular spherical particles with the uniform size distribution.

In rich hydrocarbon flames there are carbon–rich particles with one–, two–, and three–dimensional carbon backbones that also occur as intrinsic ions in the flame. In order to understand the general morphology of the soot and carbon black particles investigated in this work it is necessary to understand the theory of soot formation [60–69].

Temperatures in combustion systems range from 1200 to 2000 °C and there is generally sufficient oxygen in the system for the substantial combustion of the fuel. The total amount of soot formed under these conditions is usually very small compared to the amount of carbon present in the fuel consumed. Under these conditions, the time typically available for the formation of soot is in the order of a few milliseconds. During this time, some of the fuel is transformed to give rise to the soot particles (Fig. 4.16). The resulting aerosol can be characterized by the total amount of the condensed phase, expressed as the soot volume fraction.

Diesel engine design and operating parameters such as injection timing and pressure, compression ratio and inlet port design influence soot emissions by affecting

the size and time/temperature history of soot forming and oxidizing regions in the combustion chamber. Design and operating parameters impact the more fundamental parameters that are important in soot formation/oxidation in laboratory studies. Relatively few of the directly controllable parameters impact the more fundamental quantities, such as amount of incompletely mixed fuel and its equivalence ratio, rate of mixing, flame temperature, soot burnup, fuel type, gas temperature, oxygen availability and time availability [70]. The relation between ignition

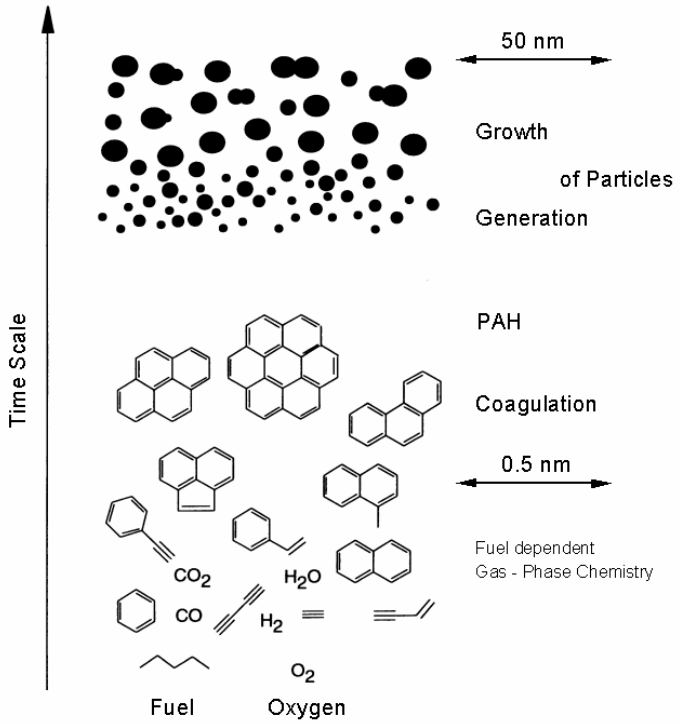

Fig. 4.16: Particulate growth during soot formation. Hydrocarbons form the first aromatic rings that result in polyaromatic hydrocarbons. Coagulation leads to growth of soot particles.

timing and ignition delay is particularly important. For fuel injected prior to ignition, atomization and evaporation results in a gaseous mixture not unlike that of a rich premixed flame. Fuel injected subsequent to ignition, however, burns before much mixing can occur, resulting in a diffusion flame. In the case of the direct injection engine evaporation of fuel droplets take place near the point of injection producing an extremely fuel rich vapor jet. This generally occurs under conditions supercritical with respect to the various chemical components of the droplet so that transition to the vapor phase is expected to be extremely rapid. Near the edge of the fuel jet, mixing with the surrounding air takes place by turbulent diffusion, producing a combustible vapor. There, the combustion takes place at a rate controlled by the turbulent fuel–air mixing. After evaporation from the droplet surface, a fuel

molecule will undergo pyrolysis in the region between the surface and the heat release source. In this region the concentration of oxidizing species is small, nevertheless due to the mechanism by which pyrolysis reactions occur, it may play a significant role.

The general soot formation can be understood via a mechanism, being a "competition" between soot and fullerene formation [38]. The controversy, whether initial soot particles in flames are formed by a fullerene mechanism or vice versa, can be resolved by the currently available experimental studies that indicate that both species have common precursors. These precursor particles are usually termed aromers. It has thus far only been possible to draw indirect conclusions with respect to their properties. They possess aromatic partial structures and are rich in hydrogen.

The first condensed phase material arises from the fuel–molecules via their oxidation and/or pyrolysis products. Such products typically include various unsaturated hydrocarbons, particularly acetylene and its higher analogues ($C_{2n}H_2$), and polycyclic aromatic hydrocarbons [71]. The most common structural element of PAHs is the hexagon of benzene. The structural variety is increased by the addition of pentagons. The existence of five–membered rings in PAHs is of particular interest with respect to fullerene formation. When five-membered rings are bordered by hexagons on not more than two adjacent edges, the molecule is still nearly planar as seen in dicyclopentapyrene. The bowl–shaped structure of corannulene is markedly different; here a five–membered ring is bordered on all sides by hexagons. In flames, PAHs also exist as both σ and π radicals. In the former species, the unpaired electron is located in a σ orbital, while in the latter it is found in a π orbital. PAHs also exist in protonated or ionized form.

From the growth of PAHs it is known that all particles with open edges can grow by binding acetylene. In the relatively hot interior of benzene/oxygen flames there are fullerenes found and measured, but no soot. Soot forms only in the less–hot edge zone, where only very few fullerenes are found. In combination with the observation that acetylene–rich flames contain few fullerenes, but a lot of soot, as long as the temperature is not too high, this temperature effect, together with the model of aromers as precursors for both types of large particles, yields the following overall picture that is summarized in Fig. 4.17. High temperature environments containing relatively low concentrations of small unsaturated hydrocarbons, favor unimolecular reactions of aromers. This includes the "zipper reactions" leading to fullerenes, but also general degradation reactions, so that it is conceivable that very large particles are not formed at all. If the temperature is lower and small growth components (such as acetylene) are present in higher concentrations, bimolecular

reactions of aromers dominate, which do not provide enough time for cage closure but instead lead rapidly to small soot particles. It is important to note that these reactions occur with particles that contain aromatic partial structures, but are no longer overall planar. In the case of normal PAHs, these alternatives would either lead only to degradation or to growth up to the stability limit for planar particles.

The condensation reactions of gas phase species such as these led to the appearance of the first recogniseable soot particles. These first particles are very small (d < 20 Å) and the formation of them involves a negligible soot loading in the region of their formation, which is generally confined to the most reactive regions of the flame – i.e. in the vicinity of the primary reaction zone. Nucleation of soot particles occur in the pyrolysis zone, depending on the residence time and the temperature histories of the fuel molecules. These histories depend primarily on the thermodynamic properties of the fuel and the rate of mixing. The oxidation rate decreases as quickly, as the gas temperature decays to ambient cylinder values.

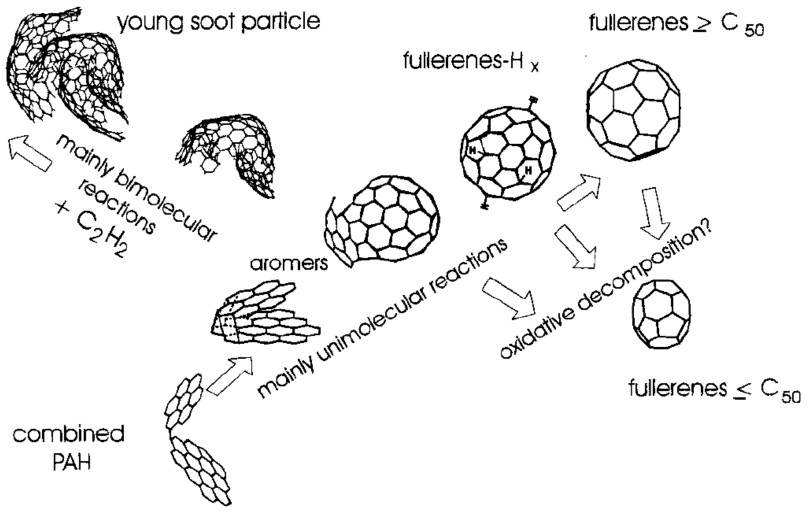

Fig. 4.17: Particle formation, a process leading to soot particles via bimolecular reactions or fullerenes via unimolecular reactions. Adapted from [66, 72]

Fuel–rich combustion under normal pressures (relatively high density of small unsaturated hydrocarbons) but with air instead of pure oxygen (lower temperature) favors the formation of soot (see, for example, the HRTEM images of BS soot, Furnace soot, and Lamp Black). Special flames, however, allow the adjustment of conditions (low pressure, a specific temperature range, aromatic fuel) in such a manner that the large particles formed in small amounts are exclusively fullerenes, formed by essentially unimolecular reactions from aromer precursors, while no soot is formed [66, 72]. This becomes evident if one considers the HRTEM micrographs of the GfG soot and the Euro IV soot.

In the case of the Euro IV HD soot one observes a different morphology probably due to the higher air/fuel ratio in the engine piston compared to the case of the BS soot. The occurence of fullerene-like soot in a non-stationary high-pressure (P_{max}: $13{\cdot}10^4$ Torr) flame by the combustion of diesel fuel in the new low-emission engine, is unexpected. The low sulphur type diesel fuel consists of 78% aliphatic and cycloaliphatic hydrocarbons and 22% aromatic hydrocarbons with 6 ppm sulphur. Combustion in diesel engines is featured by the fact that it is not a premixed, homogenous burning process, but rather an inhomogeneous one with a gradient of stoichiometric air/fuel ratios (smaller than one). Usually, the incomplete combustion under such conditions leads to the formation of spherical soot particles of 30–100 nm in diameter, in our case the Euro IV HD diesel engine soot or the BS soot desribed in the work (see section 4.1.5). The fact that small particles are detected in the exhaust of the new low-emission diesel engine could result from the improved mixing behavior of diesel fuel and air (air/fuel $>$ 1.3) in the combustion. Therefore, the formation of fullerene–like soot could be an indicator of the optimised combustion process. The conditions of nucleation and growth (supersaturation, temperature) in the carbon–forming volume of the engine will thus determine the abundance of well–ordered particles vs. the irregular objects seen in Fig. 4.5a. and that constitute the vast majority of objects in the Euro IV soot samples.

Soot particles are definitely three–dimensional. Even if it were possible to assign a definite molecular formula C_xH_y to a given soot particle, this would be rather useless as it is shown in TEM and HRTEM investigations throughout this work, that no two soot particles are alike. Fullerene molecules are hollow. Soot particles have filled interiors. A limited similarity can be found in the forms of the two species. One must, however, consider some special cases, both for fullerenes and for soot particles. There are soot particles that exhibit a nearly perfectly spherical shape, as seen in the BS soot, in the Furnace Soot and in the Lamp Black. The spherical shape for soot particles is the result of that following growth mechanism. These quite round particles were able to grow by the surface degradation of small hydrocarbon molecules. During growth, no coagulation with other soot particles occurred (quite accidentally). These turbostratically arranged layer segments exhibit an interlayer distance slightly larger than that found for graphite. During growth at flame temperatures, it is assumed that they can shift with respect to each other at the surface and thereby briefly form, in effect, a two–dimensional liquid. This forms the spherical particles in the fuel rich environments.

Surface growth, by which the bulk of the solid phase material is generated, involves the attachment of gas phase species to the surface of the particles and their incorporation into the particulate phase. Here the condensation of species with the

right hydrogen content; or condensation of species with a higher hydrogen content followed by dehydrogenation; or a combination of both.

Hence, the eventually spherical shape arises from a dynamic process, which leads to other shapes when particles coagulate during growth. The depiction of a soot particle in Fig. 4.18 should not be taken literally. It is meant to indicate the (usually only approximate) spherical shape of the particle as well as the layer fragments that are visible under an electron microscope. These layers are oriented in a more or less parallel fashion with respect to the surface and are grouped around a common center. The considerations about the origins of soot and the appearance of the first soot particles might not really be related to the structure of the finished particle. This structure is, in fact, created during the particle growth by the attachment and heterogeneous degradation of small unsaturated hydrocarbons (e.g. acetylene) at the

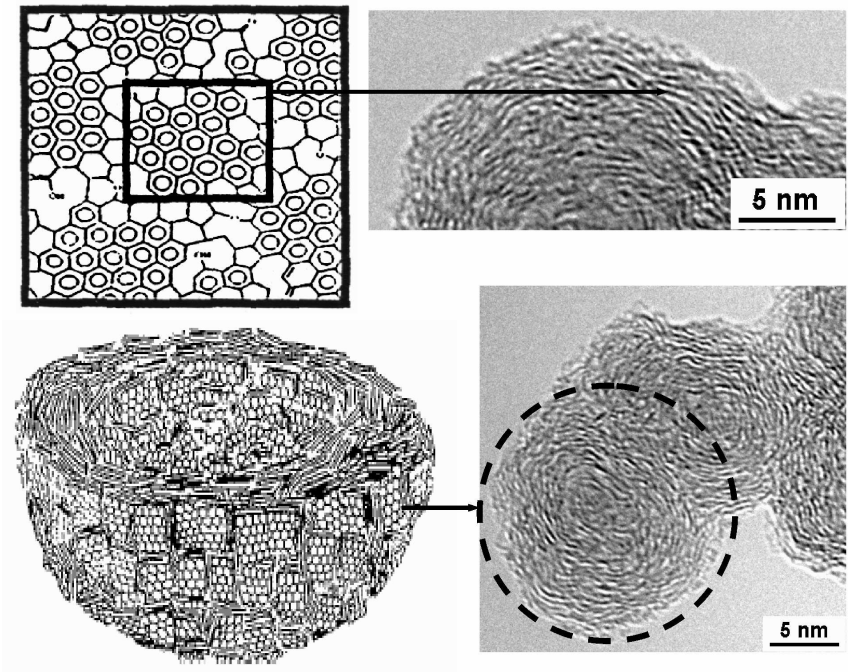

Fig. 4.18: Microstructure of carbon black. The model is built from planar basic structural units (BSU) stacks interconnected by covalent bonds. One BSU is resolved in high resolution TEM of a carbon black particle. The main image shows a projection through an agglomerate of spherical carbon black particles. The distance between the BSU is 0.34 nm, adapted from [73].

surface, tempering processes in the interior accompanied by the loss of hydrogen, and coagulation with other soot particles. For this reason, the detailed knowledge about the morphology of some "finished" soot particles might (maybe not necessarily) be related to their origin and generation. The mechanism by which soot is now believed to be formed from the vapor phase in flames is a mechanism of pyrolysis followed by nucleation. The next step is a competitive process between surface

growth and coagulation of primary particles. The last step is then the aggregation of the soot to form the chainlike agglomerates. Each of these processes is believed to be occurring in diesel engines. It was believed that soot takes the form of more or less spherical aggregates of individual spherical particles in the diesel cylinder, whereas in rich premixed flames, the geometry of fully formed particles is more often a chainlike aggregate.

These models can now explain the Soot and Carbon Black morphology visualized in the TEM. One can clearly distinguish the microstructure of the investigated carbons. The described differences indicated in Figs. 4.3, 4.4, 4.5, 4.6 and 4.10 have a direct correlation to their history of formation. Extremely important is the fuel origin and the time of formation. The availability of fuel plays an additional role.

The images of the GfG soot and the Euro IV soot (Fig. 4.10 a, e, f) reveal a microstructure, that is different from the known carbon black (Fig. 4.10 b, c, d). The carbon is made from units of sp^2 carbon that form interlaced bundles of ribbons with eventual large areas of planar interconnection. The graphenes exhibit a multiple continuous bending. No specific core of particles as typical of onion–like carbons can be identified. The interlacing can be explained by the frequent apparent intersection of the bands leaving, in 2–dimensional projection, the impression of discontinued contrast. The secondary structure of these materials formed from the graphenes can be seen more clearly from inspection of typical smaller particles. Multiple nuclei of particles arise from strongly bent graphenes. Large nuclei allow for a larger bending radius and the formation of flat sections of neighbouring structures. The nuclei then agglomerate to gain stability by a dispersive interaction between parallel and flat graphenes. The conditions of nucleation and growth (supersaturation, temperature) in the carbon-forming process will determine the abundance of well-ordered particles vs. the irregular objects seen in the majority of objects in the Euro IV and GfG soot samples. The graphenes form a 3–dimensional

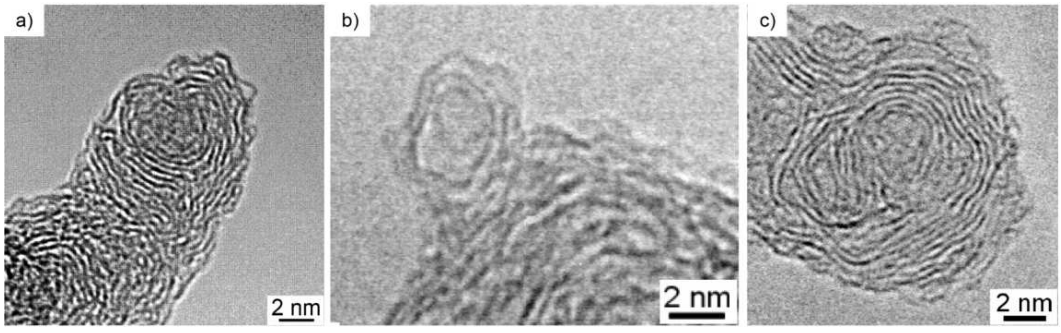

Fig. 4.19: Possible soot particle precursors, a) fullerenoid particle, b) onion like soot particle and c) primary particle with very strongly bent graphene layers.

object as can be seen from the frequently oblique projection in random orientation

giving the false impression of "amorphous" regions in the material. The surface roughness of the particles of the Euro IV Soot is a consequence of the continuous nucleation of new strong bent graphenes at the pre-formed particle, and this process is interrupted by the particle leaving the zone of carbon addition. Such small particles are visualized in Fig. 4.19. The continuous bending of graphenes indeed implies the presence of a sizeable fraction of non–6–membered carbon rings (pentagons in this case) and qualifies the graphenes as fullerenoid objects characterized by an electronic structure being hybrid between semimetallic and polyolefinic with localized double bonds at the non–6–membered carbon rings, a strong deviation from graphitic as revealed by EELS measurements (Fig. 4.14).

The spherical particles as predominant in the BS soot, the Furnace soot and the Lamp Black are similar in appearance. The spheres exhibit a core–shell morphology. The core being roughly 5 nm in diameter appears to be highly disordered. It is assumed that the aliphatic and aromatic fuel molecules break down into olefins and then acetylene by pyrolysis of diesel fuel molecules in the engine. The acetylene molecules grow into large PAHs (1–2 nm) that coagulate to nucleus. They form the core in high–resolution images as inceptions of the soot growth by adsorption of precursor molecules and by graphitization. Around this core, a shell consisting of stacks of graphenes is developed. The spherical shape for soot particles is the result of a certain growth mechanism. These quite round particles were able to grow by the surface degradation of small hydrocarbon molecules. During growth, no coagulation with other soot particles occurs. These turbostratically arranged layer segments exhibit an interlayer distance slightly larger than that found for graphite. During growth at flame temperatures, it is generally assumed that they can shift with respect to each other at the surface and thereby briefly form, in effect, a 2–dimensional liquid. This is only possible if precursor molecules are readily available at moderate temperatures. The spherical shape arises from a dynamic process, which leads to other shapes when particles coagulate during growth. The smooth outer surface of the particles indicates a long reaction time in order to reach a minimum energy situation. A post synthetic oxidative episode may also destroy surface irregularities. This leaves behind the graphitic layer structure in the shell part of the primary particles. The graphene layers are short in length, compared with the well–crystallized graphite, reflecting the dynamic of soot formation under non–stationary conditions. As seen in the HRTEM micrographs the median size of the Lamp Black particles is ~ 110 nm, however the particles often exhibit a considerably larger diameter (up to 300 nm). This morphology apparently is the result of a long developing time in a fuel–rich atmosphere. A continuous dehydrogenation of the fuel molecules lead to the shell structure consisting of large graphenes with a graphitic structure and a low amount of heteroatoms (hydrogen, oxygen). This is

also evidenced by the low amount of oxygen as revealed in the XPS measurements.

The morphology of the soot samples is different with respect to their source from combustion [58]. The shorter the time of combustion is, the smaller the spherical particles are. In fact, the lack of such particles in the GfG soot underlines these findings. In the case of the Euro IV HD soot one observes a different morphology probably due to the higher air/fuel ratio in the engine piston compared to the case of the BS soot. The gross morphology of the Furnace Soot and the BS soot is very similar, one observes spherical particles consisting of a disordered core with a graphitic shell. The Furnace soot has a comparatively longer development time. Additionally, a large amount of precursor molecules is available for surface growth. Apparently during the development of the carbon particles several influences are responsible for the final morphology. The longer the particles stay in a fuel rich atmosphere, the more the particles can attract precursor molecules in order to build the spherical form observed in the HRTEM images. This is even more evident in the case of the Lamp Black (FR 101). The particles have the form of perfect spheres, the size of the particles is relatively large (110 nm). The particles apparently had a relatively long time to develop this morphology.

The size of the graphene layers is quantified according to the procedure described in section 4.1.5. The graphene analysis provides a more comprehensive way of nanostructure analysis (Fig. 4.11). This local structure analysis correlates with the EELS and XPS measurements. The larger and more flat the single graphenes are, the more a crystalline ordered domain is created. This influences the size of the graphenes (Table 4.1). Thus a local ordering is induced. The EELS and XPS measurements correlate to these findings as the graphite like structure influences these integrative methods.

The size of the graphenes varies with the different carbons. In the case of the GfG soot the graphenes are small and strongly bent. In the case of the BS soot for example, the graphenes are large and flat. A fringe analysis of graphenes reveals differences in graphene sizes (Table 4.1, Fig. 4.12).

Nanocarbons from fullerenoid structures should, however, be more reactive than the spherical soot particles as the presence of non–6–membered carbon rings with their olefinic electronic structure and the excessive presence of chemically reactive prism edges tend to destabilise such carbon structures as evidenced in temperature-programmed oxidation studies. In addition, theoretical investigation predicts the influence of geometrical changes in chemical property (increasing reactivity with increasing curvature) of nanocarbons. The reactivity of Euro IV diesel engine soot in abatement strategies is expected to be heterogeneous with a wide spread of reactivity in contrast to homogeneously reactive BS soot. The formation of stable

tertiary structures typical of the BS soot ending up in large arrays of secondary particles will not be as favorable with Euro IV soot due to its surface irregularity. This issue will be investigated and discussed in chapter 6.

The EELS investigations reveal the bonding behavior of the carbon atoms in their surroundings. The displayed core loss spectra characterized by the excitations of electrons from the carbon 1s–orbital to states above the Fermi level. The smaller peak at 285 eV is caused by 1s-π^* transitions and the second one represents the 1s-σ^* transitions. The intensities of the peaks are proportional to the density of unoccupied states. In the disordered materials compared to the graphite, the π^* peak is much broader and seems to have a shoulder between the π^* and the σ^* peak. There are different interpretations for the origin of this additional peak between the 1s-π^* and 1s-σ^* transitions [74, 75]. One possibility is the presence of C=O or C≡C bondings in the sample which should have π^* bands lying in the range between 286-288 eV. C=O groups are clearly present, and measured in the XPS spectra.

Broadening of the π^* features in EELS spectra is also related to the amount of carbon atoms in isolated double bonds vs. carbon in aromatic sextets. A broadening of this feature occurs in X–ray Raman spectroscopy [76].

Another interpretation is that cage–strained π^* electrons present in bent graphitic layers could provide 1s–π^* electronic transitions in this energy range. Small nanotubes with high curvature radius show such shoulders in contrast to large nanotubes [77, 78]. Such spectra especially as in the GfG soot are also obtained from polyhedral carbon onions [79]. The prominent maximum at about 292 eV is the evidence for the formation of graphite clusters consisting of flat 6–membered rings larger than 1.5 nm. The 1s–σ^* band shows slight modifications due to strain in the graphene network [80–84], superimposed on these are contributions of C=O and C–OH bonds as also shown in [85–88].

Another possibility to describe the differences in the ratio between π and σ bonds in different carbons in predominant sp^2–rich form by measuring the ratio of N_π/N_σ [89]. This is expected to rise up to a maximum value to $1/3$ in completely sp^2–coordinated crystalline carbon. It is found that the loss of the fine structure in the σ* region in the spectra of disordered carbons is correlated with a high density of defects and possible vacancies which are expected to induce partially occupied σ bonds at the neighbouring carbon atoms. In diamond–like films it is assumed that uncoordinated σ bonds contribute to defect states in the region of the π density of states and therefore to the π* signal in the EELS spectra. If hydrogen is incorporated in the carbons it gives a signal at $\Delta E = (287 \pm 1)$ eV between the σ* and the π* resonance. This is assigned to electronic states of C–H bonds. At the same energy loss, the 1s–π* transition occur in CO with a natural line with of 0.1 eV [88]. These

influences are then resulting in the over all hybridisation ratio as given in Table 4.2. The higher the overall graphite like crystallinity the higher the Nsp^2 value (Fig. 4.20).

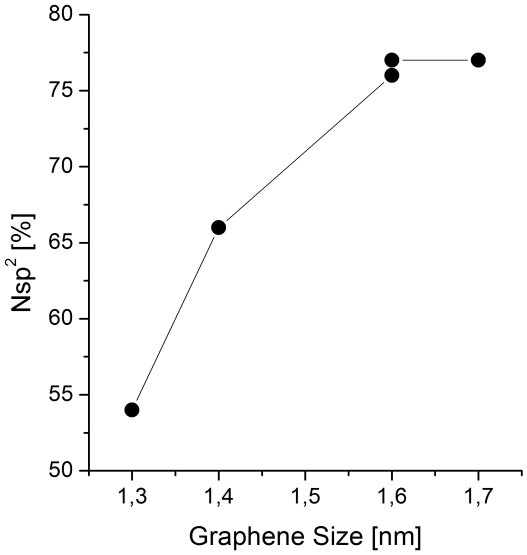

Fig. 4.20: Correlation of graphene size and Nsp^2 value. The larger the graphenes, the higher the Nsp^2 content.

The fact that soot, along with water and carbon dioxide, is observed as a combustion product whenever $C/O > 0.5$, indicates that some of the oxygen is tied up in the relatively stable combustion products CO_2 and H_2O, and is thus unavailable for reaction with C_s on the timescale characteristic of combustion systems. This is explained by the fact that one of the most important oxidizing species in flames OH, is destroyed relatively quickly via interaction with H_2 and CO to form H_2O and CO_2, respectively. Since the reverse of both of these reactions have large activation energies and thus are considerably slower than the corresponding forward reactions at flame temperatures, they effectively tie up oxygen in an unreactive form.

Chapter 5

Surface Investigatons

In this chapter the results of the surface investigations are presented. Section 5.1 shows the results of the DRIFTS measurements, section 5.2 the complementary results obtained with XPS. At the end of this chapter (in section 5.3) the results are discussed in correlation with the obtained insights into microstructure.

5.1 Infrared Spectroscopy

DRIFTS measurements are carried out in order to investigate the oxygen functional groups. In Fig. 5.1 the obtained spectra are given.

Absorption bands arise at different wavenumbers. The GfG Soot shows the highest reflectivity possibly due to the finer particles. There is a broad band centered at 3514 cm $^{-1}$ with two shoulders at 3638 cm^{-1} and 3263 cm^{-1}. These features can be assigned to ν (OH) vibrations. A weak band at about 3070 cm^{-1} originates from C–H stretching vibrations associated with C=C bonds. The bands at 2962, 2932 and 2860 cm^{-1} are characteristic of the ν(CH) vibrations of saturated hydrocarbons, indicating the presence of sp^3 hybridised carbon in this sample. The band at 1726 cm^{-1} represents a ν(CO) vibration. The position of this band is relatively characteristic; tables of vibrations of organic compounds point towards an aromatic ester group [90]. Transferred to the soot this can be interpreted as an ester group attached to the graphenes. The vibration at 1595 cm^{-1} can be either assigned to the stretching vibration of conjugated C=C bonds or to the bending mode of H_2O. The broad absorption from 1460 cm^{-1} to 1100 cm^{-1} is difficult to assign in detail. The two shoulders at approx. 1460 and 1390 cm^{-1} may arise from C–H bending vibrations. The broad and intense absorption between 1300 and 1000 cm^{-1} is assigned to a number of C–O vibrations, suggesting the presence of further oxygenates besides

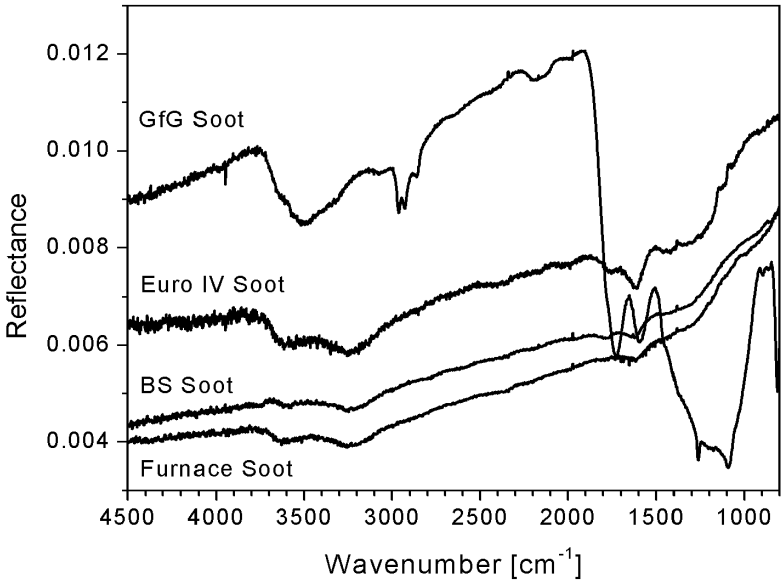

Fig. 5.1: DRIFTS measurements of four soot samples. The GfG soot, the Euro IV soot, the BS soot and the Furnace soot show distinct differences in the spectra.

esters [91].

Among the structural more similar samples, the spectra of the BS Soot and the Furnace Soot show essentially similar features. The bands at 3600 and 3230 cm^{-1} can be assigned to ν (OH) vibrations. The absorption at 1750 and 1600 cm^{-1} could be assigned to C=O vibrations and δ (H_2O), respectively. The spectrum of the Euro IV Soot contains the spectral features of the BS Soot and the Furnace Soot. However, it is more functionalized than these two samples. The absorption bands at low wavenumbers are more pronounced than those of the BS Soot and the Furnace Soot exhibits. In addition, the spectrum of the Euro IV Soot exhibits a band at 1440 cm^{-1} indicative of δ (CH) or more likely δ (OH) since ν(CH) are absent.

Unfortunately, the Lamp Black does not give any reasonable spectra due to the very low amount of functional groups and the high absorbance. This motivates a further investigation as carried out with XPS in the following section.

5.2 X-Ray Photoelectron Spectroscopy

XPS experiments are carried out in order to gain information on the surface structure of the carbon materials. The main emphasis is put on the analysis of the Carbon C1s (Figs. 5.2 and 5.3) and O1s spectra (Fig. 5.4). The spectra were processed with

a Shirley background removal.

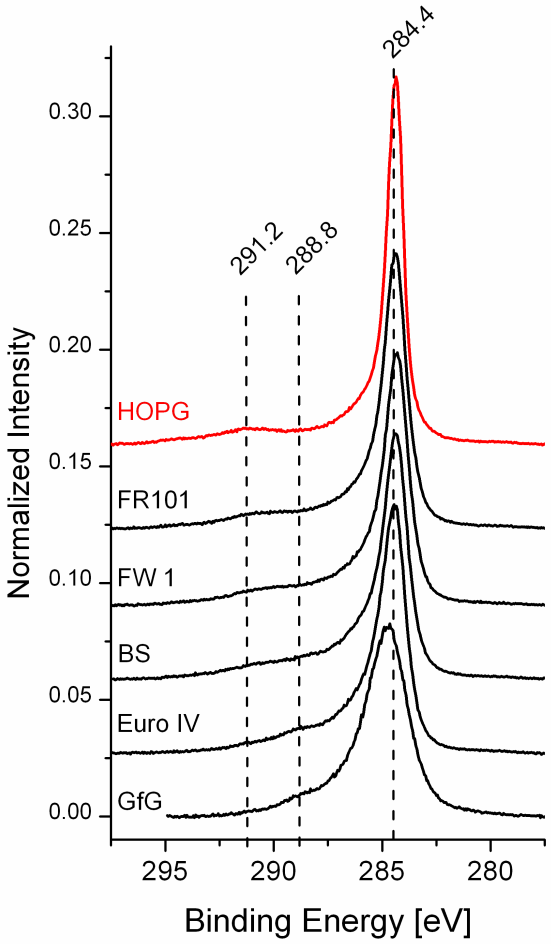

Fig. 5.2: XPS C1s spectra from the carbonaceous materials: GfG soot (GfG), the diesel engine soots (Euro IV and BS), the carbon blacks (FW 1 and FR 101) and the Graphite (HOPG). The spectra are offset for clarity.

In the C1s spectra of the carbon materials one can clearly observe the difference in the shape of the C1s (Fig. 5.2) at the binding energy (E_B) of 284.4 eV. The FWHM decreases as the graphitisation increases. The more graphitic the sample is according to the EELS measurements (Fig. 4.14) the more narrow the C1s intensity is. Additionally one observes the shake up satellite at an energy of 291.2 eV which also grows more intense with increasing graphitization [92]. The shoulder at 288.8 eV is assigned to oxygen functional groups [93–95].

To further analyse the contributions from oxygen functionalities and induced dis-

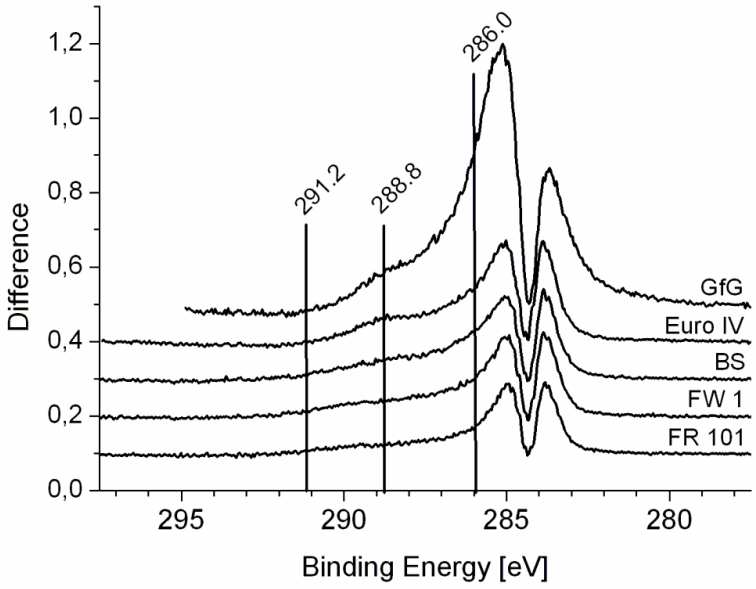

Fig. 5.3: Calculated difference of carbon black C1s and HOPG C1s spectra. Offset for clarity. The difference on the high energy side of the C1s peak indicate the density of defects as well as the different amount of oxygen functional groups.

order the C1s spectrum, difference spectra (after a normalization to 284,4 eV) are calculated of spectra from soot and carbon black and HOPG. In Fig. 5.3 the results are given. The low energetic part ($E_B < 284.4$ eV) of the difference displays predominantly the disorder in the materials compared to graphite. The higher binding energy side ($E_B > 286.5$ eV) shows clearly a contribution from oxygen functionalities. The broad peak at 287–289 eV is growing more intense the higher the amount of oxygen in the material is. In the GfG soot the additional intensity around 286 eV is assigned to C–H groups or to "sp^3" type defects [96, 97].

The O1s intensity is proportional to the amount of surface oxygen groups (Fig. 5.4). The GfG soot is the most functionalized of all, the FR 101 Lamp Black has the lowest amount, while no intensity is recorded on the non–functionalized HOPG. The focal points of the respective spectra changes, especially when comparing the carbon black samples with the diesel engine soot samples. Due to the high amount of different oxygen functional groups a data fitting with Gauss–Lorentz Curves is not performed. However, it is possible to assign predominant contributions from higher binding energies. The major components in the O1s spectra arise from contributions of the following carbon-oxygen functional groups: C=O at 530.1 eV, C–O–C at 531.8 eV, C–OH at 533.4 eV, additional intensity at 534.2 eV can also be attributed to chemisorbed water [98–101]. The contribution from 536.4 eV is as-

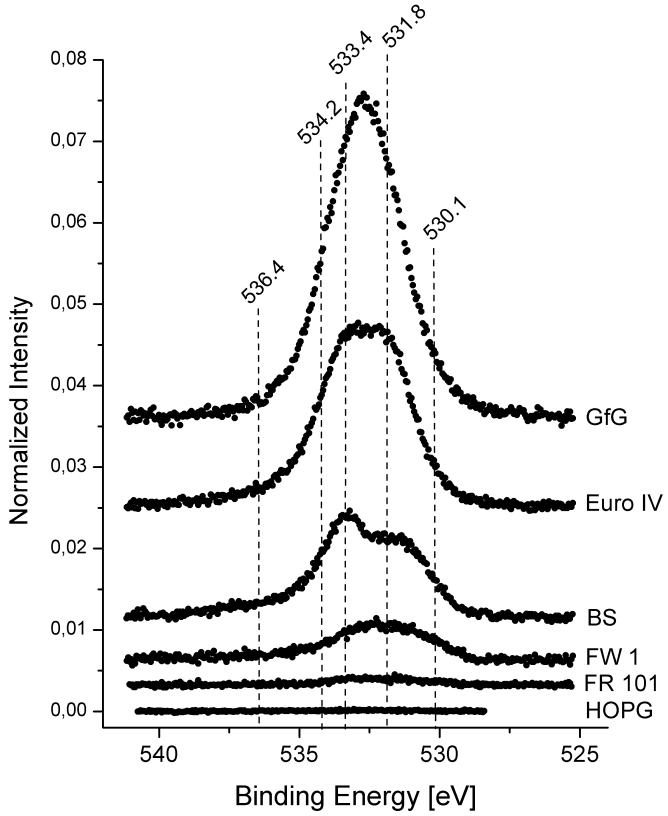

Fig. 5.4: XPS O1s spectra from the carbonaceous materials: GfG soot (GfG), the diesel engine soots (Euro IV and BS), the carbon blacks (FW 1 and FR 101) and the Graphite (HOPG). The spectra are offset for clarity.

signed to a differentially charged part. The weight of the O1s spectra in the case of the two industrial carbon blacks (FW 1, FR 101) is at 531.8 eV. Apparently the main contributions arise here from C=O and C–O–C configurations. The O1s spectra of the two diesel engine soots (BS, Euro IV) show a tendency to higher binding energies, the weight is at 532.8 eV. The majority of functional groups appear to share a C–OH configuration. The GfG soot shows the highest amount of oxygen groups equally shifted to higher binding energies. Apparently the diesel engine soot samples and the GfG soot are hydrophilic as can be seen from the higher amount of water detected with the O1s spectra. The very broad distribution indicates a wide multifariousness of carbon–oxygen–hydrogen complexes. The broad base indicates a certain amount of differential charging. From the areas of the intensities the surface composition of the carbon samples are calculated. The results are given in Table 5.1.

Table 5.1: Quantification of surface oxygen.

Sample	GfG soot	Euro IV soot	BS Soot	FW 1	FR 101	HOPG
C1s	83.1	88.0	82.6	97.0	99.5	99.8
O1s	16.9	12.0	7.4	3.0	0.5	0.2

5.3 Discussion

The XPS measurements display a similar bonding behavior. It is established that a predominant ordered sp^2 material as the HOPG will lead to a high intensity at binding energies of 284.4 eV as well as to an intense shake up satellite at 292.2 eV. The less developed these features are the less predominant sp2 hybridised carbon atoms are present. This influence of the disorder is also depicted in the FWHM of the C1s intensity for C–C carbon at a binding energy of 284.4 eV. The values decrease from 2.3 eV in the GfG soot to 0.9 eV for the HOPG. The C1s line at 284.4 eV also shows part of apparent sp^3 hybridisation due to defects or curvature strain in the material leading to an assymmetric line to higher binding energies [92,96,97, 102,103].

The C1s core–level spectra can be decomposed into two components. Because the C1s line in graphite occurs at lower binding energy than in diamond, it is possible to attribute the component at lower binding energy to sp^2 hybridization, and that at higher binding energy to sp^3 hybridization. As a matter of fact, carbonaceous materials, when conductive, give rise to a peculiar lineshape, asymmetrically broadened, that is to say its intensity decreases very slowly on the high binding energy side. Unfortunately this broadening appears on the same side as usual chemically shifted peaks [104]. Besides an inter–band $\Pi - \Pi^*$ peak about 6 eV high energy shifted (FWHM =4–5 eV called "plasmon"), pure graphite gives rise, in the region E_B = 280–300 eV, to a unique narrow carbon C1s peak which presents a very peculiar asymmetric shape, i.e., a broadening on its high energy side. Such a photospectroscopy lineshape is known to result from neutralization by conduction electrons of the holes created during photoionization. This phenomenon occurring in all the conductive materials has been well described in the literature using the Doniach–Sunjic model [104].

The line asymmetry depends on the band structure and is usually more pronounced when the Fermi level density of states (DOS) is high. Graphite, semi–metal with a very low Fermi level DOS, would normally induce a low asymmetry factor. However, electron—hole pairs are easily created in this specific material and induce a noticeable asymmetry of the C1s line. The C1s spectra have two contributions. The

first one, narrow (FWHM < 1 eV) and assymetric, arises from aromatic layers in graphitic sp^2 configurations (E_B = 284.6 eV). The second one is broader (FWHM ≥ 1.5 eV) and shifted by less than +1 eV from the preceding one, arises from regions of defective structure, presenting a more or less pronounced sp^3 character (see for example the difference spectra of GfG soot in Fig. 5.3). A third peak related to the $\Pi - \Pi^*$ levels transition, 4.5—5 eV broad and shifted by about + 5—6 eV, appears. Those three peaks are almost always present in carbonaceous materials. Their relative intensities depend on the degree of disorder of the studied material [95, 105, 106]. This is also evidenced by the fact that this feature is more intense in soot samples with a higher degree of graphitization, as the Lamp Black, the Furnace Soot and the BS soot. The total spectrum is usually completely fitted by adding to these fundamental components, the peaks related to carbon atoms bound to foreign elements like oxygen. In this context the high asymmetry in the C1s peak is strongly correlated to disorder in the soot and carbon black. As reflected in the TEM and EELS measurements, the GfG soot and the Euro IV soot differ significantly from the graphite structure. Especially in these cases, the C1s spectra show a high asymmetry toward higher BE. In the case of the other more graphitic soot and carbon blacks, the asymmetry is not that pronounced. The carbon has a higher sp^2 hybridization (EELS experiment) is therefore more graphitic and thus exhibiting a spectrum more similar to the HOPG C1s spectrum.

In the O1s intensity displays the predominant oxygen functional groups on the surface of the soot. By performing an Gauss-Lorentz fit to the spectrum we find, that the main contributions to the O1s spectrum are from C=O, C–O–C, and C–OH groups. However, the O1s spectra exhibit a high multifariousness, showing that a high variety of carbon–oxygen–hydrogen complexes exist. The main contributions to the spectra are different. The measurements of the industrial carbon blacks indicate a higher amount of C–O–C as well as C=O contributions. The diesel engine soots show a major contribution from C–OH groups, indicating their different origin. Generally, the groups are more prominent the more defects in the graphene structure is found. It is apparent, that the fullerenoid part of the carbon materials incorporates more heteroatoms as O, H, the graphitic spherical particles. DRIFTS measurements point towards aromatic ester groups. Transferred to the soot this can be interpreted as an ester group attached to the graphenes [107]. The carbon black with its graphitic structure develops less oxygen functional groups, whereas the very defective GfG soot shows the highest amount of oxygen functionalities (Fig. 5.5).

Evaluation of soot by spectroscopic methods as DRIFTS leads to additional conclusions regarding the structure of soot and related materials. The DRIFTS measure-

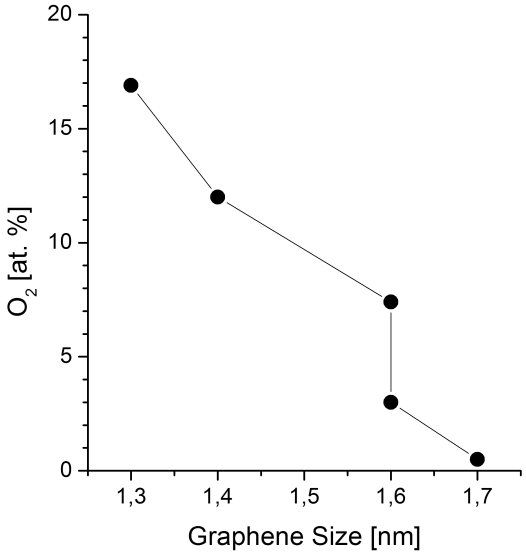

Fig. 5.5: Correlation of graphene size and O_2 content. The larger the graphenes, the lower the O_2 content.

ments correlate well with the XPS experiments. In the case of the GfG soot a high amount of heteroatoms is incorporated in the carbon material. Furthermore the C–H vibrations related to defective sp^3–type sites enforce the explanation of the respective line shape of the XPS measurements. The IR spectra show a high amount of C–OH vibrations in the case of the two diesel engine soots being the Euro IV soot and the BS soot.

Integration of all data seen in the surface investigation methods and additionally revealed with TEM and HRTEM lead to a picture of typical BSU as represented in Fig. 5.6. This is the typical graphitic structure. The layers are then held together by undefined carbon structures which are more reactive than the aromatic systems themselves [101].

The two most important elements in carbon chemistry are hydrogen and oxygen. Each element can undergo a wide range of chemically different coordinations which are often described as "surface complex". The local connectivity of surface atoms can be discriminated into sp^3, alkenic sp^2 and aromatic sp^2 for all kinds of carbon materials. Each of the three connectivities can form several type of heterobonds allowing for a broad distribution of carbon heteroatom interactions which coexist on any surface exhibiting structural defects.

The surface chemistry of prismatic and basal planes of sp^3 carbons is fundamentally different, which renders the surface area ration between the two orientations

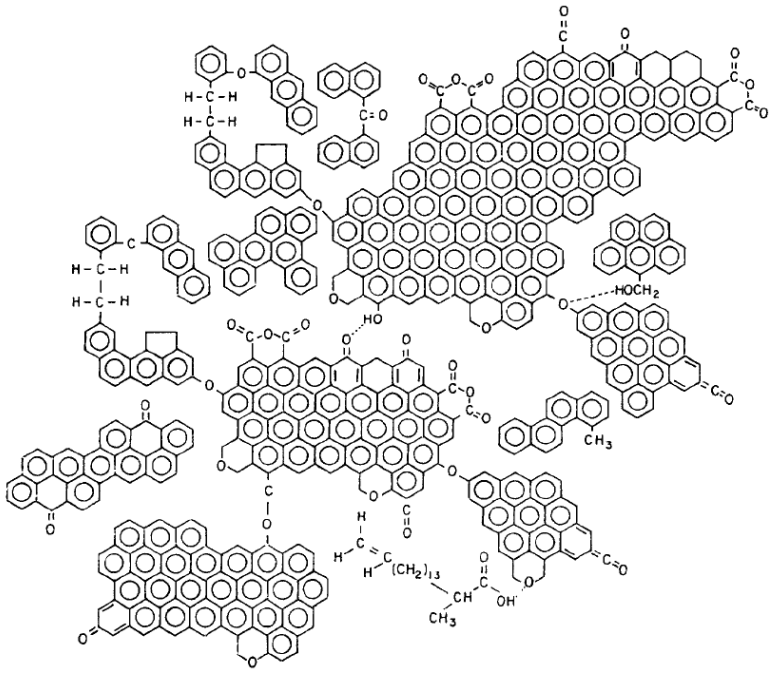

Fig. 5.6: Functionalised graphenes. The image shows different oxygen functional groups at the edges of the graphenes. The size of the graphenes varies. Smaller graphenes will exhibit a high amount of dangling bonds at the edge sites leading to a higher amount of functional groups. Adapted from [108].

one of the dominating factors for the description of carbon reactivity. This is well displayed in the TEM investigations in addition with graphene size distribution and the results from TG/TPO measurements. A significant fraction of the total carbon surface (prism faces and defect sites) is covered by heteroatoms and many of these are not just passivated by C–H bonds. However a low C:H ratio indicate small average diameters of the graphene layers or BSU. For carbons with a larger BSU diameters the dominance of prism sites is gradually reduced and defect sites become important locations for surface functional groups.

Nanocarbons from fullerenoid structure should exhibit a higher reactivity than the more graphitic soot (BS soot, Furnace soot, Lamp Black) as the presence of non 6 membered carbon rings with their olefinic electronic structure and the excessive presence of chemically reactive prism edges tend to destabilize such carbon structures. In addition, theoretical investigation predicts the influence of geometrical changes in chemical property (increasing reactivity upon increasing curvature) of nanocarbons. It is possible to conclude from the predominant graphene structures visualized from HRTEM the amount of heteroatoms as hydrogen or oxygen.

Chapter 6

Oxidation Experiments

In the following the link between microstructure, surface and reactivity is dealt with. The first two sections 6.1 and 6.2 show the different reactivities of the investigated materials, soot, carbon black and carbon model substances. In section 6.3 the gap to the real exhaust gases is closed by demonstrating the oxidation behavior of the relevant carbons as the GfG soot, the Euro IV diesel engine soot and the BS soot in NO_2. At the end (section 6.4) the reactivity issue is discussed with reference to the preceeding investigations of bulk and surface properties.

6.1 Thermogravimetric Measurements on Soot

6.1.1 TG–MS Investigations

To analyze the influence of structure on the oxidative behavior of the materials, a comparison between the GfG Soot, the Euro IV soot, the BS soot and the Furnace Soot is demonstrated. The TG/DSC data is acquired using the Netzsch–STA 449 instrument with Al_2O_3 crucibles. The samples are evacuated and the sample chamber is re–filled with 5% O_2 in N_2 which is maintained at a total flow rate of 100 ml/min. A heating rate of 5 K/min is used. The gas phase products are transferred through a heated quartz capillary to a quadrupol mass spectrometer operated in SIM mode (Thermostar, Balzers). The only products observed are CO_2 (m/e = 44–46) and H_2O (m/e = 17–18). The MS signals for m/e = 18 and m/e = 44 are representative of H_2O and CO_2, respectively. The ion currents for these masses are divided by the ion current for m/e = 28 to compensate for changes in sensitivity of the MS instrument. A background was substracted and the ratio was normalized to the mass of soot. The sample charge used for TG analysis was about 1 mg. The TG/TPO experiments display the different reactivities of the investigated carbon

samples. In Fig. 6.1a the results of the TPO experiments are plotted.

The onset temperature of combustion of the GfG Soot is about 200 °C. The soot loses mass, until at 640 °C it is completely oxidized. The Euro IV Soot shows the beginning of a weight loss at 380 °C and the oxidation of carbon is finished at 630 °C. No further oxidation is observed at temperatures above 630 °C The 10% of the sample remaining at 800 °C is ash from engine lubricating oil. The BS Soot is less prone to oxidation. It begins to lose mass at 500 °C and the highest rate of oxidation is reached at 660 °C. The combustion is completed at 690 °C. The Furnace Soot shows the lowest reactivity towards oxigen. The onset temperature of combustion is 550 °C. The soot is burnt out at 690 °C. Fig. 6.1b shows the DTG plot of the TG/TPO runs on the four selected soot and carbon black materials. For all four samples the mass remains nearly constant to temperatures up to 200 °C. From this temperature the DTG curves differ. The calculated curve for the GfG soot indicates a slow mass loss rate until a maximum in mass loss is reached at 520 °C, then the rate of mass loss decreases again until its complete oxidation at 640 °C. In the case of the Euro IV soot, the mass loss begins at 380 °C. A maximum in combustion rate is reached at 600 °C. The DTG curves for the BS soot and the FW 1 soot are similar, reflecting their common microstructure. Apparently the BS soot starts with mass loss at 450 °C, the maximum in oxidation is at 660 °C. For the FW 1 soot the oxidation begins at higher temperatures: 480 °C, the soot seems to reach the maximum in oxidation rate at slightly lower temperatures (650 °C) than the BS soot.

Fig. 6.2 shows the evolution of CO_2 (Fig. 6.2 a) and H_2O (Fig. 6.2 b) obtained from analysis of the mass spectra. The GfG Soot begins to evolve CO_2 at 250 °C. The CO_2 evolution shows two maxima, at 340 °C and 520 °C, respectively. The maximum rate in weight loss occurs at 520 °C. The H_2O is detected in the effluent stream over the same temperature range as CO_2, the maximum in H_2O evolution is at 340 °C coinciding with the first maximum in the CO_2 signal. A second local maximum in the H_2O signal is revealed at 520 °C. From the MS–Data three regions can be identified: The first temperature range from 200–400 °C where a relative high H_2O signal is dominant. The second region from 400–650 °C exhibits a lower m/e = 18 signal whereas the m/e = 44 signal is having a global maximum. In the range >650 °C both MS signals are decreasing. The MS signal of the Euro IV Soot indicates a slight evolution of CO_2 started at above 380 °C. The MS signal of CO_2 rises rapidly and reaches a maximum at 590 °C corresponding to the maximum of rate mass loss in the sample. The signal drops sharply after that due to the total burn out of carbon. The MS spectra of the Euro IV Soot begins to show a H_2O signal at 250 °C and shows a shoulder at 300 °C. The maximum in H_2O evolution (590 °C) corresponds to the maximum in CO_2 evolution. The gas phase analysis

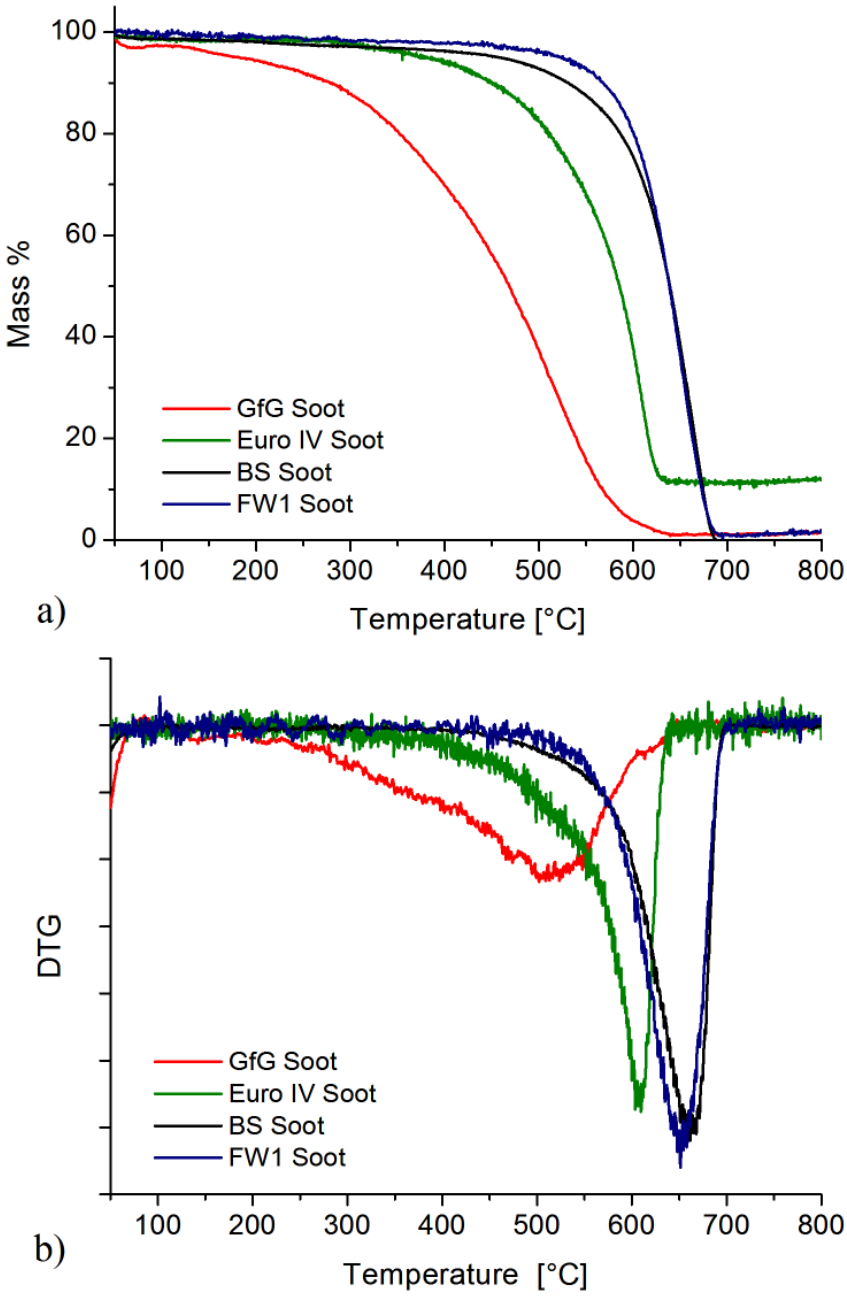

Fig. 6.1: a) TG/TPO measurements on the soot and carbon black samples, b) derived DTG results. The results show differences in the onset of mass loss and the total burnout temperature for the measured soot and carbon black samples.

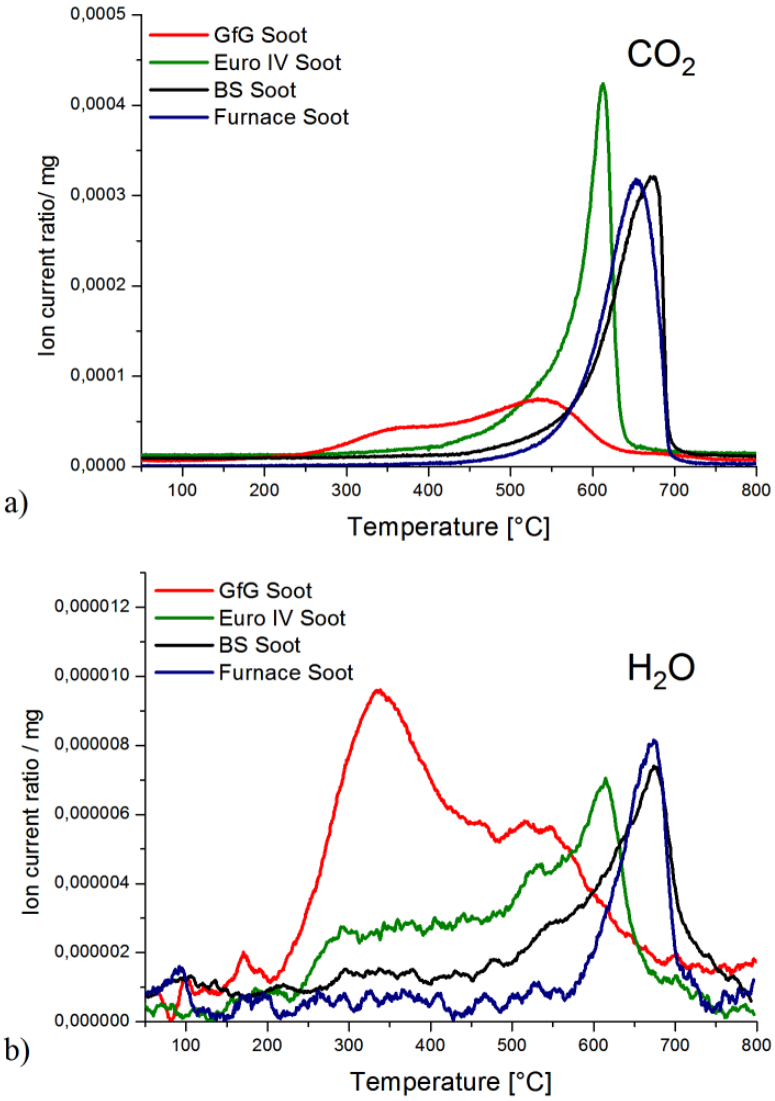

Fig. 6.2: Mass spectra analysis of the products of combustion, a) CO_2 (m/e = 44) and b) H_2O (m/e = 18).

during the combustion of the BS Soot shows that CO_2 begins to evolve at 550 °C and goes through a maximum at 680 °C. This also corresponds to the maximum in mass loss. A corresponding signal for the evolution of H_2O from the BS Soot is first detected at 400 °C with a maximum at 680 °C. The Furnace Soot begins to show a CO_2 evolution also at 450 °C which passes through a maximum at 650 °C. An increase in the H_2O signal occurs at 550 °C, it also has a maximum at 670 °C corresponding to the maximum in the CO_2 signal. The gas phase analysis of the CO_2 evolution of the BS Soot and the Furnace Soot is similar, while the H_2O evolution is different.

In order to further differentiate the samples isothermal experiments were conducted at 380 °C, the onset temperature of combustion of the Euro IV soot (Fig. 6.3).

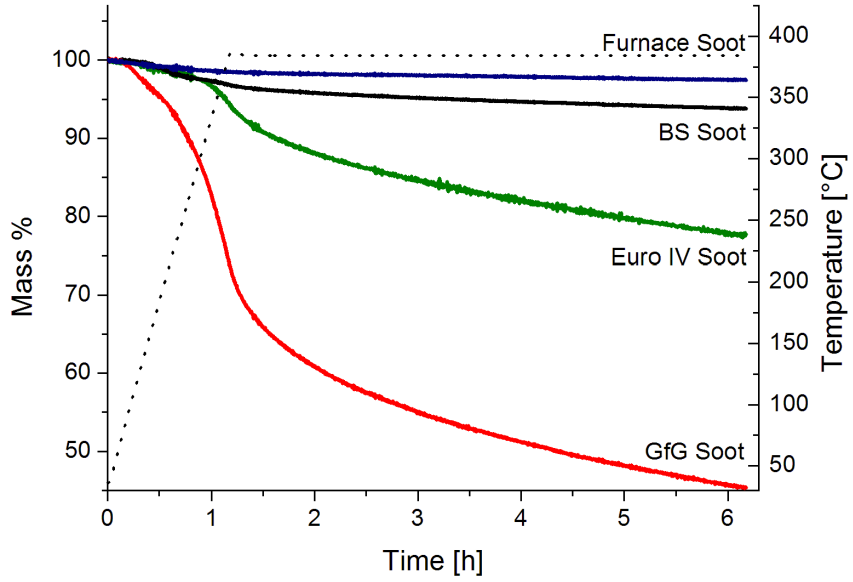

Fig. 6.3: Isothermal experiments: 6 h of oxidation of GfG Soot, Euro IV Soot, BS Soot and Furnace Soot in 5% O_2 in N_2.

Fig. 6.3 shows the mass as a function of time for the GfG Soot, the Euro IV Soot, the BS Soot and the Furnace Soot while the samples are kept at 380 °C for 5 hours in 5% O_2. The GfG Soot loses already 30% of its mass while heating up to 380 °C. The Euro IV and the BS Soot samples lose 3% of their mass during heating to 320 °C. Between 320 °C and 380 °C and for the first 2 hours thereafter the Euro IV Soot loses weight much more rapidly than the BS Soot. The easiest oxidizable fraction of soot constitutes 8% of the Euro IV Soot. The Furnace Soot loses during the whole experiment only a small fraction of mass: approximately 3%. After about 4 hours

at 380 °C all the samples continue to lose weight at constant rates, respectively, i.e. the GfG Soot at 5 wt%/h the Euro IV Soot at 2 wt%/h, the BS Soot at 0.4 wt%/h and the Furnace Soot at 0.1 wt%/h.

6.1.2 Combustion in Steps

The previous TG experiments indicate a structure–reactivity correlation. The MS data indicates changes in the predominant reaction mechanism. In the following section the changes in morphology during oxidation of the soots are investigated with TEM and HRTEM. The GfG soot and the Euro IV soot are chosen for a comparative analysis. The soot oxidation is performed in steps [109]. The respective remnant materials are then prepared for TEM investigation.

GfG soot

The experiment for the GfG spark discharge soot is depicted in Fig. 6.4. The sample is heated in the TG in 5% O_2 in N_2 to 275 °C, 450 °C, and 575 °C, respectively.

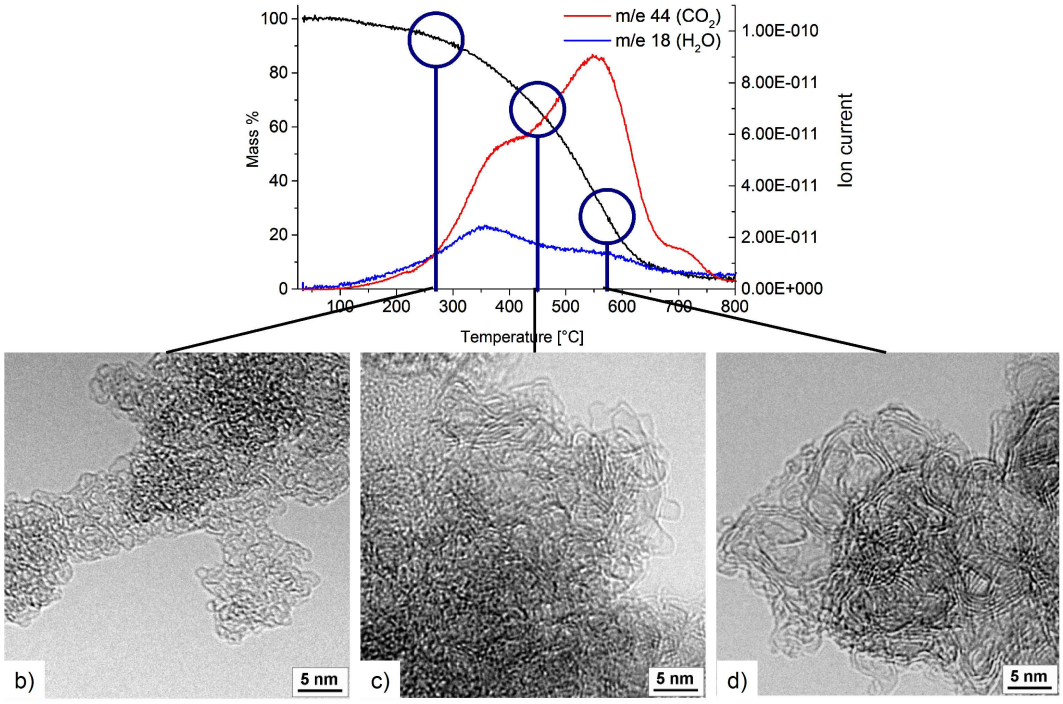

Fig. 6.4: Oxidation in steps: GfG soot, a) shows when the oxidation is interrupted to investigate the morphology, b) morphology of the GfG soot after heating to 275 °C, c) to 450 °C, d) to 575 °C

At the respective temperatures the oxidation is interrupted in cutting off the oxygen

flow. Thus, the samples can be cooled down in inert atmosphere. This prevents the samples from changing or further oxidizing during cooling down in the TG oven. Representative HRTEM images from the sample are given in Fig. 6.4b, c, d.

The predominant morphology of the investigated sample reveals differences. After the first step in oxidation the very easy combustible part of the soot is gone. This leads to a general morphology showing more flat ribbons with greater ribbon length. This is even more clearly seen in the sample which has been exposed to a temperature up to 450 °C. The HRTEM micrograph reveals larger graphene layers. This more resistant material appears to be more graphitic. A "stacking" of the graphene layers can be seen. It is also possible that a healing of defects occurs leading to a graphitization of the carbon. After a temperature of 575 °C, polyhedral onions are left in the sample. This appears to be the most stable form of carbon in the GfG soot under these oxidative conditions. The larger graphenes observed in Fig. 6.4d, although irregularly stacked are less prone to oxidation than the small strong bent graphenes observed in Fig. 6.4b.

Euro IV soot

The experiment for the Euro IV HD diesel engine soot is depicted in Fig. 6.5. The soot is heated in the TG in 5% O_2 in N_2 to temperatures of 425 °C, 550 °C, 625 °C, respectively.

At the respective temperatures the oxidation is interrupted in cutting of the oxygen flow. Thus the samples could be cooled down in inert atmosphere. This prevents the samples to change or further oxidize during cooling down in the TG oven. Representative HRTEM images from the sample are given in Fig. 6.5b, c, d. The differences in the morphology of the sample are not as strong as described in the case of the GfG soot (Fig. 6.4). The first image from 425 °C shows the morphology of the Euro IV HD diesel engine soot which is similar to that of the fresh soot. One observes in the HRTEM image the fullerenoid character of the soot. At higher temperatures the very fullerenoid part of the soot is oxidized. Soot particles are now predominant which are enclosed by a graphitic shell. This graphitic shell envelops several nuclei that are typical of the Euro IV soot. However this appears not to be the most stable material. The particles depicted in Figure 6.5 d are spherical with very few surface irregularities. The fullerenoid chainlike agglomerates are not present anymore in the sample. They are oxidized, leaving behind the graphitic spherical soot particles that are not predominant in the Euro IV soot but nevertheless present in the original sample.

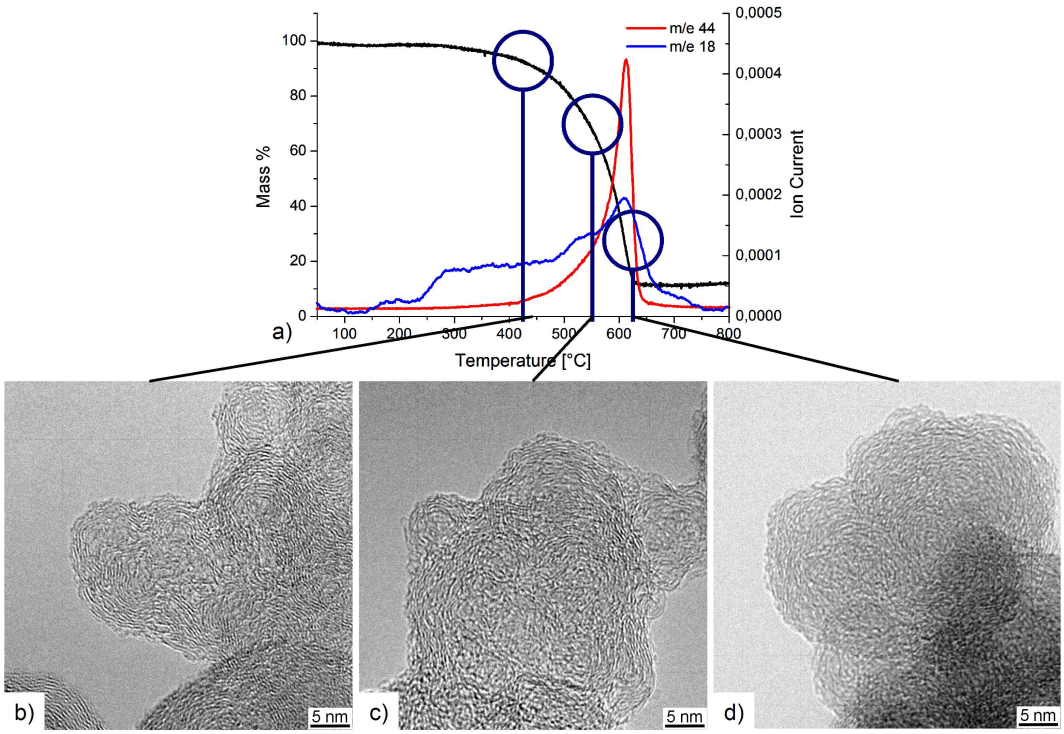

Fig. 6.5: Oxidation in steps: Euro IV soot, a) shows when the oxidation is interrupted to investigate the morphology, b) morphology of the Euro IV after heating to 425 °C, c) to 550 °C, d) to 625 °C.

6.1.3 Solid State Kinetics

The concepts of solid state kinetics [110] came into being from a wealth of isothermal experiments well before the first instruments for non–isothermal measurements became commercially available. Solid state reactions are usually taken to comprise the decomposition of solids [111], the reactions of two or more solids with each other and the reaction of a solid with a gaseous or liquid interface. One characteristic feature of solid state reactions is the total destruction of the reactant solid phases. These processes are thus sharply distinguished from reactions in gaseous or liquid solution, in which the fluid reacting phase exists continuously throughout the reaction, with a continuous variation in the activities of the components. In solid state reactions, the reaction zone often consists of growing ”nuclei” of the products. The number of nuclei and the surface area of each nucleus both increase with time and either of these dependences may determine the overall rate law. There is no single type of elementary process which can be thought of as generally dominant in solid state reaction mechanisms. Rate of reactions may be limited by the transport of matter, heat or mechanical stress (propellant burning or detonation). A reaction interface may be a surface of large extent, readily observable, and

sometimes, as in the burning of a solid propellant, of a shape, which is initially under the experimenter's control – which enhances the opportunity to preselect the kinetic rate law [112,113].

To further investigate the mechanism of soot oxidation and as a start for a model–based kinetic analysis, a model free analysis is performed. Later a model for soot oxidation, describing the influence of the predominant morphologies in the soot samples (fullerenoid part vs. spherical particles) will be presented. In kinetic analysis [113,114]it is generally assumed that the rate of reaction can be described by two separable functions $K(T)$ and $f(\alpha)$ such that:

$$\frac{\mathrm{d}\alpha}{\mathrm{d}t} = K(T) \cdot f(\alpha) \tag{6.1}$$

where $\mathrm{d}\alpha/\mathrm{d}t$ is the rate of reaction, α the conversion, $K(T)$ is the temperature dependent rate constant, and $f(\alpha)$ corresponds to the reaction model. The temperature dependence of the rate constant is commonly described by the Arrhenius equation

$$K(T) = A \cdot \exp\left(\frac{-E_A}{RT}\right) \tag{6.2}$$

where R is the universal gas constant, E_A is the activation energy and A is the preexponantial factor. For experiments in which samples are heated at a constant rate, the explicit time dependence can be eliminated so that

$$\frac{\mathrm{d}\alpha}{\mathrm{d}T} = \frac{1}{\beta}\frac{\mathrm{d}\alpha}{\mathrm{d}t} \tag{6.3}$$

In the case of a constant heating rate, $\beta = \mathrm{d}T/\mathrm{d}t$ Eq. 6.1 becomes

$$\frac{\mathrm{d}\alpha}{\mathrm{d}T} = \frac{A}{\beta} \cdot \left(\frac{-E_A}{RT}\right) \cdot f(\alpha) \tag{6.4}$$

The "model-free" isoconversional method assumes that both the activation energy and the pre–exponential factor are functions of the degree of conversion α. In this case conversion is the amount of mass loss during oxidation. The activation energy is determined by Friedman's method [115] from the logarithmic form of the rate equation for each heating rate:

$$\ln\left[\beta_i \left(\mathrm{d}\alpha/\mathrm{d}T\right)_{\alpha,i}\right] = \ln\left(A_\alpha f\left(\alpha\right)\right) - \frac{E_\alpha}{RT_{\alpha,i}} \tag{6.5}$$

where the subscript α is the value at a particular degree of conversion and i refers

to data from a given heating rate experiment. The activation energy at each degree of conversion is calculated using linear regression from a plot of $\ln\left[\beta_i \left(\mathrm{d}\alpha/\mathrm{d}T\right)_{\alpha,i}\right]$ versus $1/T_{\alpha,i}$ (Friedman plot) across all of the heating rates tested. Similarly, the product of conversion dependent pre–exponential factor and the reaction model can be obtained from the y–intercept of the Friedman plot.

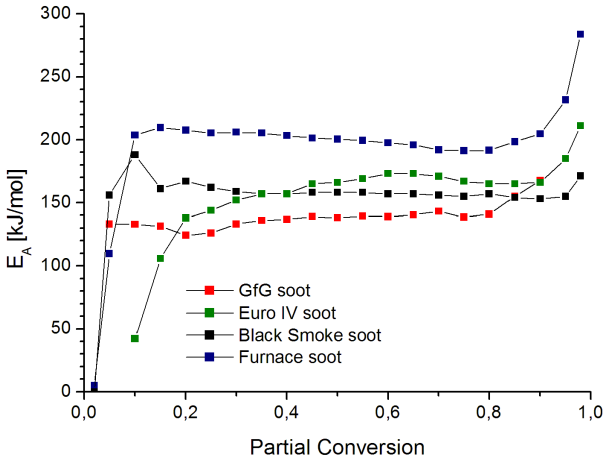

Fig. 6.6: Estimated apparent activation energies derived with the isoconversional approach after Friedman.

The isoconversional approach can be used to evaluate both simple and complex chemical reactions. For evaluation of data using this method no kinetic rate expression is assumed a priori. It is possible to estimate different apparent activation energies to the different soot samples. For this purpose the samples are heated in the same atmosphere with different heating rates (1.5, 3 and 5 K/min). With the model free analysis suggested by Friedman [115], implemented in the NETZSCH Thermokinetics Diffusion Control software version 2000.9b, the apparent activation energies can be estimated (Fig. 6.6). The isoconversional approach can be used to evaluate both simple and complex chemical reactions. For evaluation of data using this method no kinetic rate expression is assumed a priori. Furthermore it is assumed that no change in reaction mechanism occurs during the experiment. Table 6.1 gives the results of the average apparent activation energy (E_A).

The established formalism of isothermal kinetics has been extended to non–isothermal conditions. Equation 6.1 describes the dependence of the reaction rate on the extent of reaction. In soot, the molecular motion is restricted. The reactions are dependent on the local structure and reactivity. Unlike in a pure compound soot is a very heterogeneous material. It will burn probably with many parallel reaction paths. The reaction model $f(\alpha)$ plays a role of an empirical function.

Table 6.1: Average value of the apparent activation energies E_A estimated with model free analysis of three TPO experimens, at 1.5, 3 and 5 K/min, respectively.

Sample	Apparent Activation Energy [kJ/mol]
GfG Soot	130 ± 10
Euro IV Soot	150 ± 30
BS Soot	160 ± 40
Furnace Soot	210 ± 30

Equation (6.1) is often used in its integral form which for isothermal conditions becomes:

$$g(\alpha) \equiv \int_0^\alpha [f(\alpha)]^{-1} \, \mathrm{d}\alpha = K(T)t \tag{6.6}$$

For non–isothermal conditions, one can eliminate the explicit time dependence of the kinetic equations by use of the heating rate. In the case of a constant heating rate, $\beta = \mathrm{d}T/\mathrm{d}t$ Equation (6.6) takes the form:

$$g(\alpha) \equiv \int_0^\alpha [f(\alpha)]^{-1} \, \mathrm{d}\alpha = \frac{1}{\beta} \int_0^T K(T) \, \mathrm{d}T \tag{6.7}$$

For many reactions, the Arrhenius equation provides a good description of the temperature dependence of the rate constant. Substitution for $K(T)$ leads to

$$g(\alpha) = \frac{A}{\beta} \int_0^T \exp\left(\frac{-E_A}{RT}\right) \mathrm{d}T \tag{6.8}$$

where E_A and A are the Arrhenius parameters (activation energy and pre–exponential factor, respectively). Using this formalism, the global reaction kinetics are completely specified by three pieces of information: the reaction model and the two Arrhenius parameters.

The model free analysis gives a first insight into the apparent activation energies calculated for the soot oxidation. From the gas phase analysis it is evident that the soot oxidation is not a one step process, as during different stages of burnout the MS signals change. These steps involve different reaction paths predominant on the different soot morphologies. It is also observed, that different morphologies in the soot exhibit different oxidation profiles. First of all the soot is not a homogeneous material as revealed in the TEM investigations. The most striking difference is the occurrence of soot spheres (primary particles) versus the single graphenes

(GfG soot) or the small nuclei (in the Euro IV diesel engine soot). Thus, it cannot be expected that only a single reaction step occurs in order to oxidize the soot completely. The defective highly functionalized part has a different pathway of combustion than predominant spherical soot particles.

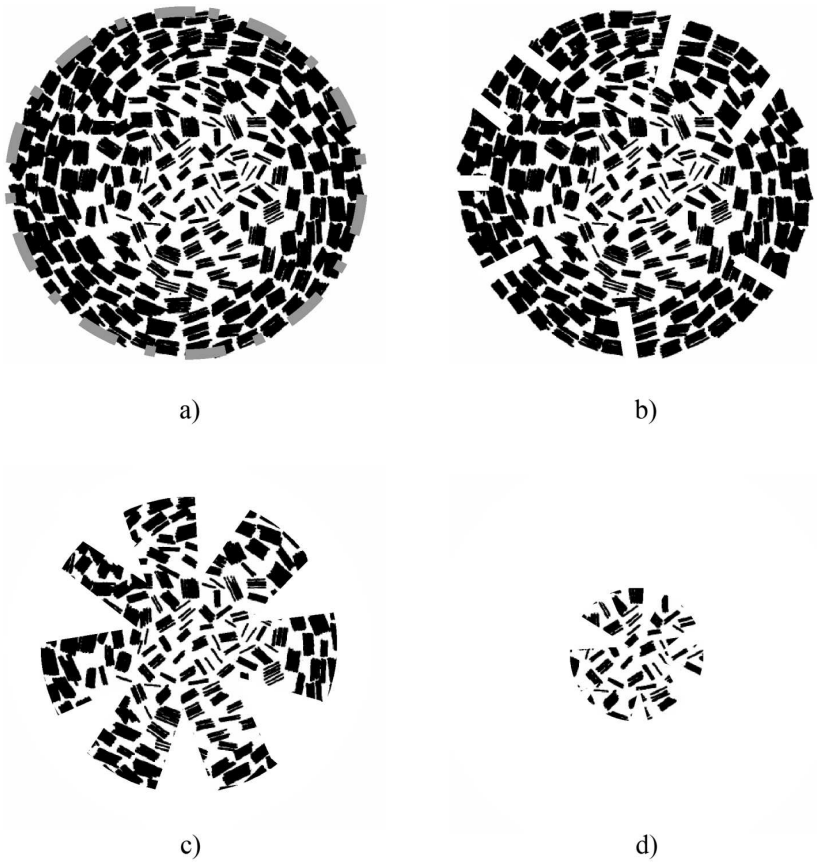

Fig. 6.7: Model of the oxidation of the soot spheres. a) the surface is oxidized removing volatile parts, b) the first pores are developing due to the anisotropical oxidation of the graphenes, c) the pores are widened, d) the spheres reduce in size until the soot is oxidized.

A model for the soot oxidation should include the following steps. First the very defective functionalized graphenes are oxidized. In a second step the smaller nuclei with the strong bent graphenes are oxidized. The transport limitation in this case is the diffusion to the graphene oxidation sites. The third process might then be the predominant oxidation of the large graphitic primary particles. This would indicate different reactions being independent from each other. A possible sketch of the soot sphere oxidation is depicted in Fig. 6.7.

Based on the fact that the graphite oxidation proceeds anisotropically, it is possible to outline the following soot oxidation mechanism. First, as already described for the defective functionalized graphenes and the smaller nuclei, the strong bent

graphenes are oxidized. This procedure is dominant in the very defective GfG Soot as to a great part in the Euro IV soot. In the very graphitic spheres the graphite crystallites have to be oxidized. Small pores are present in the soot [59]. The oxidant enters these pores and the oxidation takes place. This process leads to an enlargement of the micropores. Thus the surface increases, more surface is accessible to the oxidant. This leads to the combustion of the soot spheres in such a way that the overall projected diameter decreases [109] until the particles are oxidized.

These processes of oxidation of graphenes, of small nuclei and oxidizing the soot spheres are independent from each other. The oxidation will take place in the different structures at different temperatures. The apparent activation energy is higher for the graphitic spherical soot particles.

It is important to point out that no detailed analysis in the framework of solid state kinetics is attempted. The phenomenological models used in this work are chosen to fit the soot oxidation. The results are then used to predict the soot oxidation for isothermal experiments.

The three assigned models for the soot oxidation could be fitted with the following steps, known from solid state chemistry. The integral form of the models g(α) with $0 < \alpha < 100$, are given in Table 6.2.

Table 6.2: Set of chosen reaction models applied to describe the reaction kinetics for soot oxidation.

	Reaction Model	$g(\alpha)$
1	3-dim. Diffusion, Jander	$1 - \sqrt[3]{1 - \frac{100-\alpha}{100}}^{\,2}$
2	3-dim. Nucl. Growth, Avrami Erofeev	$-\ln \frac{100-\alpha}{100}^{\,1/2}$
3	3-dim. Phase Boundary Reaction, Contr. Sphere	$1 - \left(1 - \frac{100-\alpha}{100}\right)^{1/2}$

With the NETZSCH Software it is possible to fit the data according to the presented models. For the very Graphitic materials the contracting sphere model appears to be the dominating step in overall mass loss.

The routine model fitting was performed as follows. In the case of the GfG soot four independent reactions are assumed. The gas phase analysis supports this view (see Fig. 6.2). The parallel reactions are being assumed of a three dimensional diffusion (Jander [116]). The four steps contribute to the overall reaction in the following manner: step 1: 5%, step 2: 16%, step 3: 65%, step 4: 14%. These overall found parts in combustion correlate with the steps in the gas phase in such a way that step 2 and step 3 do contribute to the major amout in mass loss (maximum in gas phase evolution).

In the case of the Euro IV HD diesel engine soot, three major steps in gas phase evo-

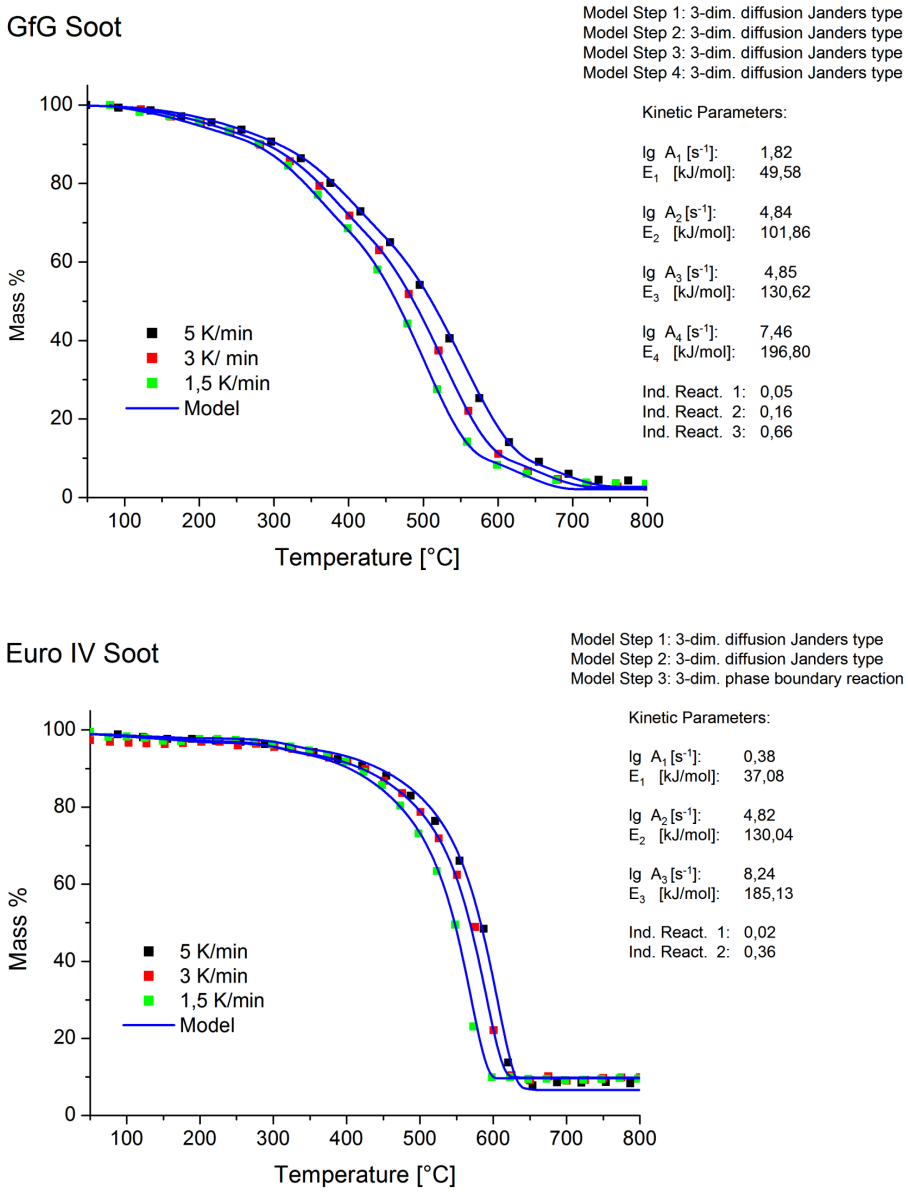

Fig. 6.8: Oxidation a) of the GfG soot, b) of the Euro IV HD diesel engine soot.

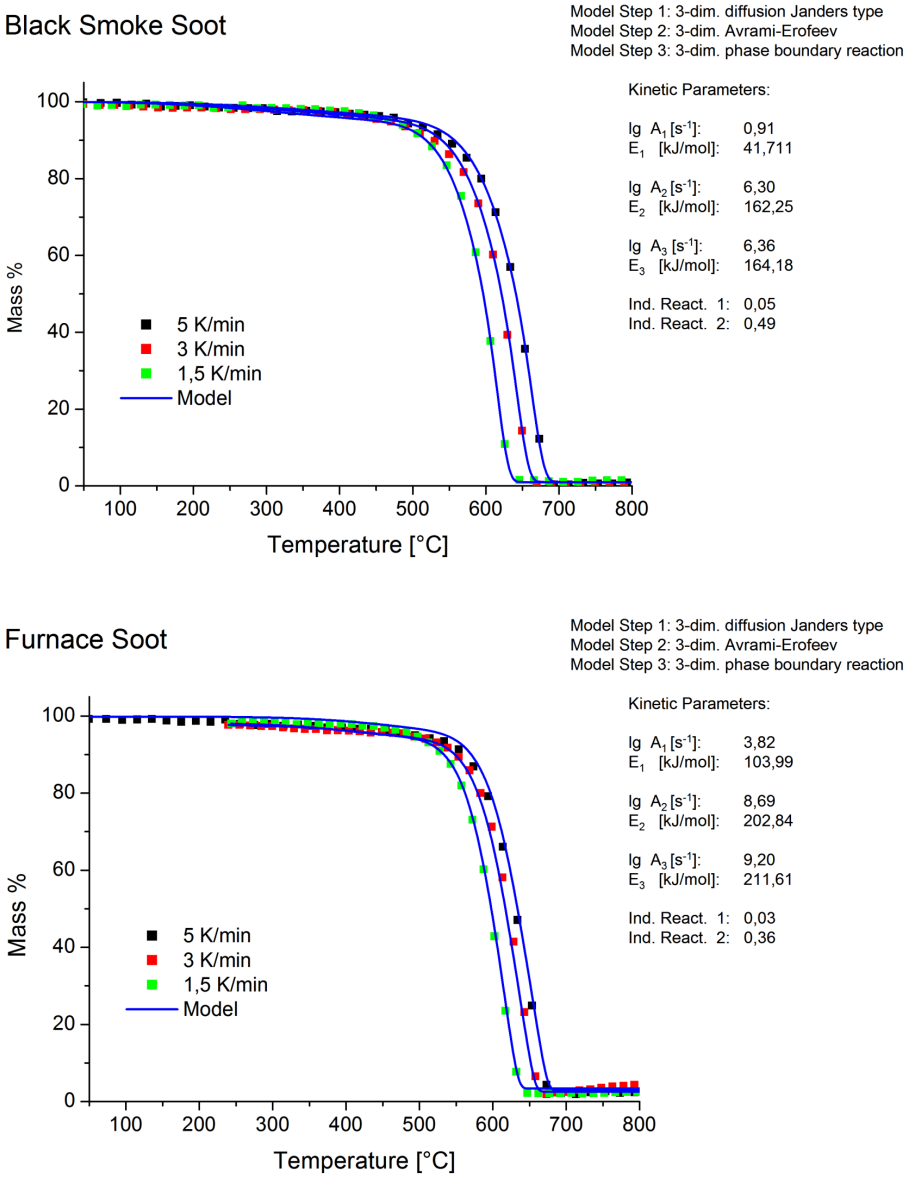

Fig. 6.9: Oxidation of a) the BS soot and b) the Furnace Soot.

lution can be deduced from the acquired MS data. Due to the different morphology and functionalisation, the predominant parts in kinetics require the modeling of the soot oxidation with the following models as three parallel reactions. Two steps are fitted using the 3 dim. Jander's diffusion, the last step with the 3 dim. phase boundary reaction model. The three steps contribute to the overall reaction in the following manner: step 1: 3%, step 2: 36%, step 3: 61%. These parallel pathways in combustion correlate with the steps in the gas phase in such a way that step 2 and step 3 do contribute to the major amout in mass loss (maximum in gas phase evolution).

The oxidation of the BS soot and the Furnace Soot takes place in quite similar ways. As already pointed out, the general morphology is similar and also the overall functionalization, as seen in the XPS and DRIFTS experiments. In this case, for both soots, three steps are assumed: step 1: 3 dim. Jander's type diffusion, step 2: 3 dim. Avrami–Erofeev, step 3: 3 dim. phase boundary reaction. The overall reaction in the case of the BS soot takes place as follows: step 1: 5%, step 2: 49% step 3: 46%. In the case of the Furnace soot, the Parts are divided as follows: step 1: 3%, step 2: 36%, step 3 51%.

The apparent activation energies are different in the respective steps of soot oxidation. However the steps exhibit similarities in the values for E_A. The first step with a mass loss of 3–5% gives an apparent activation energy of approximately 30–50 kJ/mol. This is a value typical for gas phase transport. The other steps describe with their apparent activation energies the parts of mass transport in the solids as well as converting C(solid) to CO_2. The found activation energies correlate well with the literature. For soot aerosols values from 50 to 100 kJ/mol are reported, in contrast to this for graphitic materials (carbon blacks) higher activation energies are calculated (100–400 kJ/mol) [9,117,118]

In order to validate these models and to relate the temperature ramp experiments to the real world filter, predictions are calculated for the mass loss at 380 °C. In Fig. 6.10, predictions obtained from the results of the model fitting of the independent reaction steps are plotted against the experimental results already shown in Fig. 6.3. The oxidation behavior of the GfG soot, the Euro IV soot, the BS soot and the Furnace Soot, while the samples are kept at 380 °C for 5 hours in 5% O_2 is plotted.

The GfG soot loses already 30% of its mass while heating up to 380 °C. The Euro IV and the BS soot samples lose 3% of their mass during heating to 320 °C. The Furnace Soot loses during the whole experiment only a small fracton of mass: approximately 3%. After about 4 hours at 380 °C all the samples continue to lose weight at constant rates, respectively, i.e. the GfG Soot at 5 wt%/h, the Euro IV

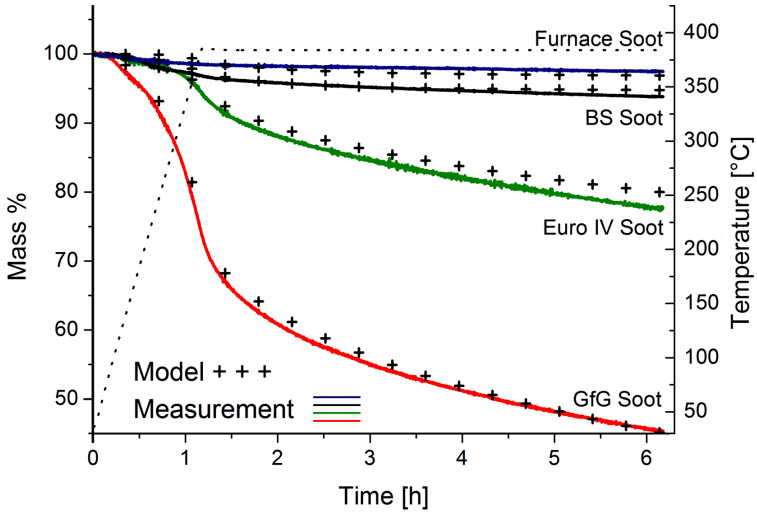

Fig. 6.10: Isothermal experiments carried out at 380 °C, the predictions from the applied models are plotted against the curves.

soot at 2 wt%/h, the BS soot at 0.4 wt%/h and the Furnace Soot at 0.1 wt%/h. The models describe the oxidation behavior of the investigated materials at isothermal conditions very well. This can be derived from Fig. 6.10. It is possible to model the mass loss over time for the whole experiment consisting of the heating step to 380 °C and the isothermal conditions for 5h. This bridges these experiments to the isothermal conditions in a particulate trap. Furthermore it should now be possible to make predictions for different temperatures of oxidation and different atmospheres. These results will be applied to soot oxidation experiments under more realistic conditions in section 6.3.

6.2 Thermogravimetric Measurements on the GPAH

A short description of the GPAH model systems is given in section 4.1.4. The TG/TPO experiments are conducted in order to clarify the influence of the microstructure on the reactivity. The respective samples are heated in 5% O_2 in N_2 from 25 °C to 800 °C. Fig. 6.11 displays the mass loss over temperature.

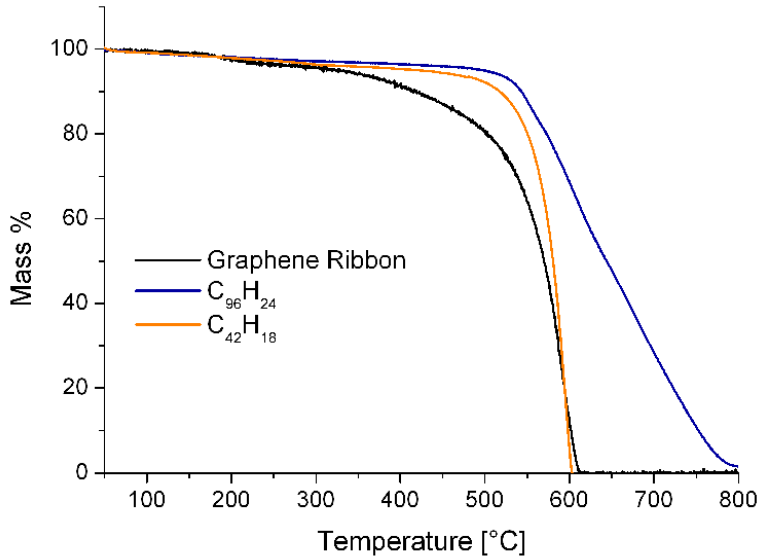

Fig. 6.11: Mass loss over temperature for the three chosen model substances.

The different reactivity of the samples is clearly visible. The Graphene Ribbon already shows a small mass loss at 200 °C. At slightly higher temperatures (350 °C) the weight loss increases and reaches a maximum at about 590 °C. A different and more defined combustion behavior is observed in the case of the $C_{42}H_{18}$. The mass remains nearly constant to a temperature of 500 °C. Then the sample rapidly loses mass (highest rate at 600 °C) until at 610 °C the combustion of the sample is completed. The least reactive sample is the $C_{96}H_{24}$. The mass of the sample remains constant until at 550 °C. The maximum in mass loss is found to be at 650 °C. The reaction is finished at 800 °C.

Fig. 6.12 shows the evolution of CO_2 (Fig. 6.12 a) and H_2O (Fig. 6.12 b) obtained from analysis of the mass spectra. The gas phase evolution follows the scheme of mass loss. In the case of the Graphene Ribbon, the CO_2 evolution starts at about 300 °C. The signal shows a small shoulder already at 440 °C, followed by a maximum in the CO_2 evolution at 590 °C. This corresponds to the maximum in mass loss as described above. The H_2O signal begins to rise at 200 °C, where the first

mass loss takes place. The signal shows a local maximum at 440 °C coinciding with the shoulder in he CO_2 signal. A second maximum can be measured (590 °C). The gas phase evolution of the $C_{42}H_{18}$ is considerably different. A CO_2 evolution begins at 480 °C and reaches a maximum at 600 °C related to the maximum in mass loss. The CO_2 signal drops to 0 at 610 °C. The H_2O evolution is similar. A slight intensification of the signal can be measured at 300 °C, showing a small plateau. The maximum of H_2O evolution coincides with the maximum in CO_2 evolution.

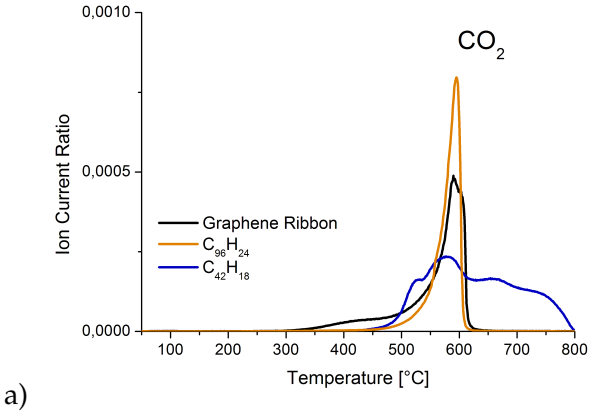

a)

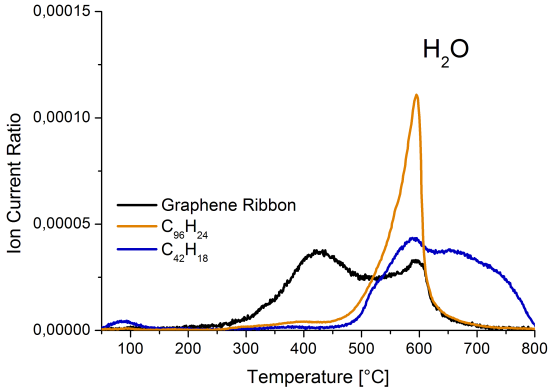

b)

Fig. 6.12: MS Data acquired during oxidation of the GPAH. a) CO_2 signal, b) H_2O signal.

The MS data of the $C_{96}H_{24}$ show a somehow interesting behavior. The CO_2 evolution starts at 450 °C. Several local maxima (525 °C, 580 °C, 660 °C, 740 °C) are observed during the oxidation of the material. As the carbon consumption is completed at 800 °C, the CO_2 signal drops to 0. The evolution of H_2O begins at the same temperature as in the case of he CO_2. Here too, the MS signal shows several features until the H_2O signal drops down. A clear maximum can be seen at 580 °C, coinciding with the second local maximum the mass signal for CO_2. The other features follow the gas phase evolution of CO_2, but only in exhibiting small shoulders.

Apparently the reactivity of the GPAH is dominated also by their microstructure already described in section 4.1.4. The very graphitic $C_{96}H_{24}$ is the most difficult to oxidise. In the case of the smaller Hexabenzocoronene $C_{42}H_{18}$, the oxidation is enhanced. From literature it is known that $C_{42}H_{18}$ sublimes at temperatures around 650 °C, so it cannot be excluded that this effect overlaps with the overall oxidation. From the point of view of structure reactivity correlation it is apparent, that the Graphene Ribbon resembles most to the natural soot. The bent, defect rich ribbons exhibit an olefinic structure with double bonds as derived from the EELS measurements (Fig. 4.13). The burnout temperature and the overall behavior as Mass = f(Time), resembles most to the soot substances. It may be an interesting enigm to continue the research on this material in introducing different oxygen functional groups and investigating the change in reactivity. A further discussion with relation to the investigated soot samples is continued in section 6.4.

6.3 Towards Realistic Exhaust Conditions

6.3.1 Experimental Considerations

As seen in section 6.1, the structurally different carbon black samples exhibit different reactivities in the oxidative atmosphere. This is due to the influence of morphology and nanostructure, sp^2/sp^3 hybridization ratio and functionalization (chapter 4 and 5). It is now evident that a meaningful investigation on the influence of the real gas atmosphere in a particulate trap can only be successful if the real diesel engine soot is used. Preliminary investigations also revealed that changes in the oxygen content from 5% to 10% does not influence the results of the TG experiments. Variing H_2O as well as NO content in the gas atmosphere did not show significant changes in the TPO experiments as well. The main focus is put on the influence of the NO_2 on the soot oxidation. For this purpose the influence of NO_2 will be tested on the GfG soot, the Euro IV HD diesel engine soot and the BS soot.

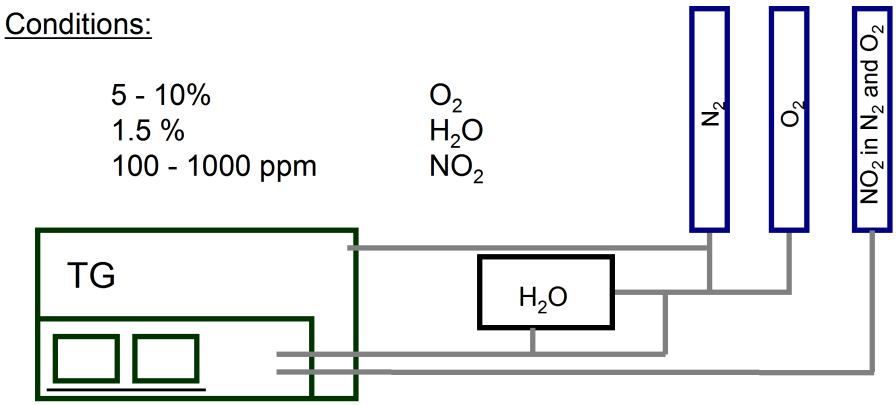

Fig. 6.13: Setup for exhaust relevant investigations.

As the setup for exhaust gas treatment system requires the use of NO_2 for a continuous reaction, the overall experimental conditions for gas phase are adjusted to engine exhaust gas values. The gas phase products are transferred through a heated quartz capillary to a quadrupole mass spectrometer operated in SIM mode (Thermoster, Balzers). In order to obtain relevant results for realistic exhaust gas conditions, a Seiko Thermobalance is used. A schematic drawing is given in Fig. 6.13. Note that the addition of NO_2 to the gas phase takes place as late as possible, to avoid the reaction of NO_2 and H_2O to HNO_3. The samples are loaded into the TG oven at room temperature. The NO_2 is added to the atmosphere. The gases stabilize, then the TPO experiment is started.

6.3.2 Influence of NO_2

GfG soot

The GfG soot is oxidized with different amounts of NO_2 in 10% O_2, 1.5% H_2O, balance N_2. The NO_2 content is varied between 0 and 1000 ppm. A heating rate of 5 K/min is used in the experiments. Fig. 6.14 shows the mass loss over temperature for the different NO_2 concentrations.

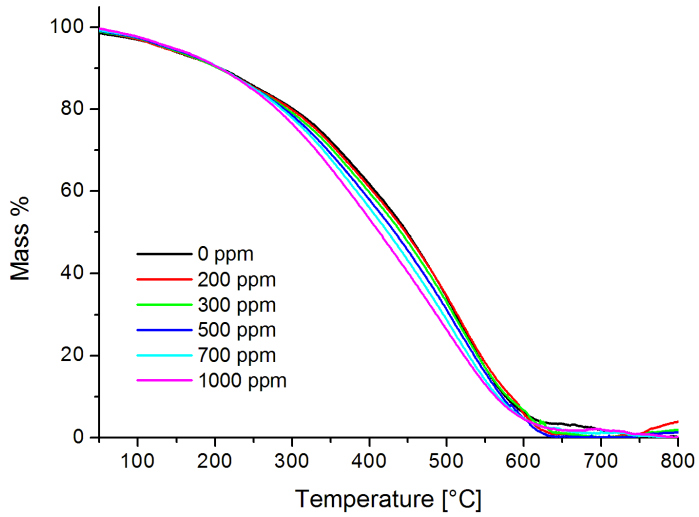

Fig. 6.14: GfG soot: TG/TPO experiments. The sample is heated in in 10% O_2, 1.5% H_2O, balance N_2, with varying amount of NO_2 in the oxidizing atmosphere.

The NO_2 concentration does not significantly influence the mass loss behavior in the temperature range between 50 °C and 200 °C. Fig. 6.14 shows that the measurements in the different gas atmospheres are superpositioned above each other. In the temperature range between 200 °C and 590 °C the influence of the oxidizing agent NO_2 is revealed. The mass loss over temperature is increased with higher amount of NO_2 in the gas feed. The enhancement of NO_2 amount increases the soot oxidation rate. Considering the mass loss at 400 °C it is observed in the case of no NO_2 in the gas phase approximately 39% of the soot has been oxidised. In the case of 500 ppm NO_2 in the gas feed the mass loss is slightly higher: 42%. Adding 1000 ppm NO_2 to the oxidative atmosphere the soot has lost 47% of its original mass. Within the limits of accuracy of the Seiko Thermobalance ($\pm$ 50–100 μg), the temperature at which the soot is oxydized is not changed. The combustion is completed at 600 °C. Fig. 6.15 shows the MS Data analysis for two of the TG experiments described in Fig. 6.14. As examples two sets of data are chosen: 10% O_2 in N_2 and the addition of 500 ppm NO_2. The MS Signal for m/e = 44 is divided by

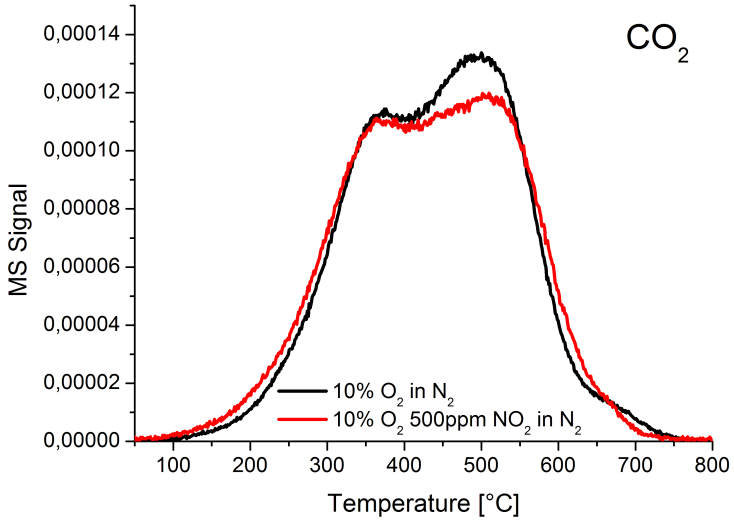

Fig. 6.15: MS data CO_2 signal m/e = 44 for TG experiments on the GfG soot with 10% O_2 in N_2 and the addition of 500 ppm NO_2.

the MS signal m/e = 28 in order to care for change in MS sensitivity, a background is substracted. The results are mass normalized. Fig. 6.15 reveals slight differences in CO_2 evolution during oxidation of the GfG soot. In the case of the experiment without NO_2 the results already described in section 6.1 (5% O_2) are essentially reproduced. The evolution of CO_2 begins at 100 °C. Two maxima are being resolved at 380 °C and 500 °C. The signal drops slowly to zero at 750 °C where the soot is completely consumed. In the case of NO_2 addition the overall CO_2 evolution during oxidation of the GfG soot changes slightly as expected. The CO_2 signal starts to rise at a lower temperature of around 70 °C. The signal rises faster, showing an increase in the oxidation rate at lower temperatures. The first maximum in CO_2 generation is at 370 °C, the second at 510 °C. The soot appears to be oxidized earlier as the CO_2 signal drops to zero at 700 °C.

Fig. 6.16 shows the results of three ramp rate experiments to model the soot oxidation. Three ramp rates are used: 2, 5, 8 K/min respectively. A Friedman model free analysis for the two sets of experiments is presented in Fig. 6.17. The differences in the curves are due to the earlier mass loss in the case of the NO_S containing atmosphere. The Friedman Analysis provides information about the apparent activation energy. The apparent activation energies for the respective oxidation experiments are given in Fig. 6.17. To model the oxidation of the GfG soot, four independent reactions are fitted. In order to predict the mass loss in an atmosphere of 500 ppm NO_2 in 10% O_2, balance N_2, a model fitting is done as demonstrated in the case of the comparative analysis of the different soot and carbon black materials. It is

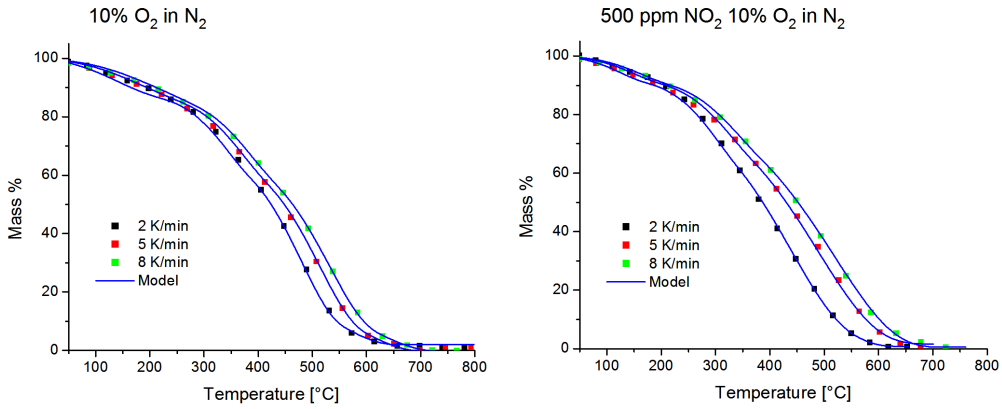

Fig. 6.16: Ramp rate experiments with the GfG soot

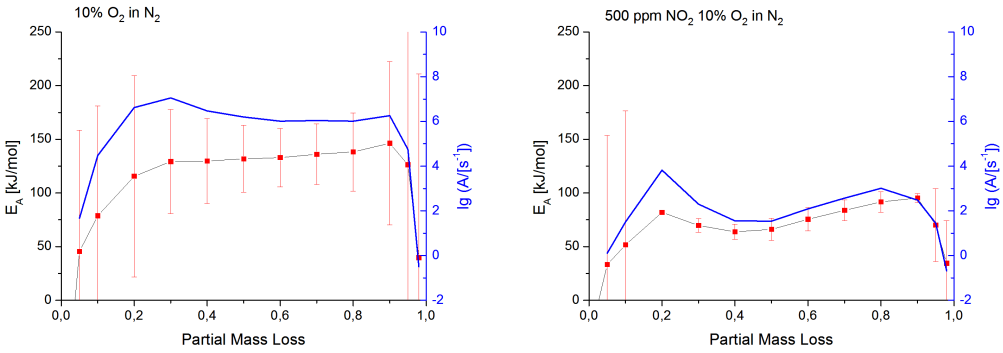

Fig. 6.17: Apparent activation energies calculated with the Friedman analysis of data in Fig. 6.16

possible to model the reaction behavior with four independent steps of oxidation. The models are chosen as in the previous case of the GfG soot oxidation, the models being the same: Four independent steps representing a 3–dim. Jander's type diffusion (Table 6.3).

Table 6.3: Models and fit parameters used to describe the oxidation of the GfG soot. The results are used to calculate the predictions.

Model Step 1: 3-dim. diffusion Janders type			
Model Step 2: 3-dim. diffusion Janders type			
Model Step 3: 3-dim. diffusion Janders type			
Model Step 4: 3-dim. diffusion Janders type			
10% O_2 in N_2		10% O_2 500 ppm NO_2 in N_2	
lg A_1 [s^{-1}]:	0,84	lg A_1 [s^{-1}]:	2,66
E_1 [kJ/mol]:	39,14	E_1 [kJ/mol]	49,86
lg A_2 [s^{-1}]:	4,92	lg A_1 [s^{-1}]:	1,02
E_2 [kJ/mol]:	101,85	E_1 [kJ/mol]	71,67
lg A_3 [s^{-1}]:	3,94	lg A_1 [s^{-1}]:	4,67
E_3 [kJ/mol]:	127,78	E_1 [kJ/mol]	92,26
lg A_4 [s^{-1}]:	4,61	lg A_1 [s^{-1}]:	6,78
E_4 [kJ/mol]:	126,47	E_1 [kJ/mol]	170,28
Ind. React. 1:	0,12	Ind. React. 1:	0,07
Ind. React. 2:	0,19	Ind. React. 2:	0,70
Ind. React. 3:	0,20	Ind. React. 3:	0,11

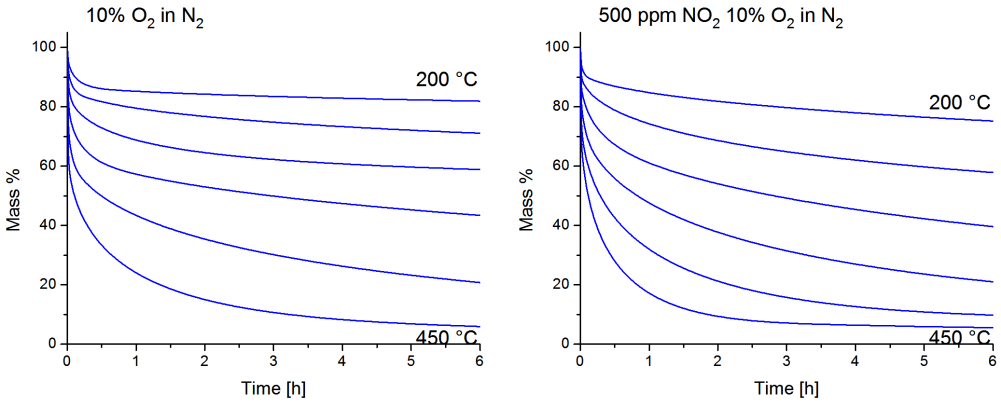

Fig. 6.18: Predictions for mass loss of the GfG soot at different temperatures in isothermal conditions.

The calculated predictions for the mass loss over time at different temperatures are given in Fig. 6.18. Apparently with the addition of NO_2 to the oxidative gas phase, the soot oxidation is not increased significantly. The total burnout after 6 h remains practically unaffected whereas in the early stages of oxidation the rate appears to be increased.

Euro IV HD diesel engine soot

The Euro IV diesel engine soot is oxidized with different amounts of NO_2 in 10% O_2, 1.5% H_2O, balance N_2. The NO_2 content is varied between 0 and 1000 ppm. A heaing rate of 5 K/min is used in the experiments. Fig. 6.19 shows the mass loss over temperature for the different NO_2 concentrations.

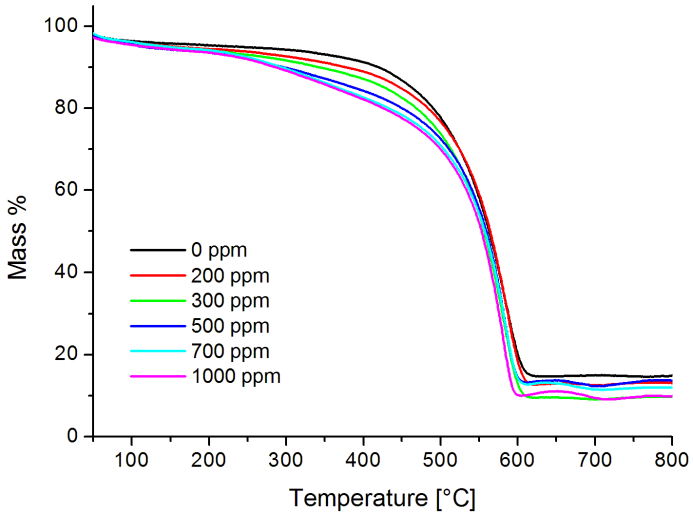

Fig. 6.19: Euro IV soot: TG/TPO experiments. The sample is heated in in 10% O_2, 1.5% H_2O, balance N_2, with varying amount of NO_2 in the oxidizing atmosphere.

In the temperature range between 250 °C and 450 °C the influence of the oxidizing agent NO_2 is revealed. The mass loss over temperature is increased with higher amount of NO_2 in the gas feed. Considering the mass loss at 400 °C it is observed in the case of no NO_2 in the gas phase approximately 10% of the soot has been oxidised. In the case of 500 ppm NO_2 in the gas feed the mass loss is slightly higher: 15 %. With the addition of 1000 ppm NO_2 to the oxidative atmosphere the soot has lost 20% of its original mass. At higher temperatures, the mass loss from oxidation is not enhanced anymore. However the total burnout temperature of the soot remains unaffected. The curves do not change at higher temperatures ($>$ 450 °C), i.e. the mass loss over temperature is the same for the five single experiments. The remaining weight in the TG experiments is found to be ash from engine lubricant oil. Apparently the amount of ash is inhomogeneous as the amout of remnant is different after the oxidation of the Euro IV soot.

Fig. 6.20 shows the MS Data analysis for two of the TG experiments described in Fig. 6.19. As examples two sets of data are chosen: 10% O_2 in N_2 and the addition of 500 ppm NO_2. The MS Signal for m/e = 44 is divided by the MS signal m/e = 28

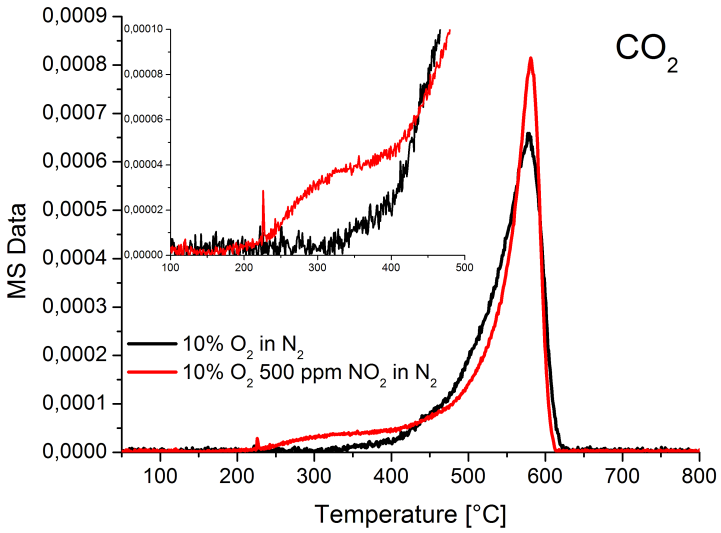

Fig. 6.20: MS data CO_2 signal m/e = 44 for TG experiments on the Euro IV diesel engine soot with 10% O_2 in N_2 and the addition of 500 ppm NO_2.

in order to care for change in MS sensitivity, a background is substracted. The results are mass normalized. Fig. 6.20 reveals differences in CO_2 evolution during oxidation of the Euro IV diesel engine soot. In the case of the experiment without NO_2 the results already described in section 6.1 could be reproduced. The evolution of CO_2 begins at 380 °C, where also the first mass loss is observed in Fig. 6.19. The CO_2 signal goes through a maximum at 580 °C where the rate in mass loss also reaches its maximum. The soot is completely oxidized at 630 °C, the MS signal for CO_2 drops to zero. The addition of NO_2 changes the oxidative behavior of the Euro IV soot. A CO_2 evolution at lower temperatures is observed, the inset in Fig 6.20 shows the onset to be at 250 °C. The maximum in CO_2 evolution is at 580 °C, corresponding to the maximal rate in mass loss. The soot is burnt at 610 °C, the CO_2 signal returns to zero.

Fig. 6.21 shows the results of three ramp rate experiments to model the soot oxidation. Three ramp rates are used: 2, 5, 8 K/min respectively. Fig. 6.22 shows the results of the model free analysis for the two sets of experiments. The differences in the curves are due to the earlier mass loss in the case of the NO_2 containing atmosphere. The Friedman Analysis provides information about the apparent activation energy. The apparent activation energies for the respective oxidation experiments are given in Fig. 6.22. The NO_2 enhances the oxidation at low temperatures. The apparent activation energy is reduced. At a higher fraction of mass loss the model free estimation E_A is unaffected. This analysis shows two major steps in the overall oxidation. The soot oxidation appears to be governed by O_2 at higher temperatures

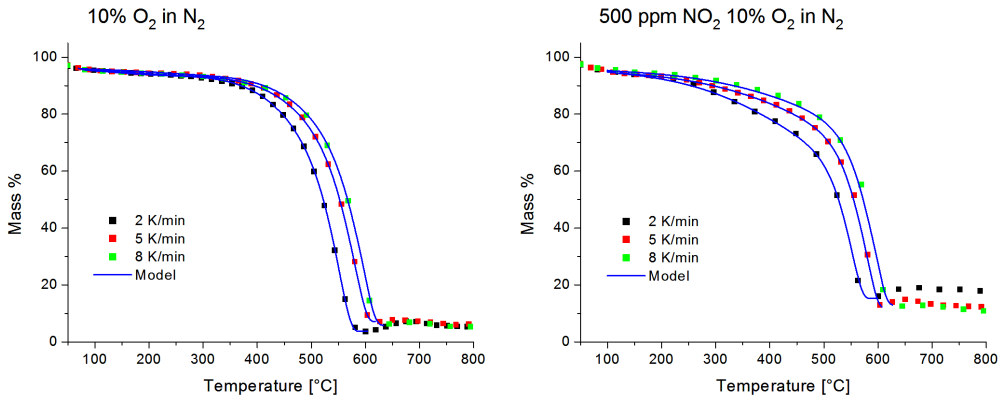

Fig. 6.21: Ramp rate experiments with the Euro IV soot

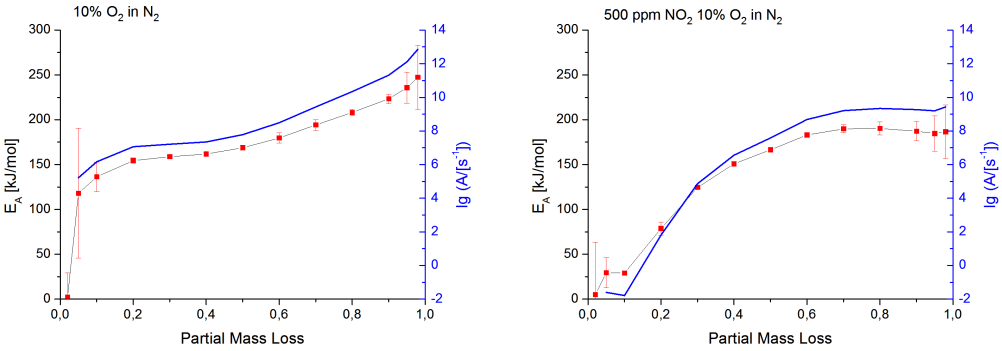

Fig. 6.22: Apparent activation energies calculated with the friedman analysis.

(> 400°C). In this way, at higher temperatures, the reaction path changes and the direct oxidation becomes faster. In this case the NO_2 concentration will not have any influence anymore on the soot oxidation.

In order to predict the mass loss in an atmosphere of 500 ppm NO_2 in 10% O_2 balance N_2, a model fitting is done as demonstrated in the case of the comparative analysis. It is possible to model the reaction behavior with three steps of oxidation. The model is chosen as in the previous case of the Euro IV oxidation, the models being the same: Three independent steps, 3–dim. diffusion, shrinking core (Table 6.4).

Table 6.4: Models and fit parameters used to describe the oxidation of the Euro IV diesel engine soot. The results are used to calculate the predictions.

Model Step 1: 3-dim. diffusion Janders type			
Model Step 2: 3-dim. diffusion Janders type			
Model Step 3: 3-dim. phase boundary reaction			
10% O_2 in N_2		10% O_2 500 ppm NO_2 in N_2	
lg A_1 [s^{-1}]:	0,38	lg A_1 [s^{-1}]:	0,67
E_1 [kJ/mol]:	37,08	E_1 [kJ/mol]	48,80
lg A_2 [s^{-1}]:	4,82	lg A_1 [s^{-1}]:	0,76
E_2 [kJ/mol]:	130,04	E_1 [kJ/mol]	47,73
lg A_3 [s^{-1}]:	8,24	lg A_1 [s^{-1}]:	8,02
E_3 [kJ/mol]:	185,13	E_1 [kJ/mol]	180,71
Ind. React. 1:	0,02	Ind. React. 1:	0,22
Ind. React. 2:	0,36	Ind. React. 2:	0,12

Thus the oxidation in isothermal cases can be predicted, as given in Fig. 6.23.

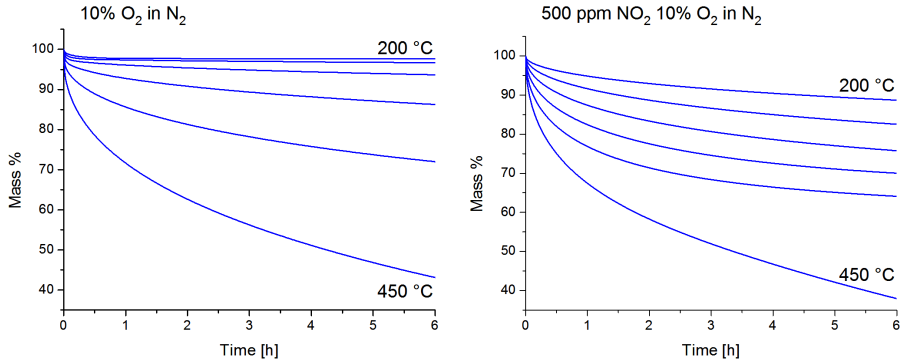

Fig. 6.23: Predictions for mass loss of the Euro IV soot at different temperatures in isothermal conditions.

The predictions of the combustion are calculated with six different temperature settings 200 °C, 250 °C, 300 °C, 350 °C, 400 °C, 450 °C. The oxidation of soot occurs in the case with NO_2 at lower temperatures and with a higher rate as in the case without NO_2. The mass loss over time is higher.

Black Smoke soot

The BS soot is oxidized with different amounts of NO_2 in 10% O_2, 1.5% H_2O, balance N_2. The NO_2 content is varied between 0 and 1000 ppm. A heating rate of 5 K/min is used in the experiments. Fig. 6.24 shows the mass loss over temperature for the different NO_2 concentrations.

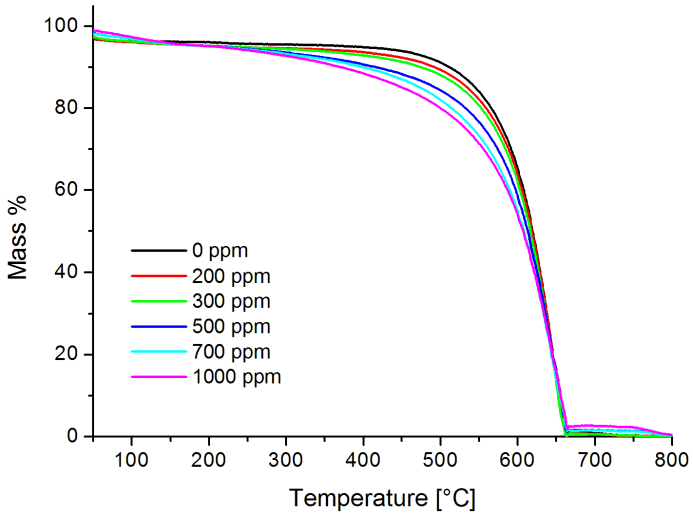

Fig. 6.24: Euro IV soot: TG/TPO experiments. The sample is heated in in 10% O_2, 1.5% H_2O, balance N_2, with varying amount of NO_2 in the oxidizing atmosphere.

The NO_2 concentration does not influence the mass loss behavior in the temperature range between 50 °C and 200 °C. Fig. 6.24 shows that the measurements in the different gas atmospheres are superpositioned above each other. In the temperature range between 200 °C and 650 °C the influence of the oxidizing agent NO_2 is revealed. The mass loss over temperature is increased with higher amount of NO_2 in the gas feed. The higher amount of the NO_2 increases the soot oxidation. Three examples are chosen to demonstrate this fact: At 500 °C, with 0 ppm NO_2 in the gas phase approximately 10% of the soot has been oxidised. In the case of 500 ppm NO_2 in the gas feed the mass loss is considerably higher: 15 %. Adding 1000 ppm NO_2 to the oxidative atmosphere results in a loss of 20% of its original mass. The burnout temperature where the soot is completely oxidized remains unaffected for the different amounts of the NO_2.

Fig. 6.25 shows the MS Data analysis for two of the TG experiments described in Fig. 6.24. As examples two sets of data are chosen: 10% O_2 in N_2 and the addition of 500 ppm NO_2. The MS Signals for m/e = 44 are divided by the MS signal m/e = 28 in order to care for change in MS sensitivity, a background is substracted. The re-

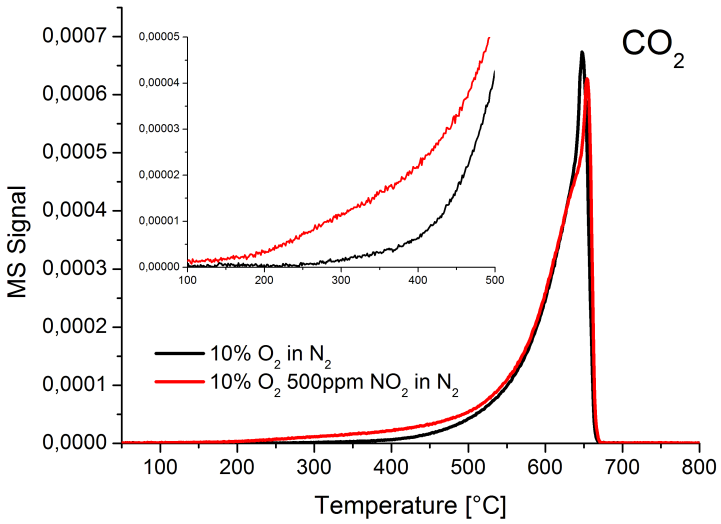

Fig. 6.25: MS data CO_2 signal m/e = 44 for TG experiments on the BS soot with 10% O_2 in N_2 and the addition of 500 ppm NO_2.

sults are mass normalized. Fig. 6.25 reveals differences in CO_2 evolution during oxidation of the BS soot. In the case of the experiment without NO_2 the results already described in section 6.1 could be basically reproduced. The evolution of CO_2 begins at 400 °C as shown in the inset in Fig. 6.25. The signal reveals a maximum at 645 °C and goes to zero at 670 °C as the soot is then completely oxidized. The maximum in CO_2 generation corresponds to the maximum rate in mass loss. In the case of NO_2 addition the MS signal increases at lower temperatures. The evolution of CO_2 begins at 150 °C. The CO_2 generation is higher at lower temperatures (150–600 °C) compared to the experiment without NO_2. The signal shows a maximum at a slightly higher temperature: 655 °C. Also under these conditions the soot is burnt at 670 °C as the MS signal drops to zero.

Fig. 6.26 shows the results of three ramp rate experiments to model the soot oxidation. Three ramp rates are used: 2, 5, 8 K/min respectively. In order to predict the mass loss in an atmosphere of 500 ppm NO_2 in 10% O_2, balance N_2 and 10% O_2 in N_2. Fig. 6.27 shows the Friedman model free estimation of the activation energies for the two sets of experiments. The differences in the curves are due to the earlier mass loss in the case of the NO_S containing atmosphere. The apparent activation energies for the respective oxidation experiments is given in Fig. 6.27. The apparent activation energy at low conversion is reduced. At a higher fraction of mass loss the model free estimation E_A is unaffected. This analysis shows two major steps in the overall oxidation.

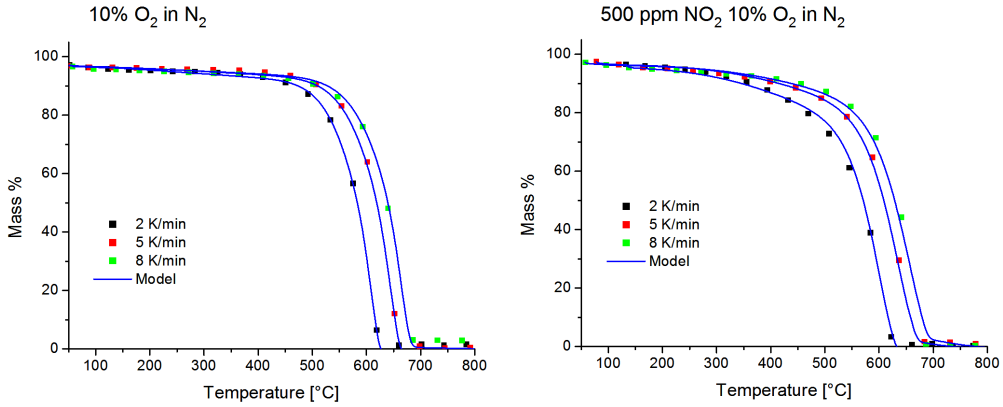

Fig. 6.26: Ramp rate experiments with the BS soot.

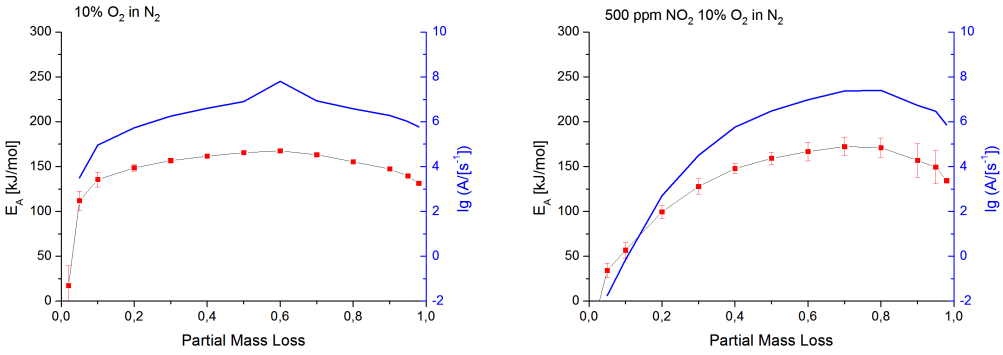

Fig. 6.27: Apparent activation energies calculated with the friedman analysis.

Table 6.5: Models and fit parameters used to describe the oxidation of the Back Smoke soot. The results are used to calculate the predictions.

Model Step 1: 3-dim. diffusion Janders type			
Model Step 2: 3-dim. Avrami–Erofeev			
Model Step 3: 3-dim. phase boundary reaction			
10% O_2 in N_2		10% O_2 500 ppm NO_2 in N_2	
lg A_1 [s^{-1}]:	0,24	lg A_1 [s^{-1}]:	0,83
E_1 [kJ/mol]:	23,78	E_1 [kJ/mol]	17,14
lg A_2 [s^{-1}]:	5,49	lg A_1 [s^{-1}]:	0,60
E_2 [kJ/mol]:	146,18	E_1 [kJ/mol]	55,27
lg A_3 [s^{-1}]:	8,75	lg A_1 [s^{-1}]:	8,04
E_3 [kJ/mol]:	202,53	E_1 [kJ/mol]	181,37
Ind. React. 1:	0,06	Ind. React. 1:	0,01
Ind. React. 2:	0,50	Ind. React. 2:	0,22

It is possible to model the reaction behavior with three steps of oxidation. The model is chosen as in the previous case of the BS soot oxidation, the models being the same: three independent steps, 3–dim. diffusion, Avrami Erofeev and 3–dim. shrinking core (Table 6.5).

The following Fig. 6.28 shows the calculated isothermal behavior for the BS soot. As is to be expected, the soot will not lose mass significantly during oxidation in 10% O_2 in N_2 at temperatures between 200 °C and 450 °C. Whereas in the case of

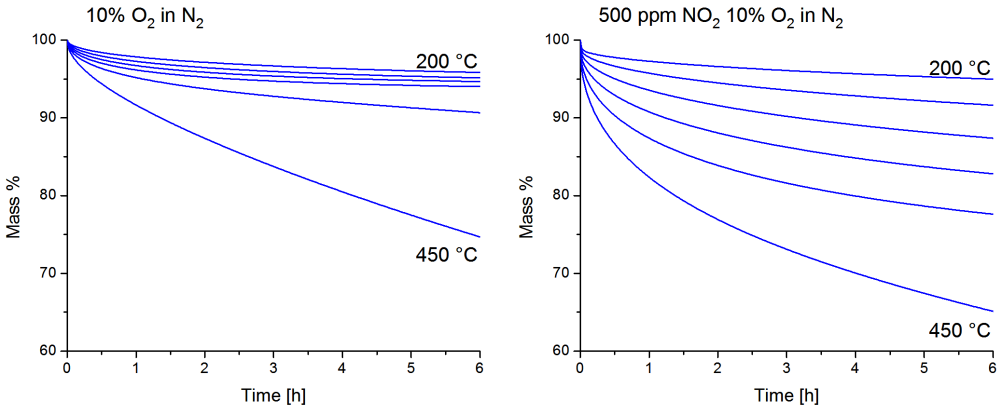

Fig. 6.28: Predictions for mass loss of the BS soot at different temperatures in isothermal conditions.

oxidation with NO_2 in the gas phase the oxidation is increased, the soot loses mass significantly at already lower temperatures. In the case of a rise in temperatures up to 450 °C, the mass loss over time is increased.

6.4 Discussion

6.4.1 Carbon Oxidation

The Role of O_2

Two independent reaction mechanisms have been proposed for the oxidation of graphite surfaces [119, 120]: 1. a surface migration mechanism, being the reaction of the migrating oxygen molecules that are first adsorbed on nonreactive sites (Langmuir–Hinshelwood mechanism), 2. reaction from collisions of O_2 molecules with a reactive carbon site (Eley–Rideal mechanism). The reaction mechanism according to the Langmuir–Hinshelwood formalism consists basically of the following steps: the physisorption of molecular oxygen on the graphitic basal surfaces, and the diffusion of these species to defect sites that subsequently results in the formation of carbon–oxygen surface functional groups . The Eley–Rideal mechanism is initiated by the direct collision of the oxygen molecules with the graphitic defect sites. These steps are presented in the following. The oxidation reaction is a gas–solid state reaction which requires two independent types of electronically different sites. One site should be electron rich to activate molecular oxygen (**A**); the other site should be electron–deficient to react with activated oxygen atoms (**C**). The generation of oxygen functional groups can be considered as a preparation of intermediate states of the oxidation process of carbon to CO/CO_2. One step is the reductive activation of the reagent producing an oxygen di–anion: the following sequence is suggested [73]:

$$2(\mathbf{A}) + \mathrm{O_2} \longrightarrow \mathrm{O_2(ads)} \tag{6.9}$$

$$\mathrm{O_2}(ads) + 2\mathrm{e^-} \longrightarrow \mathrm{O_2^{2-}(ads)} \tag{6.10}$$

$$\mathrm{O_2^{2-}(ads)} + 2\mathrm{e^-} \longrightarrow 2\mathrm{O^{2-}(ads)} \tag{6.11}$$

$$\mathrm{O^{2-}(ads)} + (\mathbf{C}) \longrightarrow \mathrm{CO(ads)} + 2\mathrm{e^-} + (\mathbf{A}) \tag{6.12}$$

This can either occur by chemisorption and reductive dissociation at the basal planes of sp^2 carbon, or by direct activation of a radical centre formed by a dangling bond of an sp^2/ sp^3 carbon atom at the surface. For materials such as the investigated soot and carbon black whose graphenes are characterized by highly reactive edge planes, oxidation does not necessarily require physisorption. Thus, the oxidation mechanism of the graphenes, involves only a single step, which is the Eley–Rideal mechanism. As these centres are very reactive they will only be present during gasification or during formation of solid carbon from atomic carbon sources. In this

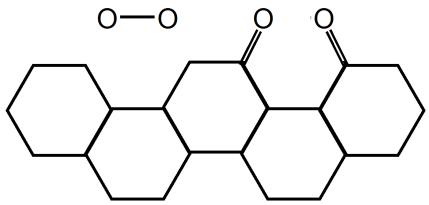

Fig. 6.29: Reaction of molecular oxygen with an armchair edge of a graphene sheet.

mechanism, the oxidation of a carbon surface is initiated by the direct collision of an oxygen molecule with the reactive edges (armchair or zig–zag) of the graphene sheet [119, 120]. Oxygen molecules approaching the edges of graphenes (Fig. 6.29) are reduced by charge transfer from the carbon atoms in these planes. This breaks the O–O bond exothermically without an activation barrier, and results in the formation of carbon–oxygen functional groups. The necessary electrons come from the conduction band of the graphite valence electrons. The second reaction is the diffusion of the activated oxygen di–anion to a site of covalent bond formation which must be a prismatic edge/defect site in sp^2 carbons. In strongly bent carbons of fullereneoid structures this site may also be a localized double bond at the curved graphene sheet where an epoxide ring structure is formed. At too high temperature the C–O complex will desorb as CO. At too high temperatures and under excess of activated oxygen a CO_2 group will form and desorb as carbon dioxide. This is described with the following sequence:

$$\mathrm{CO(ads)} \longrightarrow \mathrm{CO(gas)} + \mathbf{C} \tag{6.13}$$

$$\mathrm{O^{2-}} + \mathrm{CO(ads)} \longrightarrow \mathrm{CO_2(ads)} + 2\mathrm{e^-} + (\mathbf{A}) \tag{6.14}$$

$$\mathrm{CO_2(ads)} \longrightarrow \mathrm{CO_2(gas)} + \mathbf{C} \tag{6.15}$$

This sequence of events requires two sites ranging from ionic to covalent or to a distribution of sites with varying energy of oxygen chemisorption. A sketch of the reaction is given in Fig. 6.30. This process requires the presence of weakly bound electrons in order to split the oxygen double bond (step 1 in Fig. 6.30). Such electrons are available on the basal planes of graphitic carbon. **A** are the graphene planes with their delocalized electrons more weakly bound than in aromatic molecules. The oxygen atoms will diffuse (step 2) on the surface using their excess dissociation energy until they either recombine and desorb or find a structural defect **C** where they can form a covalent bond to carbon (step 3, 4). This reaction is a an oxidation reaction in which the directly bonding carbon atom loses two electrons which flow back into the reservoir of the graphene layer. The resulting CO complex can

either desorb (3a, 4a) or survive depending on the energy available. This amount of activation energy depends on the carbon microstructure and onto which site the carbon is bound to. The desorption of the oxidation product leaves in any case an empty site for a new attack of an oxygen atom. An efficient oxidation requires the presence of electrons from graphene layers and sufficient defect sites for reaction of the activated carbon. At intermediate temperature a carbon oxygen group with low disturbance of the graphene will form. At very low temperature a complex carbon–oxygen group with strong disturbance of the graphene layer will form. It occurs that reaction temperature and abundance of activated oxygen (partial pressures) are important parameters determining the chemical nature of resulting functional groups as well as the specific ease with which a given carbon–oxygen functionality is formed. This renders it clear that on structurally inhomogeneous surfaces (prismatic faces and defects) a wide variety of functional groups will begin to exist as soon as the reaction temperature is too low to permit a complete oxidation.

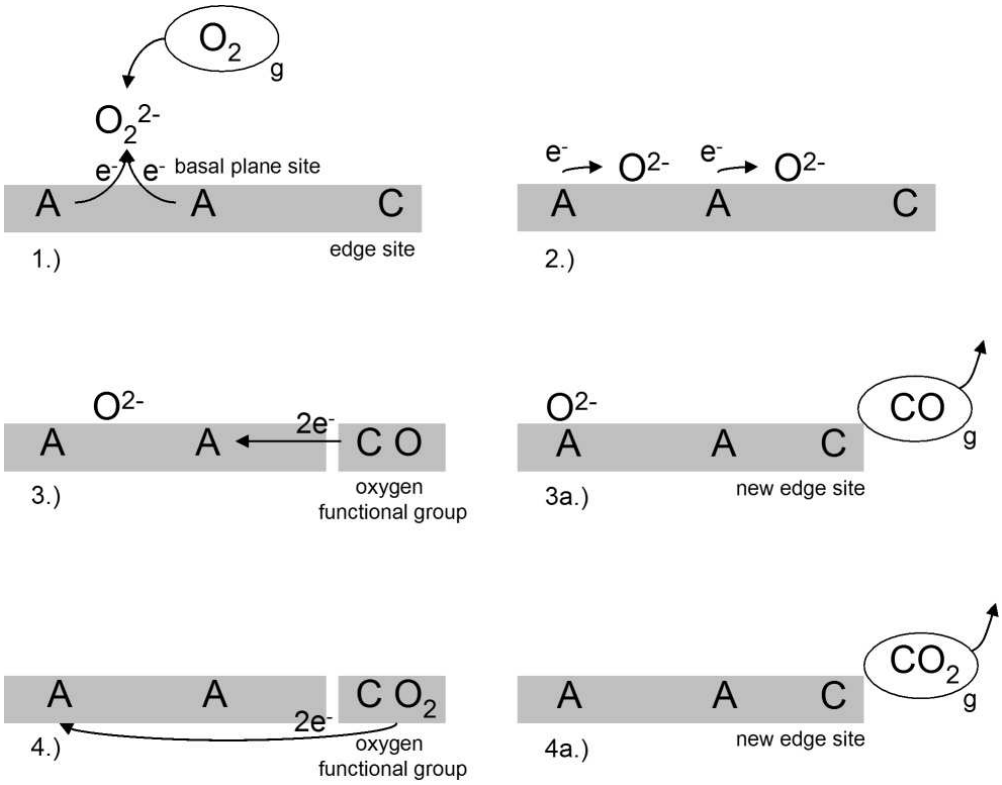

Fig. 6.30: Sketch of the model for carbon oxidation. The steps of adsorption and dissociation of the oxygen, the formation of oxygen functional groups as well as the desorption of Co and CO_2 respectively are shown.

The oxidation rate of carbonaceous materials in air is strongly dependent on parameters such as the surface area and crystallographic structure. The crystallographic structure of carbon consists of distinct surface sites, i.e. basal plane and edge sites.

Highly graphitized carbons have a preponderance of basal plane sites that are less reactive than disordered carbons that contain a larger fraction of edge or active sites.

The Role of NO_2 in addition to O_2

Due to its reactivity, NO_2 initiates the creation of O–containing sites intermediates [118, 121], which are more reactive than the complexes that have already existed. As a consequence, O_2 is able to react with them [8, 122–124]. In the following the NO_2/O_2–soot reaction phenomena are discussed based on reaction mechanism schemes [125]. As basis, the generally accepted reaction scheme for the oxidation of carbonaceous material is used. In the NO_2/O_2 mixture the formation of oxygen groups is initiated by NO_2, the reactions are described as in Fig.6.31.

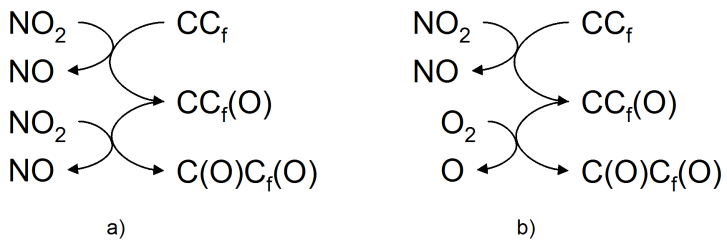

Fig. 6.31: Sceme showing the generation of surface functional groups in the oxidising atmosphere.

The decomposition of oxygen functional groups can occur through thermal dissociation of intermediates or through the reaction with O_2 (Fig. 6.32a) and NO_2 (Fig. 6.32b):

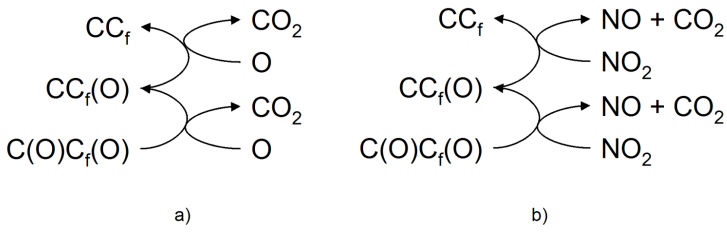

Fig. 6.32: Oxidation of surface oxygen groups during the oxidation process.

In the genesis of oxygen functional groups with NO_2/O_2 mixture, O_2 is present abundantly in comparison to NO_2. So, among the total oxidation of the oxygen surface groups, the Oxidation with O_2 will dominate the reactions. According to the reaction scheme, O_2 plays a role in the formation of less stable complexes and in the decomposition of the oxygen functional groups. It is suggested that carboxylic

acid and/or lactone are the major species responsible for the CO and CO_2 formation [126,127].

6.4.2 Linking Microstructure with Reactivity

Within the carbon black literature, various models have been developed to describe the structure of soot. Long considered equivalent to amorphous carbon, soot does not possess a periodic crystalline structure. Instead, short graphene segments are often found grouped together in short stacks, called crystallites. Within each crystallite, the segments of carbon atom layer planes are stacked and randomly rotated with respect to each other along the c–axis, an arrangement called turbostratic structure as seen in the HRTEM micrographs. The dimensions of the crystallite stacks vary considerably between different carbon blacks (Fig. 4.12). Additionally theoretical models for carbon gas phase reactions have been developed [128].

It is particularly important to note that the basic unit of soot, the graphene segment with planar dimensions of generally less than a few nanometers, consists of carbon atoms located at basal plane and edge site positions. Yet by atomic similarity with coal char [129–131] and graphite [132–134], the relative number and accessibility of potential reactive carbon layer edge sites (aryl C–H bonds) is dependent on the soot nanostructure. These sites are potentially accessible for reaction with O_2 or NO_2 (oxidation). Larger (longer) graphene layer planes, larger (and hence fewer) crystallites and concentrically oriented crystallites (lower edge site accessibility) result in fewer potential reaction sites [11], or sites of lower reactivity. As revealed by the combination of the TEM measurements and the TG experiments, the fullerenoid small graphenes are more easily oxidized than the stacked flat graphenes forming the BSUs and the spherical particles. Thus, the number of such potential sites is a direct reflection of the detailed soot particle nanostructure. Graphite oxidation proceeds anisotropically, i.e. the reactivity of basal plane carbon atoms is far lower than that of edge site carbon atoms [134]. Consistent with these results are the measured oxidation rates of graphitized carbon blacks exhibiting higher threshold temperatures and much slower rates than the non–graphitized GfG Soot and the Euro IV HD diesel engine soot.

Geometrically, carbon atoms in edge sites can form bonds with chemisorbed oxygen due to the availability of unpaired sp^2 electrons. Carbon atoms in basal planes have only shared π electrons forming chemical bonds. Consequently, the observed reactivity will be an average of basal vs. edge site carbon atom reactivities for graphitic layer planes of finite dimensions [135]. As the layer plane size decreases, the number of edge site carbon atoms will necessarily increase in proportion to the

number of basal plane carbon atoms, allowing one to expect the overall reactivity to increase. This leads to the observed structure reactivity correlation. The GfG soot, for example, is more easily oxidized due to the small strong bent graphenes. The Furnace Soot and the Lamp Black exhibit flat graphenes stacked to form the well known BSUs. Here the material is less prone to oxidation. In addition to the size of the graphene segments, their relative curvature will also impact on their oxidation rate. Curvature arises from non–6–membered rings within the aromatic framework. This curvature imposes bond strain as the orbitals overlap, and the electronic resonance stabilization is lessened [136]. Therein the C–C bonds are weakened and individual atoms are more exposed, i.e. they are more susceptible to oxidative attack [137, 138]. It is for these same reasons that fullerenes and carbon nanotubes are less resistant toward oxidation than planar graphite. A larger degree of curvature (smaller radius of curvature) increases the imposed bond strain and hence the resistance toward oxidation decreases, as has been found for carbon nanotubes of different diameters [139, 140]. This duality of reactive sites forms the physical basis for the soot oxidation rate expression which takes into account both edge and basal plane carbon sites and their associated reactivities [141]. This semi-empirical model is based on pyrolytic graphite, a structure with extended basal planes and correspondingly few edge site carbon atoms. Consequently, the overall oxidation rate would be expected to be relatively low compared to most other carbons possessing a less graphitic structure as in the case of the soot. It still is an issue to find a corresponding model or rate expression that takes into account the curvature of graphitic layer planes and the associated impact upon oxidative stability. The effects of oxygen and hydrogen heteroatoms has always to be taken into account. The overall reactivity of a soot particle toward oxidation depends upon its nanostructure, i.e. the size, orientation, and organization of the graphene layer planes. Variations in the graphene layer plane dimensions, curvature, and relative orientation influence the reactivity of the individual graphene segments, and hence the overall particle reactivity, as evidenced in the TEM/TG experiments.

The GfG Soot is the most reactive soot of all four investigated materials. The reason is the very defective structure which is observed in the TEM micrographs. The material consists of fine subunits not larger than 3 nm building up agglomerates with a high surface area. Strongly bent graphenes lead to localized double bonds resulting in an olefinic structure [16]. Theoretical investigations of nanocarbons predict the influence of geometric changes on chemical properties (increasing reactivity upon increasing curvature) [142, 143]. The graphenes in this soot are small as seen in Fig. 4.10a. This increases the ratio of carbon atoms on graphene edge sites to carbons in the center of the graphene sheet. A high ratio between border carbon and graphene carbon is equivalent to high reactivity and the carbon is more easily converted to

CO_2. Carbon atoms in edge sites can form bonds with chemisorbed oxygen and hydrogen due to the availability of unpaired sp^2 electrons, while carbon atoms in basal planes are more aromatic, having only shared π–electrons to form chemical bonds [12]. TEM and TPO results are in perfect agreement, as evidenced by the low apparent activation energy that is needed to oxidize the GfG Soot (130 kJ/mol). The coordination of the carbons in the defective graphenes must be completed, and this is achieved through functional groups as shown in the DRIFT spectra. Additionally oxygen containing functional groups attached to non six membered rings may occur as very reactive sites [108]. The high reactivity is expressed in an early CO_2 evolution starting at 250 °C. The first maximum in the CO_2 profile at 340 °C coincides with a considerable H_2O evolution, indicating the combustion of the hydrogen–rich functional groups. The second maximum in CO_2 production (at 520 °C) is accompanied by a smaller H_2O signal and is most likely due to the oxidation of the remaining graphenes.

The Euro IV heavy duty diesel engine soot is less reactive than the GfG Soot but still more than the BS Soot and the Furnace Soot. The analysis of the apparent activation energy necessary to oxidize the Euro IV Soot results in an intermediate value: 150 kJ/mol. One reason is seen in the size distribution of primary particles, the majority of the particles has a size of 10 – 15 nm. Comparing the TEM images the Euro IV Soot appears more compact and thus less accessible to oxygen than the GfG Soot. However, the crucial reason is seen in the multi–shell like fullerenoid structure with the defective surface. The defective non six membered rings may produce, as already described for the GfG Soot, highly localized olefinic electronic structures prone to the addition of molecular oxidants [144]. However, the DRIFT spectra do not reveal C–H vibrations as for the GfG Soot but predominantly C=O and O–H vibrations. As a consequence the MS–data from the TPO studies show an onset of H_2O evolution at a lower temperature than the evolution of CO_2. Not only the morphology but also the surface chemistry of the Euro IV Soot differs from that of the GfG Soot.

The BS Soot as well as the Furnace Soot is less prone to oxidation due to the well developed graphitic properties. The graphenes are flat, indicating a less defective structure. One observes domains where graphenes are stacked forming graphitic nanocrystallites. The ratio of "border" to "in plane" carbons is low. These structures decrease the reactivity [58, 141]. Additionally the local density is higher. The higher apparent activation energies, 160 and 210 kJ/mol, as obtained from the TG measurements, are a clear indication of these influences [9]. A lower amount of defects should result in fewer functional groups and this is reflected in the DRIFT spectra. However the spectra do not differ significantly from that of the Euro IV

Soot. In the case of the BS Soot, the MS-data show a slight H_2O – formation at temperatures around 320 °C. In the case of the Furnace Soot, such a signal is missing.

The high rate of oxidation of the GfG Soot and the Euro IV Soot is due to the defective graphenes that are more reactive than these of the BS Soot and the Furnace Soot. The TG analysis shows that the fullerene–like soot is easier to oxidize than well graphitized samples. This morphology/microstructure – controlled reactivity of soot is in agreement with earlier findings in temperature–programmed oxidation studies [145] which show that as the concentration of non–six–membered carbon rings with their olefinic electronic structure increases, and with the presence of chemically reactive prism edges, nanocarbons with fullerenoid structure become more reactive than the more graphitized technical carbon blacks.

The oxidation experiments of the GPAH also reveal a structure reactivity correlation. The Graphene Ribbon structure is more prone to oxidation than the more graphite like the HBC $C_{42}H_{18}$ or the $C_{96}H_{24}$, Fig. 6.11 and Fig. 6.12. The Graphene Ribbon shows an increased reactivity at lower temperatures (300 °C). This is due to the bent graphene ribbons resulting in an overall more polyolefinic structure. As already described for the soot samples the structure is expected to show a higher reactivity. The graphitic stacked HBC and $C_{96}H_{24}$ are less prone to oxidation due to the more graphitic properties as already evidenced by the TEM and EELS experiments. The H_2O signal emerging from the three samples stems from the C–H termination of the graphenes. As a conclusion on the structure reactivity correlation experiments, the Graphene Ribbon structure is the most suitable for a comparative analysis between soot and synthetic materials. The other platelet–like materials are "too perfect" to serve as real model single graphenes, as their structure does not inhibit different oxygen functional groups.

6.4.3 Linking Gas Phase with Reactivity

The influence of NO_2 and H_2O on diesel engine soot oxidation has been investigated in various studies prior to this work. The oxidation of the carbon black Printex–U, graphite and activated carbons in presence of NO_2, O_2 and NO [146] on soot aerosols [147] as well as on diesel engine soot [148] have been investigated. Phenomenological models for soot oxidation were presented [118, 149–151]. Other groups investigated the influence of O_2 and NO_2 on the generation of surface oxygen groups [127, 131, 152, 153]. The influence of an optimized design of particulate traps on the soot oxidation are tested [126], as well as the influence of engine settings and exhaust gas temperatures [121]. Other groups report the soot – nitrous oxide interactions under atmospheric conditions [154].

It is generally accepted, that NO_2 enhances the oxidation of soot and carbon black. The effect of induced reactivity with higher amount of NO_2 is an effect of enhanced graphene functionalization with oxygen groups. This effect takes place due to the easier dissociation of NO_2 on graphenes in comparison with the O_2. It has been shown in a recent ab initio modeling study of the oxidation of the basal plane of a graphene that the initial step is chemisorption of an oxygen atom across a C–C bond of the graphene sheets. The calculated binding energy of the chemisorbed oxygen atom is 250– 300 kJ mol^{-1}, which must be compared with the bond dissociation enthalpies D(O–O) = 498 and D(ON—O) = 306 kJ mol^{-1}. The reaction is exothermic, but enhanced with NO_2 due to the lower dissociation energy. Transferred to the results of soot and carbon black oxidation, this means that at lower temperatures the first step to the oxidation of the carbons, being the functionalisation, is enhanced. The total oxidation of the carbon to CO_2 occurs at lower temperatures.

When comparing the oxidation in various amounts of NO_2, it is apparent that highly functionalized graphenes are less prone to an enhancement of oxidation with NO_2. The GfG soot does not display such significant differences in the oxidation curves as the Euro IV or the BS soot. From the TG experiments it is apparent that the influence of the oxidation of the soot through NO_2 is dominant at temperatures between 200 °C and 450 °C. The first step of creating an oxygen functional group is easier due to the strong oxidative properties of the NO_2.

This is even more evidenced in the calculated predictions for the isothermal oxidation. Where at low temperatures (200–350 °C) in the case of the BS soot the mass loss over time would not be significant (range of 5% mass loss after 6 h of oxidation) the addition of 500 ppm NO_2 to the oxidizing gas atmosphere enhances the oxidation (20% mass loss). The addition of NO_2 increases the oxidation of the graphitic parts of the soot. Apparently the oxidation of graphitic material with O_2 only does not take place at temperatures below 400 °C, here the oxidation, when O_2 and NO_2 is present, is dominated by the interaction of the NO_2 with the single graphenes.

NO_2 lowers the apparent activation energy at temperatures relevant for diesel soot oxidation. For temperatures between 50–350 °C, activation energies from 50 – 80 kJ/mol are reported. This correlates well with the data found with the model free estimation (Friedman) or the model fitting routines discussed earlier.

Nevertheless, the general soot nanostructure plays an important role in the overall reactivity. Different reaction rates and activation energies are reported in the literature. In many cases this is attributed to different experimental setups. In this work it is obvious, that the differences in activation energies and rates stem from the differences in microstructure of the soot. So even in the case of gasification of soot with NO_2, the structure reactivity correlation discussed in the section 6.4.2 before

holds. It is important to mention that in the case of the GfG soot the overall reaction is enhanced but not as significantly as in the case of the Euro IV soot or even the BS soot. It seems that the more functionalized the graphenes are, the less the soot oxidation could be enhanced. If the soot is more graphitic, the overall functionalization is enhanced, probably NO_2 generates thermodynamically favored surface functional groups that play the key role in carbon oxidation at temperatures less than 400 °C.

H_2O enhances the soot oxidation slightly. This is also reported by other investigations. The H_2O might undergo a water–gas–shift reaction. Another possibility is, that the water enhances the functionalisation of the graphenes with lactones, carboxyl or anhydrides. These groups are then responsible for an overall enhanced total conversion of the soot samples to CO_2. Another explanation for the role of water is that the decomposition of surface oxygen groups as soot oxidation intermediates is enhanced. This is, of course, beneficial in view of commercial application because about 2—10% water is always present in the exhaust stream.

Overall the NO_2 rich atmosphere enhances the soot oxidation at lower temperatures. The enhanced reactivity of soot emitted from modern diesel engines plays an important role in the exhaust after–treatment. With both of these issues the diesel engine exhaust after–treatment is feasible at temperatures typical of the exhaust train.

Chapter 7

Conclusion and Outlook

TEM, EELS (discussed in chapter 4) and the surface sensitive techniques DRIFTS and XPS (discussed in chapter 5) are very powerful in order to understand physical properties of carbons, in this work soot materials. HRTEM investigations give an insight into the defective graphite like structures. Soot consists of spherical particles built up of stacked graphenes, the BSU. Part of the soot exhibits a fullerenoid morphology with strong bent and defective graphenes. The Euro IV diesel engine soot consists of graphitized spherical particles and of a fullerenoid part. The fullerenoid soot exhibits strong bent graphenes. The spark discharge (GfG) soot is a fullerenoid soot, spherical particles are not found. Black Smoke soot, the Furnace Soot and the Lamp Black, in contrary, mainly consist of spherical particles. EELS spectra show the predominant bonding behavior of the carbon. A direct quantification of the sp^2/sp^3 ratio is possible. Superimposed on the direct quantification of the bonding are contributions from bonds to hydrogen and/or oxygen. However, the amount of oxygen bound to the carbon surface is measured with DRIFTS and XPS. The trends in the degree of graphitization are mirrored. The more defective the soot material is (smaller and stronger bent graphenes) the higher the amount of oxygen is. With these study it is demonstrated that soots from various sources are structurally different and need to be thoroughly investigated in order to draw further conclusions about reactivity and potential health risks.

The TG/TPO investigations (chapter 6) show that soots and carbon black materials from different sources exhibit different reactivities. The onset temperature as well as the temperature, where carbons are completely oxidized is different. The defective carbons as the spark discharge GfG Soot and the Euro IV Soot oxidize faster than the well graphitized soot samples (Black Smoke soot and Furnace Soot). This can be correlated with the micromorphology and the functionalization of the soot materials.

The fact that soot from modern Euro IV diesel engines is more easily oxidized, might give new impulses for exhaust treatment technologies. One has to be aware that model soot substances have to be carefully chosen and investigated for any future development. The choice of adequate model carbon systems is crucial for the understanding of the reactivity of the carbonaceous materials. NO_2 enhances the soot oxidation at low temperatures. Nevertheless soot from different sources, with their unique microstructure, will still exhibit differences in the reactivity.

Fig. 7.1 illustrates these results. The graph shows the main results of the structure–reactivity relationship described in this work. On the left side scale the correlation of microstructure (Table 4.1) resulting in oxygen functional groups (Table 5.1) is plotted. The Microstructure is quantified with the HRTEM investigations, the oxygen functional groups are measured and quantified with XPS. On the right side scale the reactivity correlation, giving the amount off mass loss after 6 h of oxidation in 5% O_2 in N_2 measured in TG experiments (Fig. 6.3), is plotted.

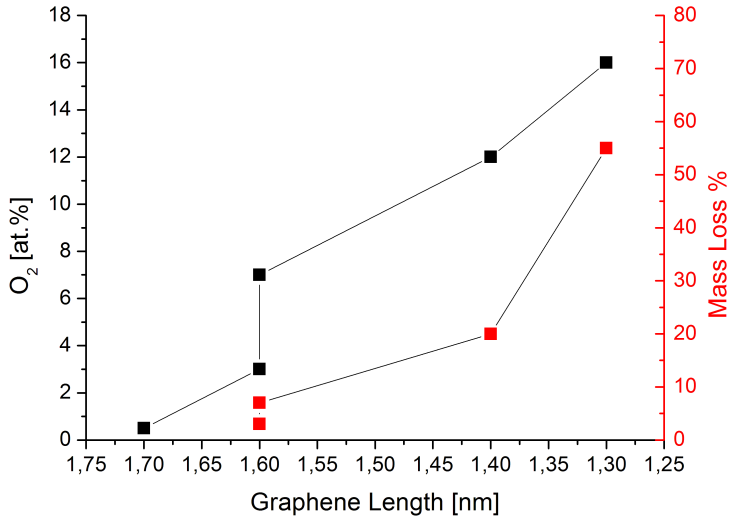

Fig. 7.1: Graph showing the main results of the structure–reactivity relationship described in this work. On the left side the correlation of defects resulting in oxygen functional groups Table 4.1 and 5.1. On the right side the reactivity correlation, giving the amount off mass loss after 6 h of oxidation in 5% O_2 in N_2 measured in TG experiments Fig. 6.3. The smaller the graphenes, the higher the functionalization and the reactivity.

The reactivity of the small fullerene–like soot originating from the heavy duty test diesel engine optimized to fulfill the Euro IV conditions may have consequences for the future development of exhaust treatment systems. Certainly the reduction of particle size is undesirable due to potentially easier access of the fine particles to human lung membranes. However it seems that, from the physico–chemical

point of view the formation of fullerene–like soot in optimized diesel engines is an indicator of the improvement in diesel engine combustion systems. The small particle size, highly defective surface structure, and more easily oxidized fullerene–like soot, identified in this work, are favorable for the catalytic automotive pollution control, if the substance can be converted to CO_2 completely. With an appropriate particulate trap, and choice of oxidative atmosphere, it is feasible to oxidize the investigated Euro IV soot at temperatures relevant for the exhaust gas train. This is shown with the combined effect of the enhanced oxidative properties of the NO_2 and the soot microstructure.

The present work is also relevant for health risk assessments: the reduction of the emitted soot particulate mass is not automatically beneficial for environmental protection and for reducing the epidemiological effect for human health. The risk of the technological achievement of reducing the mass is a shift of structural and chemical properties of the particles of a novel quality with adverse potential, as the soot becomes smaller in size and carries a large amount of OH groups on the local defective sites of the rough surface of the fullerenoid soot. Of relevance is further the similarity in size of surface features of the fullerenoid soot and typical dimensions of enzymatic pockets resulting in the possibility of a geometrically matching interface between inorganic materials and the biosphere. However and fortunately, this new risk potential stands opposite to the fact that, due to the same microstructural/surface–chemical reasons, the fullerenoid soot is more reactive towards oxidation. It is easier to be eliminated.

Bibliography

[1] D. Stadler, M. J. Rossi, The Reactivity of NO_2 and HONO on Flame Soot at Ambient Temperature: The Influence of Combustion Conditions, Phys. Chem. Chem. Phys. 2 (2000) 5420.

[2] A. R. Chughtai, M. M. O. Atteya, J. Kim, B. K. Konowalchuk, D. Smith, Adsorption and Adsorbate Interaction at Soot Particle Surfaces, Carbon 36 (1998) 1573.

[3] V. H. Grassian, Chemical Reactions of Nitrogen Oxides on the Surface of Oxide, Carbonate, Soot, and Mineral Dust Particles: Implications for the Chemical Balance of the Troposphere, J. Phys. Chem. A 106 (2002) 860.

[4] J. E. Hansen, A. A. Lacis, Sun and Dust versus Greenhouse Gases: An Assessment of their Relative Roles in Global Climate Change, Nature 346 (1990) 713.

[5] H.-G. Neumann, Health Risk of Combustion Products: Toxicological Considerations, Chemosphere 42 (2001) 473.

[6] J. Kagawa, Health Effects of Diesel Exhaust Emissions – a Mixture of Air Pollutants of Worldwide Concern, Toxicology 181 - 182 (2002) 349.

[7] M. Riedl, D. Diaz-Sanchez, Biology of Diesel Exhaust Effects on Respiratory Function, J. Allergy Clin. Immunol. 115 (2005) 221.

[8] B. R. Stanmore, J. F. Brilhac, P. Gilot, The Oxidation of Soot: a Review of Experiments, Mechanisms and Models, Carbon 39 (2001) 2247.

[9] J. P. A. Neeft, M. Makee, J. A. Mulijn, Diesel Particulate Emission Control, Fuel 76 (1997) 1129.

[10] A. D. H. Clague, J. B. Donnet, T. K. Wang, J. C. M. Peng, A Comparison of Diesel Engine Soot with Carbon Black, Carbon 37 (1999) 1553.

[11] C. Li, T. C. Brown, Carbon Oxidation Kinetics from Evolved Carbon Oxide Analysis During Temperature-Programmed Oxidation, Carbon 39 (2001) 725.

[12] R. Schlögl, Surface Composition and Structure of Active Carbons, in: F.Schüth, K. Sing, J. Weitkamp (Hrsg.), Handbook of Porous Solids, Wiley-VCH, Weinheim, 2002, Ch. , pp. 1863–1900.

[13] N. W. Ashcroft, N. D. Mermin, Solid State Physics, Holt–Saunders International Editions, Philadelphia, 1976.

[14] H. W. Kroto, J. R. Heath, S. C. O'Brien, R. F. Curl, R. E. Smalley, C_{60}: Buckminsterfullerene, Nature 318 (1985) 162.

[15] S. Iijima, Helical Microtubules of Graphitic Carbon, Nature 354 (1991) 56.

[16] M. S. Dresselhaus, G. Dresselhaus, P. Eklund, Science of Fullerenes and Carbon Nanotubes, Academic Press, San Diego, 1996.

[17] D. B. Kittelson, Engines and Nanoparticles: A Review, J. Aerosol Sci. 29 (1998) 575.

[18] E. Jacob, N. D'Alfonso, A. Döring, S. Reisch, D. Rothe, R. Brück, P. Treiber, PM-KAT: Nichtblockierende Lösung zur Minderung von Dieselruß für EuroIV–Nutzfahrzeugmotoren, H.P. Lenz (Hrsg.) 23. Internationales Wiener Motorensymposium, 25.–26. April 2002 Band 2: Fortschritt-Berichte VDI Reihe 12 Nr. 490 Düsseldorf: VDI–Verlag (2002) 196 – 216.

[19] E. Jacob, D. Rothe, R. Schlögl, D. S. Su, J.-O. Müller, R. Nießner, C. Adelhelm, A. Messerer, U. Pöschl, K. Müllen, C. Simpson, Ž. Tomović, Dieselruß: Mikrostruktur und Oxidationskinetik, H.P. Lenz (Hrsg.) 24. Internationales Wiener Motorensymposium, 15.–16. Mai 2003, Band 2: Fortschritt–Berichte VDI Reihe 12 Nr. 539 Düsseldorf: VDI–Verlag (2003) 19 – 45.

[20] B. A. A. L. van Setten, M. Makkee, J. A. Moulijn, Science and Technology of Catalytic Diesel Particulate Filters, Catal. Rev. 43 (2001) 489.

[21] P. Ciambelli, P. Corbo, M. Gambino, V. Palma, S. Vaccaro, Catalytic Combustion of Carbon Particulate, Catalysis Today 27 (1996) 99.

[22] G. Mul, J. P. A. Neeft, F. Kapteijn, M. Makkee, Soot Oxidation Catalyzed by a Cu/K/Mo/Cl Catalyst: Evolution of the Chemistry and the Performance of the Catalyst, Appl. Cat. B 6 (1995) 339.

[23] G. Mul, F. Kapteijn, J. A. Moulijn, Catalytic Oxidation of Model Soot by Metal Chlorides, Appl. Cat. B 12 (1997) 33.

[24] V. G. Milt, M. L. Pisarello, E. E. Miró, C. A. Querini, Abatement of Diesel–Exhaust Pollutants: NO_x Storage and Soot Combustion on K/La_2O_3 Catalysts, Appl. Cat. B 1276 (2002) 1.

[25] A. Setiabudi, J. Chen, G. Mul, M. Makkee, J. A. Moulijn, CeO_2 Catalysed Soot Oxidation. The Role of Active Oxygen to Accelerate the Oxidation Conversion, Appl. Cat. B 51 (2004) 9.

[26] W. Jahn, Easily Prepared Holey Films for Use in Cryo–Electron Microscopy, J. Microscopy 179 (1995) 333.

[27] L. Reimer, Transmission Electron Microscopy, 4th Edition, Springer, 1997.

[28] J. C. H. Spence, Experimental High–Resolution Electron Microscopy, 2nd Edition, Oxford University Press, 1996.

[29] D. B. Williams, C. B. Carter, Transmission Electron Microscopy: A Textbook in Materials Science, Plenum Press, 1996.

[30] R. F. Egerton, Electron Energy–Loss Spectroscopy in the Electron Microscope, Plenum Press, New York, 1996.

[31] L. Reimer, (Ed.), Energy–Filtering Transmission Electron Microscopy, Springer, 1995.

[32] P. Schattschneider, Fundamentals of Inelastic Electron Scattering, Springer, 1996.

[33] S. D. Berger, D. R. McKenzie, P. J. Martin, EELS Analysis of Vacuum Arc–Deposited Diamond–Like Films, Phil. Mag. Lett. 57 (1988) 285.

[34] B. Jouffrey, P. Schattschneider, C. Hébert, The Magic Angle: a Solved Mystery, Ultramicroscopy 102 (2004) 61.

[35] U. O. Köylü, G. M. Faeth, T. L. Farias, M. G. Carvalho, Fractal and Projected Structure Properties of Soot Aggregates, Comb. Flame 100 (1995) 621.

[36] M. Wentzel, H. Gorzawski, K.-H. Naumann, H. Saathoff, S. Weinbruch, Transmission Electron Microscopical and Aerosol Dynamical Characterization of Soot Aerosols, Aerosol Science 34 (2003) 1347.

[37] A. Oberlin, High Resolution TEM Studies of Carbonization and Graphitization, in: P. Thrower (Edt.), Chemistry and Physics of Carbon 22, Dekker, New York, 1989.

[38] T. Belz, H. Werner, F. Zemlin, U. Klengler, M. Wesemann, B. Tesche, E. Zeitler, R. Schlögl, On the Mechanism of Fullerene Formation, Angew. Chem. Int. Ed. 33 (1994) 1866.

[39] T. Ishiguro, N. Suzuki, Y. Fujitani, H. Morimoto, Microstructural Changes of Diesel Soot During Oxidation, Comb. Flame 85 (1991) 1.

[40] T. Ishiguro, Y. Takatori, K. Akihama, Microstructure of Diesel Soot Particles Probed by Electron Microscopy: First Observation of Inner Core and Outer Shell, Comb. Flame 108 (1997) 231.

[41] M. Müller, J. Petersen, R. Strohmeier, C. Günther, N. Karl, K. Müllen, Ab Initio Study of Surface Structural Changes During Methanol Synthesis over Zn/Cu(111), Angew. Chem., Int. Ed. Engl. 35 (1996) 886.

[42] C. Kübel, K. Eckhard, V. Enkelmann, G. Wegner, K. Müllen, , J. Mater. Chem 10 (2000) 879.

[43] Ž. Tomović, to be published.

[44] C. Helsper, W. Mölter, F. Löffler, C. Wadenpohl, S. Kaufmann, G. Wenninger, Investigations of a New Aerosol Generator for the Production of Carbon Aggregate Particles, Atmosp. Environment 27A (1993) 1271.

[45] D. E. Evans, R. M. Harrison, J. G. Ayres, The Generation and Characterisation of Elemental Carbon Aerosols for Human Challenge Studies, J. Aerosol Sci. 34 (2003) 1023.

[46] T. Belz, J. Find, D. Herein, N. Pfänder, T. Rühle, M. Wohlers, R. Schlögl, On the Production of Different Carbon Forms by Electric Arc Graphite Evaporation, Ber. Bunsenges. Phys. Chem. 101 (1997) 712.

[47] A. Sharma, T. Kyotani, A. Tomita, Direct Observation of Raw–Coals in Lattice Fringe Mode Using High–Resolution Transmission Electron Microscopy, Energy & Fuels 14 (2000) 1219.

[48] H. S. Shim, R. H. Hurt, N. Y. C. Yang, A Methodology for Analysis of 002 Lattice Fringe Images and its Application to Combustion–Derived Carbons, Carbon 38 (2000) 29.

[49] A. Goel, P. Hebgen, J. B. V. Sande, J. B. Howard, Combustion Synthesis of Fullerenes and Fullerenic Nanostructures, Carbon 40 (2002) 177.

[50] F. Tuinstra, J. L. Koenig, Raman Spectrum of Graphite, J. Chem. Phys. 53 (1970) 1126.

[51] R. Escribano, J. J. Sloan, N. Siddique, N. Sze, T. Dudev, Raman Spectroscopy of Carbon–Containing Particles, Vib. Spec. 26 (2001) 179.

[52] R. F. Egerton, M. J. Whelan, Electron Energy Loss Spectra of Diamond, Graphite and Amorphous Carbon, J. Elec. Spec. Rel. Phen. 3 (1974) 232.

[53] H. Daniels, A. Brown, A. Scott, A. Scott, T. Nichells, B. Brand, R. Brydson, Experimental and Theoretical Evidence for the Magic Angle in Transmission Electron Energy Loss Spectroscopy, Ultramircoscopy 96 (2003) 523.

[54] C. Hébert, B. Jouffrey, P. Schattschneider, Comment on "Experimental and Theoretical Evidence for the Magic Angle in Transmission Electron Energy Loss Spectroscopy" by H. Daniels, A. Brown, A. Scott, T. Nichells, B. Rand and R. Brydson, Ultramicroscopy 101 (2004) 271.

[55] N. K. Menon, J. Yuan, Quantitative Analysis of the Effect of Probe Convergence on Electron Energy Loss Spectra of Anisotropic Materials, Ultramicroscopy 74 (1998) 83.

[56] A. C. Ferrari, A. Libassi, B. K. Tanner, V. Stolojan, J. Yuan, L. M. Brown, S. E. Rodil, B. Kleinsorge, J. Robertson, Density, sp^3 Fraction and Cross-Sectional Structure of Amorphous Carbon Films Determined by X–Ray Reflectivity and Electron Energy–Loss Spectroscopy, Phys. Rev. B62 (2000) 11089.

[57] A. J. Papworth, C. J. Kiely, A. P. Burden, S. R. P. Silva, G. A. J. Amaratunga, Electron–Energy–Loss Spectroscopy Characterization of the sp^2 Bonding Fraction within Carbon Films, Phys. Rev. B 62 (2000) 12628.

[58] R. L. vander Wal, A. J. Tomasek, Soot nanostructure: dependence upon synthesis conditions, Comb. Flame 136 (2004) 129.

[59] W. Zhu, D. E. Miser, W. G. Chan, M. R. Hajaligol, HRTEM Investigations of Some Commercially Available Furnace Carbon Blacks, Surf. Sci. 42 (2004) 1841.

[60] H. F. Calcote, Mechanisms of Soot Formation in Flames – A Critical Review, Comb. Flame 42 (1981) 215.

[61] B. S. Haynes, H. G. Wagner, Soot Formation, Prog. Energy Combust. Sci. 7 (1981) 229.

[62] I. M. Kennedy, Models of Soot Formation and Oxidation, Prog. Energy Combust. Sci. 23 (1997) 95.

[63] O. I. Smith, Fundamentals of Soot Formation in Flames with Application to Diesel Engine Particulate Emissions, Prog. Energy Combust. Sci. 7 (1981) 225.

[64] Q. L. Zhang, S. C. O'Brien, J. R. Heath, Y. Liu, R. F. Curl, H. W. Kroto, R. E. Smalley, Reactivity of Large Carbon Clusters: Spheroidal Carbon Shells and Their Possible Relevance to the Formation and Morphology of Soot, J. Phys. Chem. 90 (1986) 525.

[65] F. Tao, V. I. Golovitchev, J. Chomiak, APhenomenological Model for the Prediction of Soot Formation in Diesel Spray Combustion, Comb. Flame 136 (2004) 270.

[66] K.-H. Homann, Fullerenes and Soot Formation – New Pathways to Large Particles in Flames, Angew. Chem. Int. Ed. 37 (1998) 2434.

[67] F. Xu, K.-C. Lin, G. M. Faeth, Soot Formation in Laminar Premixed Methane/Oxygen Flames at Atmospheric Pressure, comb. Flame 115 (1998) 195.

[68] J. Appel, H. Bockhorn, M. Frenklach, Kinetic Modeling of Soot Formation with Detailed Chemistry and Physics: Laminar Premixed Flames of C_2 Hydrocarbons, Comb. Flame 121 (2000) 122.

[69] H. Bockhorn, Ultrafine Particles from Combustion Sources: Approaches to What We Want to Know, Phil. Trans. R. Soc. Lond. A 358 (2000) 2659.

[70] B. M. Vaglieco, S. S. Merola, A. D'Anna, A. D'Alessio, Spectroscopic Analysis and Modeling of Particulate Formation in a Diesel Engine, J. Quant. Spec. Rad. Trans. 73 (2002) 443.

[71] H. Richter, J. B. Howard, Formation of Polycyclic Aromatic Hydrocarbons and Their Growth to Soot – a Review of Chemical Reaction Pathways, Progress in Energy and Combustion Science 26 (2000) 565.

[72] K.-H. Homann, Fulleren – und Rußbildung – Wege zu großen Teilchen in Flammen, Angew. Chem. 110 (1998) 2572.

[73] R. Schlögl, Carbons, in: G. Ertl, H. Knözinger, J. Weitkamp (Hrsg.), Handbook of Heterogeneous Catalysis, Wiley-VCH, Weinheim, 1997, Ch. 2.1.9., pp. 138–191.

[74] C. Jäger, H. Mutschke, T. Henning, Optical Properties of Carbonaceous Dust Analogues, Astron. Astrophys. 332 (1998) 291.

[75] C. Jäger, T. Henning, R. Schlögl, O. Spillecke, Spectral Properties of Carbon Black, J. Non–Cryst. Solids 258 (1999) 161.

[76] U. Bergmann, H. Groenzin, O. C. Mullins, P. Glatzel, J. Fetzer, S. Cramer, Carbon K–edge X–ray Raman Spectroscopy Supports Simple, Yet Powerful Description of Aromatic Hydrocarbons and Asphaltenes, Chem. Phys. Lett. 369 (2003) 184.

[77] J. T. Titantah, K. Jorissen, D. Lamoen, Density Functional Theory Calculations of Energy–Loss Carbon Near–Edge Spectra of Small Diameter Armchair and Zigzag Nanotubes: Core–Hole, Curvature, and Momentum–Transfer Orientation Effects, Phys. Rev. B 69 (2004) 125406.

[78] J. T. Titantah, D. Lamoen, Technique for the sp^2/sp^3 Characterization of Carbon Materials: Ab Initio Calculation of Near–Edge Structure in Electron–Energy–Loss Spectra, Phys. Rev. B 70 (2004) 075115.

[79] S. Tomita, M. Fujii, S. Hayashi, K. Yamamoto, Electron Energy–Loss Spectroscopy of Carbon Onions, Chem Phys. Lett. 305 (1999) 225.

[80] U. Stephan, T. Frauenheim, P. Blaudeck, G. Jungnickel, π Bonding Versus Electronic–Defect Generation: An Examination of Band Gap Properties in Amorphous Carbon, Phys. Rev. B 49 (1994) 1489.

[81] O. Stéphan, P. M. Ajayan, C. Colliex, Curvature–Induced Bonding Changes in Carbon Nanotubes Investigated by Electron Energy–Loss Spectrometry, Phys. Rev. B 53 (1996) 13824.

[82] R. Kuzuo, M. Terauchi, M. Tanaka, Y. Saito, H. Shinohara, High Resolution Electron Energy–Loss Spectra of Solid C_{60}, Jpn. J. Appl. Phys. 30 (1991) L1817.

[83] R. Kuzuo, M. Terauchi, M. Tanaka, Electron Energy–Loss Spectra of Carbon Nanotubes, Jpn. J. Appl. Phys. 31 (1992) L1484.

[84] R. Kuzuo, M. Terauchi, M. Tanaka, Y. Saito, H. Shinohara, Electron Energy–Loss Spectra of Crystalline C_{84}, Phys. Rev. B 49 (1994) 5054.

[85] K. Varlot, J. Martin, C. Quet, Y. Kihn, Towards Sub–Nanometer Scale EELS Analysis of Polymers in the TEM, Ultramicroscopy 68 (1997) 123.

[86] K. Varlot, J. M. Martin, D. Gonbeau, C. Quet, Chemical Bonding Analysis of Electron–Sensitive Polymers by EELS, Polymer 40 (1999) 5691.

[87] K. Varlot, J. M. Martin, C. Quet, Phase Differentiation of a Tri–Phase Polymer Composite Using Energy–Filtering Transmission Electron Microscopy, Polymer 41 (2000) 4599.

[88] A. Braun, F. E. Huggins, N. Shah, Y. Chen, S. Wirick, S. B. Mun, C. Jacobsen, G. P. Huffmann, Advantages of Soft X–ray Absorption over TEM–EELS for Solid Carbon Studies – a Comparative Study on Diesel Soot with EELS and NEXAFS, Carbon 43 (2005) 117.

[89] B. Reznik, D. Gerthsen, K. J. Hüttinger, Micro– and Nanostructure of the Carbon Matrix of Infiltrated Carbon Fiber Felts, Carbon 39 (2001) 215.

[90] M. Hesse, H. Meier, B. Zeeh, Spektroskopische Methoden in der organischen Chemie, Georg Thieme Verlag, Stuttgart New York, 1984.

[91] B. Dippel, H. Jander, J. Heintzenberg, NIR FT Raman Spectroscopic Study of Flame Soot, Phys. Chem. Chem. Phys. 1 (1999) 4707.

[92] S. Turgeon, R. W. Paynter, On the Determination of Carbon sp^2/sp^3 Ratios in Polystyrene–Polyethylene Copolymers by Photoelectron Spectroscopy, Thin Solid Films 394 (2001) 44.

[93] U. Wild, N. Pfänder, R. Schlögl, Species Analysis of Automotive Carbon Particles: Application of XPS for Integral Analysis of Filter Samples, Fresenius J. Anal. Chem. 357 (1997) 420.

[94] P. M. A. Sherwood, Surface Analysis of Carbon and Carbon Fibers for Composites, J. Elec. Spec. Rel. Phen. 81 (1996) 319.

[95] J. A. Leiro, M. H. Heinonen, T. Laiho, I. G. Batirev, Core–Level XPS Spectra of Fullerene, Highly Oriented Pyrolytic Graphite, and Glassy Carbon, J. Elec. Spe. Rel. Phen. 128 (2003) 205.

[96] R. Haerle, E. Riedo, A. Pasquarello, A. Baldereschi, Sp^2/sp^3 Hybridisation Ratio in Amorphous Carbon from C1s Core–Level Shifts: X–Ray Photoelectron Spectroscopy and First–Principles Calculation, Phys. Rev. B65 (2001) 045101.

[97] B. Rousseau, H. Estrade-Szwarckopf, A.-L. Thomann, P. Brault, Stable C–Atom Displacements on HOPG Surface under Plasma Low–Energy Argon–Ion Bombardment, Appl. Phys. A 77 (2003) 591.

[98] U. Zielke, K. J. Hüttinger, W. P. Hoffmann, Surface Oxidized Carbon Fibers II: Chemical Modification, Carbon 34 (1996) 999.

[99] S. Biniak, G. Szymański, J. Siedlwski, A. Światkowski, The Characterization of Activated Carbons with Oxygen and Nitrogen Surface Groups, Carbon 35 (1997) 1799.

[100] H. P. Boehm, Surface Oxides on Carbon and their Analysis: a Critical Assessment, Carbon 40 (2002) 145.

[101] J. L. Figueiredo, M. F. R. Pereira, M. M. A. Freitas, J. J. M. Orfao, Modification of the Surface Chemistry of Activated Carbons, Carbon 37 (1999) 1379.

[102] H. Estrade-Szwarckopf, XPS Photoemission in Carbonaceaous Materials: A "defect" Peak Beside the Graphitic Assymmetric Peak, Carbon 42 (2004) 1713.

[103] K. Umishita, Y. Ochiai, K. Iwasaki, S. Hino, Photoelectron Spectra of Carbon Materials Containing Multiwall Carbon Nanotubes, Synth. Met. 121 (2001) 1159.

[104] S. Doniach, M. Šunjić, Many–Electron Singularity in X–ray Photoemission and X–ray Line Spectra from Metals, J. Phys. C 3 (1970) 285.

[105] F. R. McFreely, S. P. Kowalczyk, L. Ley, R. G. Cavell, R. A. Pollak, D. A. Shirley, X–ray Photoemission Studies of Diamond, Graphite, and Glassy Carbon Valence Bands, Phys. Rev. B9 (1974) 5268.

[106] S. Suzuki, C. Bower, T. Kiyokura, K. G. Nath, Y. Watanabe, O. Zhou, Photoemission Spectroscopy of Single–Walled Carbon Nanotube Bundles, J. Elec. Spec. Rel. Phen. 114 (2001) 225.

[107] J.-O. Müller, D. S. Su, R. E. Jentoft, J. Kröhnert, F. C. Jentoft, R. Schlögl, Morphology Controlled Reactivity of Carbonaceous Materials Towards Oxidation, Catalysis Today 102–103 (2005) 259.

[108] D. M. Smith, A. R. Chughtai, The Surface Structure and Reactivity of Black Carbon, Coll. Surf. A 105 (1995) 47.

[109] H. Jung, D. B. Kittelson, M. R. Zachariah, Kinetics and Visualization of Soot Oxidation Using transmission Electron Microscopy, Comb. Flame 136 (2004) 445.

[110] S. Vyazovkin, C. A. Wight, Kinetics In Solids, Annu. Rev. Phys. Chem. 48 (1997) 125.

[111] K. Pielichowski, Kinetic Analysis of the Thermal Decomposition of Polyaniline, Solid State Ionics 104 (1997) 123.

[112] C. H. Bamford, C. F. H. Tipper, Comprehensive Chemical Kinetics; vol. 2; The Theory of Kinetics, Elsevier Publishing Company, Amsterdam-London-New York, 1969.

[113] H. Schmalzried, Chemical Kinetics of Solids, Wiley-VCH, Weinheim, 1995.

[114] K. H. Laidler, Chemical Kinetics, 3rd Edition, Harper & Row, Cambridge, 1987.

[115] H. L. Friedman, New Methods for Evaluating Kinetic Parameters from Thermal Analysis Data, Journal of Polymer Science Part B: Polymer Letters 7 (1969) 41.

[116] W. Jander, Reaktionen im festen Zustande bei höheren Temperaturen, Z. anorg. u. allg. Chem 163 (1927) 1.

[117] M. Ammann, U. Pöschl, Y. Rudich, Effects of Reversible Adsorption and Langmuir–Hinshelwood Surface Reactions on Gas Uptake by Atmospheric Particles, Phys. Chem. Chem. Phys 5 (2003) 531.

[118] F. Jacquot, V. Logie, J. Brilhac, P. Gilot, Kinetics of the Oxidation of Carbon Black by NO_2. Influence of the Presence of Water and Oxygen, Carbon 40 (2002) 335.

[119] R. T. Yang, C. Wong, Kinetics and Mechanism of Oxidation of Basal Plane on Graphite, J. Chem. Phys. B 75 (1981) 4471.

[120] R. T. Yang, C. Wong, Mechanism of a Single–Layer Graphite Oxidation: Evaluation by Electron Microscopy, Science 214 (1981) 437.

[121] I. P. Kandylas, G. C. Koltsakis, NO_2–Assisted Regeneration of Diesel Particulate Filters: A Modeling Study, Ind. Eng. Chem. Res. 41 (2002) 2115.

[122] J. Nagle, R. F. Strickland-Constable, Oxidation of Carbon Between 1000–2000 °C, in: Proc. Conf. on Carbon, Pergamon Press, New York, Vol. 1, 1962, p. 154.

[123] G. Blyholder, J. S. Binford, H. Eyring, A Kinetic Theory for the Oxidation of Carbonized Filaments, J. Phys. Chem. 62 (1958) 263.

[124] W.-Y. Chen, A. Kulkarni, J. L. Milum, Stochastic Modeling of Carbon Oxidation, Reactors, Kinetics and Catalysis 45 (1999) 2557.

[125] J. A. Moulijn, F. Kapteijn, Towards a unified Theory of Reactions of Carbon with Oxygen–Containing Molecules, Carbon 33 (1995) 115.

[126] A. Setiabudi, M. Makkee, J. A. Moulijn, An Optimal NO_x Assisted Abatement of Diesel Soot in an Advanced Catalytic Filter Design, Appl. Cat. B 42 (2003) 35.

[127] A. Setiabudi, M. Makkee, J. A. Moulijn, The Role of NO_2 and O_2 in the Accelerated Combustion of Soot in Diesel Exhaust Gases, Appl. Cat. B 50 (2004) 185.

[128] Z. Zhu, G. Lu, J. Finnerty, R. T. Yang, Electronic Structure Methods Applied to Gas—Carbon Reactions, Carbon 41 (2003) 635.

[129] K. A. Davis, R. H. Hurt, N. Y. C. Yang, T. J. Headley, Evolution of Char Chemistry, Crystal Unity, and Ultrafine Structure during Pulverized-Coal Combustion, Comb. and Flame 100 (1995) 31.

[130] H. Wang, B. Z. Dlugogorski, E. M. Kennedy, Coal Oxidation at Low Temperatures: Oxygen Consumption, Oxidation Products, Reaction Mechanism and Kinetic Modelling, Prog. Energy Comb. Sci. 29 (2003) 487–513 29 (2003) 487.

[131] J. Zawadzki, M. Wiśniewski, K. Skowrońska, Heterogeneous Reactions of NO_2 and NO–O_2 on the Surface of Carbons, Carbon 41 (2003) 235.

[132] F. Atamny, J. Blöcker, B. Henschke, R. Schlögl, T. Schedel-Niedrig, M. Keil, A. M. Bradshaw, Reaction of Oxygen with Graphite: X-ray Absorption Spectroscopy of Carbonaceous Materials, J. Phys. Chem 96 (1992) 4522.

[133] H. Werner, D. Herein, J. Blöcker, B. Henschke, U. Tegtmeyer, T. Schedel-Niedrig, M. Keil, A. M. Bradshaw, R. Schlögl, Spectroscopic and Chemical Characterisation of "Fullerene Black", Chem. Phys. Lett. 194 (1992) 62.

[134] B. Henschke, H. Schubert, J. Blocker, F. Atamny, R. Schlögl, Mechanistic Aspects of the Reaction Between Carbon and Oxygen, Thermochimica Acta 234 (1994) 53.

[135] K. Zaghib, X. Song, K. Kinoshita, Thermal Analysis of the Oxidation of Natural Graphite: Isothermal Kinetic Studies, Thermochimica Acta 371 (2001) 57.

[136] G. Ghigo, A. Maranzana, G. Tonachini, C. M. Zicovic-Wilson, M. Causa, Modeling Soot and Its Functionalization under Atmospheric or Combustion Conditions by Density Functional Theory within Molecular (Polycyclic–Aromatic–Hydrocarbon–Like) and Periodic Methodologies, J. Phys. Chem B 108 (2004) 3215.

[137] H. Ulbricht, G. Moos, T. Hertel, Physisorption of Molecular Oxygen on Single–Wall Carbon Nanotube Bundles and Graphite, Phys. Rev. B 66 (2002) 075404.

[138] H. Ulbricht, G. Moos, T. Hertel, Interaction of Molecular Oxygen with Single–Wall Carbon Nanotube Bundles and Graphite, Surf. Sci. 532–535 (2003) 852.

[139] I. W. Chiang, B. E. Brinson, A. Y. Huang, P. A. Wills, M. J. Broniowski, J. L. Margrave, R. E. Smalley, R. H. Hauge, Purification and Characterization of Single–Wall Carbon Nanotubes (SWNTs) Obtained from the Gas–Phase Decomposition of CO (HiPco Process), J. Phys. Chem. B 105 (2001) 8297.

[140] Y. Yang, H. Zou, B. Wu, Q. Li, J. Zhang, Z. Liu, X. Guo, Z. Du, Enrichment of Large–Diameter Single–Walled Carbon Nanotubes by Oxidative Acid Treatment, J. Phys. Chem. B 106 (2002) 7160.

[141] R. L. vander Wal, A. J. Tomasek, Soot Oxidation: Dependence Upon Initial Nanostructure, Comb. Flame 132 (2003) 1.

[142] K. Choho, W. Langenaeker, G. vande Woude, P. Geerlings, Reactivity of Fullerenes: Quantum–Chemical Descriptors Versus Curvature, J. Mol. Struct. (Theochem) 338 (1995) 293.

[143] R. Haddon, G. Scuseria, R. Smalley, C_{240} – The Most Chemically Inert Fullerene, Chem. Phys. Lett. 272 (1997) 38.

[144] J. Poater, X. Fradera, M. Duran, M. Solà, An Insight into the Local Aromaticities of Polycyclic Aromatic Hydrocarbons, Chem. Eur. J. 9 (2003) 1113.

[145] T. Belz, R. Schlögl, Characterization of Fullerene Soots and Carbon Arc Electrode Deposits, Synth. Met. 77 (1996) 223.

[146] K. L. Choi, N. W. Cant, D. L. Trimm, Gasification of Carbonaceous Particulates, J. Chem. Technol. Biotechnol. 71 (1998) 57.

[147] S. Kamm, H. Saathoff, K.-H. Naumann, O. Möhler, U. Schurath, Gasification of a Soot Aerosol by O_3 and NO_2: Temperature Dependence of the Reaction Probability, Comb. Flame 138 (2004) 353.

[148] F. Arens, L. Gutzwiller, U. B. H. W. Gäggeler, M. Ammann, Heterogeneous Reaction of NO_2 on Diesel Soot Particles, Environ. Sci. Technol. 35 (2001) 2191.

[149] J. P. A. Neeft, T. X. Nijhuis, E. Smakman, M. Makee, J. A. Mulijn, Kinetics of the Oxidation of Diesel Soot, Fuel Processing Technology 47 (1996) 1.

[150] B. A. Lur'e, A. V. Mikhno, Interaction of NO_2 with Soot, Kinetics Catal. 38 (1997) 490.

[151] A. Messerer, R. Niessner, U. Pöschl, Comprehensive Kinetic Characterization of the Oxidation and Gasification of Model and Real Diesel Soot by Nitrogen Oxides and Oxygen under Engine Exhaust Conditions: Measurement, Langmuir–Hinshelwood, and Arrhenius Parameters, submitted.

[152] H. Muckenhuber, H. Grothe, The Reaction Between Soot and NO_2 – Investigation on Functional Groups Using TPD–MS, Topics in Catalysis 30/31 (2004) 287.

[153] M. Jeguirim, V. Tschamber, J. F. Brilhac, P. Ehrburger, Interaction Mechanism of NO_2 with Carbon Black: Effect of Surface Oxygen Complexes, J. Anal. Appl. Pyrolysis 72 (2004) 171.

[154] C. Alcala-Jornod, H. van den Bergh, M. J. Rossi, Reactivity of NO_2 and H_2O on Soot Generated in the Laboratory: a Diffusion Tube Study at Ambient Temperature, Phys. Chem. Chem. Phys 2 (2002) 5584.

Thanks

I would like to thank all the people who helped me in every kind of way to get this work done. First of all Prof. Dr. R. Schlögl, who gave me the opportunity to do the work at the Fritz–Haber–Institute. I learned a lot and profited from a giant knowledge in carbon chemistry. Dr. D. S. Su, as my supervisor was often enough encouraging me, when I was coming to points where I was only seeing the black part of my work. I owe a lot to Dr. R. E. Jentoft, who gave me a considerable amount of help in order to support my first steps in chemistry, solid state kinetics, any kind off issues on TG and TPO. Dr. T. Ressler discussed with me the issues of solid state chemistry. Dr. F. C. Jentoft and J. Kröhnert helped me with IR spectroscopy; thank you U. Wild for the XPS measurements. M. Swoboda developed and built the soot particle collector which worked impeccably, and surveyed together with me the first test in Nürnberg. I thank M.–G. Willinger and Dr. J. B. Wagner for extremely fruitful discussions and excellent working atmosphere in our office (L 0.07 at the "Ernst–Ruska–Bau"). This is equally true for the whole group Electron Microscopy: G. Weinberg, N. Pfänder, H. Sauer, Dr. D. Wang. I also have to thank W. Fritz for proof reading of the manuscript.

This work was performed in the project "Katalytisches System zur filterlosen kontinuierlichen Rußpartikelverminderung für Fahrzeugdieselmotoren" supported by the Bayerische Forschungsstiftung and performed in the framework of ELCASS. In this context I would like to thank A. Messerer, D. Rothe and Ž. Tomović, the involved PhD students for a good cooperation. Merci bien C. Salzemann, C. Chan Thaw et Dr. J. P. Tessonier pour me donner la possibilité de reanimer mon français, cela m'a fait beaucoup plaisir. Last not least I have to thank the youngsters from the "Seglervereinigung Havel e.V." who did a great job in distracting me from work in case I did (and didn't) need it.

... to the family, they know why.